UNIVERSITY OF JOHANNESBURG

A Functional Dependence Analysis of Wind Erosion Modelling System Parameters to Determine a Practical Approach for Wind Erosion Assessments

Hanlie Liebenberg-Enslin

A thesis submitted in fulfilment of the requirements for the Degree of

Doctor of Philosophy

Department of Geography, Environmental Management & Energy

Faculty of Science

UNIVERSITY OF JOHANNESBURG

Supervisor: Professor Harold John Annegarn

May 2014

Affidavit:

To Whom It May Concern

This serves to confirm that I, Hanlie Liebenberg-Enslin, ID number: 710109 0102 087; student number: 908921075, enrolled for the degree *Philosophiae Doctor* (Environmental Management), Faculty of Science, University of Johannesburg herewith declare that my academic work is in line with the Plagiarism Policy of the University of Johannesburg with which I am familiar.

I further declare that the work presented in the thesis

"*A Functional Dependence Analysis of Wind Erosion Modelling System Parameters to Determine a Practical Approach for Wind Erosion Assessments*"

is authentic and original unless clearly indicated otherwise and in such instances full reference to the source is acknowledged and I do not pretend to receive any credit for such acknowledged quotations, and that there is no copyright infringement in my work. I declare that no unethical research practices were used or material gained through dishonesty. I understand that plagiarism is a serious offence and that should I contravene the Plagiarism Policy notwithstanding signing this affidavit, I may be found guilty of a serious criminal offence (perjury) that would amongst other consequences compel the UJ to inform all other tertiary institutions of the offence and to issue a corresponding certificate of reprehensible academic conduct to whomever request such a certificate from the institution.

Signed at _____ on this _____ day of _____ 2014

Signature_____
Hanlie Liebenberg-Enslin

STAMP COMMISSIONER OF OATHS
    Affidavit certified by a Commissioner of Oaths

This affidavit conforms with the requirements of the JUSTICES OF THE PEACE AND COMMISSIONERS OF OATHS ACT 16 OF 1963 and the applicable Regulations published in the GG GNR 1258 of 21 July 1972; GN 903 of 10 July 1998; GN 109 of 2 February 2001 as amended.

Dedication

I dedicate this work to my parents,
my late father, Petrus Wessel Liebenberg, and
my mother, Wilma Liebenberg.

Acknowledgements

I am deeply grateful to Prof. Harold Annegarn, for his advice and supervision throughout this study and for the opportunities afforded me. Without his assistance, this study would not have been possible.

I would like to express my sincere gratitude to my colleague Dr Lucian Burger, for his technical support and guidance. His in-depth technical knowledge and insight served me greatly throughout the course of this study.

Prof. Yaping Shao is thanked for patiently replying to all my questions relating to his research.

I wish to extend my appreciation to Mr Charl Human from AngloGold Ashanti for making their ambient and source data available for use in this study. I also want to thank Dr Jon Andrews and Ms Annah Kgaswane from Impala Platinum for allowing the use of their data. Dr Kristy Langerman is thanked for providing me with the Eskom data used in this study.

I would like to thank my company, Airshed Planning Professionals (Pty) Ltd, for the financial support through payment of my registration fees, and making available in-house software for use in this thesis. My colleagues at Airshed are thanked for their patience and support throughout the duration of my research. The technical support and advice received from Dr Gerrit Kornelius is highly appreciated.

Thanks are also due to Elisabeth Anne Frewin for proof reading the language in this final version of this thesis.

My deepest gratitude goes to my parents for their loving support and for the sound moral values and principles, they have instilled in me. Their love has been the encyclopaedic foundation throughout my life and even though my father is not with us anymore, I know he would have been proud.

My special thanks go to my husband, Johann Enslin, for his moral support, patience and understanding throughout the years. Without his enduring love and inspiration, this study would not have been completed.

To my family and friends, I wish to extend my appreciation for their incessant backing and support.

Abstract

The focus of Aeolian research has mainly been on wind-blown dust from desert and arid areas. Numerous dust emission schemes have been developed over the years aimed at accurately estimating dust emission rates from various soil types and land use surfaces. Limited research has been done on wind-blown dust from smaller area sources – such as mine tailings and ash storage facilities. Lately, the concern about the environmental and health impacts, caused by dust from mine tailings storage facilities and ash disposal sites, has become more prominent, calling for better methods in determining dust emissions and their related impacts.

This thesis established a practical approach for wind-blown dust emissions estimation and dispersion modelling from mine waste and ash storage facilities for the purpose of legal compliance assessment. Extensive research on the physics of wind erosion has been done over the past decade, compelling the re-evaluation of previously applied techniques. The latest and most widely applied dust emission schemes are evaluated to determine, through systematic testing of parameterisation and validation, using empirical mine waste and coal ash data, a best-practice prescription for quantifying wind-blown dust emissions and determining effects on a local scale using commercially available dispersion models.

The applicability of two dust-flux schemes, (one developed by Marticorena and Bergametti (1995) and the simplified Shao 2004 scheme, as reported in 2011) for the quantification of wind-blown dust emissions, were tested using site specific particle size distribution data, bulk density and moisture content from six gold- and one platinum- tailings storage facilities and from two ash storage facilities. The availability of the required input parameters and the uncertainty associated with these parameters, were tested. The dependency of the Shao *et al.* (2011) model on plastic pressure (P) and the coefficient c_y, both of which are not easily determined, added to the uncertainty of the emission rates. In this study, P and c_y were both interpolated using the range limits provided by Shao (2004) for natural soils. By calculating P, using the salt and calcium carbonate content, similar values were obtained. The minimally disturbed dust fraction, as required by the Shao *et al.* (2011) scheme were derived from particle size distribution analysis but found to be more representative of the fully disturbed particle size faction (η_{fi}) and therefore needed to be corrected to represent the minimally disturbed particle size faction (η_{mi}) through the application of a correction factor, $CF\eta_{mi}$.

Specific attention was given to the quantification of the threshold friction velocity (u^*_t) and the threshold velocities (u^*), and how these two parameters relate to each under variable wind speed and time durations. This was tested using sub-hourly averaged meteorological data, one set reflected 5-minute intervals and the other 10-minute intervals. Dependent on the frequency and

strength of the sub-hourly wind gusts, the resulting dust-flux rates were found to vary significantly when based on hourly averaged wind data in comparison with 5- and 10-minute wind data.

Dispersion models are useful tools in air quality management. Whereas ambient monitoring provides actual ambient concentrations for specific pollutants at set locations, atmospheric dispersion models can be used to simulate any number of pollutants and determine the impacts at any location within the modelling domain. These dust-flux schemes of Marticorena and Bergametti (1995) and Shao *et al.* (2011) have been coupled with the US EPA regulatory Gaussian plume AERMOD dispersion model for the simulation of ground level concentrations resulting from wind-blown dust from mine tailings facilities. For this study, two Case Studies were evaluated; one included two of the gold mine tailings and the second focused on the platinum tailings. Simulated ambient near surface concentrations were validated with ambient monitored data for the same period as used in the model.

For the Marticorena and Bergametti (1995) dust-flux scheme, only z_0 had to be adjusted to provide a good fit with measured data – whereas the Shao *et al.* (2011) scheme resulted in significantly higher concentrations, resulting in an over-prediction of the measured data. By applying the correction factor, $CF\eta_{\text{mi,}}$ to the minimally disturbed dust fraction, the predicted concentrations improved considerably.

The coupling of the dust-flux schemes with a regulatory Gaussian plume model provided simulated ground level PM_{10} concentrations in good agreement with measured data. The best correlation was found under conditions of high wind speeds when the prevailing wind was from the direction of the tailings storage facility.

This thesis demonstrates that simulated impacts from complex source groups can be performed, within an acceptable range of certainty, using widely applied dust-flux schemes. These dust-flux schemes, developed primarily for large-scale desert and arid areas, have been demonstrated to be applicable also to small-scale sources, of the order of 1 km^2, and can be coupled to regularly available dispersion models for impact evaluations of wind-blown dust. The value of this improved approach to the mining and mineral processing industries are substantial, allowing for more accurate health risks and adverse environmental assessments from wind-blown dust from large material storage piles, a source category that has hitherto been difficult to quantify.

Table of Contents

List of Figures

List of Tables

List of Abbreviations and Acronyms

AD	Anno Domini
ADDAS	Airborne Dust Dispersion model from Area Sources
AERMOD	American Meteorological Society/Environmental Protection Agency Regulatory Model
Asl	above sea level
ASF	Ash Storage Facility
CERC	Cambridge Environmental Research Consultants
CFD	Computational Fluid Dynamic
DEA	Department of Environmental Affairs, South Africa
DMR	Department of Mineral Resources, South Africa
EIA	Environmental Impact Assessment
GLC	Ground level concentration
IRIS	Integrated Risk Information Systems
ITCZ	Inter-tropical Convergence Zone
JPEG	Joint Photographic Experts Group
kPa	Kilo Pascal
MB95	Marticorena and Bergametti (1995) dust-flux scheme
meq	millequivalents
MFE	Ministry for the Environment, New Zealand
MME	Ministry of Mines and Energy, Namibia
Pa	Pascal
PM_{10}	Particulate Matter with an aerodynamic diameter of less than 10 μm
$PM_{2.5}$	Particulate Matter with an aerodynamic diameter of less than 2.5 μm
RWEQ	Revised Wind Erosion Equation
SAWS	South African Weather Service
SH11	Shao *et al.* (2011) dust-flux scheme
TSF	Tailings Storage Facility
TSP	Total Suspended Particulates
US EPA	United States Environmental Protection Agency
WBG	World Bank Group
WEPS	Wind Erosion Prediction System
WEQ	Wind Erosion Equation
WHO	World Health Organization

<div align="right">

CHAPTER ONE

</div>

1   Introduction

1.1   Background

Dust emissions from anthropogenic, natural and biogenic sources give rise to ambient pollution concentrations and fallout (Friedrich, 2009). Wind-blown dust from natural mineral sources is estimated to account for between 75% (Ginoux *et al.,* 2012) and 89% (Satheesh & Moorthy, 2005) of the global aerosol load, of which 25% (Ginoux *et al.,* 2012) to 50% (Tegen & Fung, 1995) is attributed to disturbed soil surfaces and the rest to natural soil surfaces. Estimates indicate around 1 000 million tons of global dust emissions are generated annually (Zender *et al*., 2003; Ginoux *et al*., 2004; Miller *et al.*, 2004; Tanaka & Chiba, 2006), with recent estimates as high as 2 000 million tons per annum (Shao *et al*., 2011b). In Africa, approximately 54% of the dust is from desert and sparsely vegetated soils (Tegen & Fung, 1995), where North Africa alone contributes 55% of the global dust emissions of which only 8% is from anthropogenic sources (Ginoux *et al.,* 2012). Wind erosion can lead to land degradation where fertile agricultural topsoil is lost during events of strong winds (Queensland Government, 2013). Mahowald *et al*. (2010) estimated that the global dust loads have doubled in the 20th century due to anthropogenic activities. According to Eswaran and Reich (2001), yield reduction due to soil erosion in Africa alone amounts to between 2% and 40%. Mining operations and aggregate extraction sites are significant sources of anthropogenic dust emissions (McKenna Neuman *et al*., 2009) with wind-blown dust primarily emanating from mine storage facilities.

Airborne particulate matter comprises a mixture of organic and inorganic substances, varying in size, shape and density. These can be divided into Total Suspended Particulates (TSP), thoracic particles or PM_{10} (particulate matter with an aerodynamic diameter of less than 10 µm) and respirable particles or $PM_{2.5}$ (particulate matter with an aerodynamic diameter of less than 2.5 µm). PM_{10} and $PM_{2.5}$ are associated with health impacts; TSP is associated with nuisance caused by dust fallout. The particle size and density determine the residence time in the atmosphere, with coarser and denser particles deposited faster because of gravitation – the finer particles remain suspended for longer. The optical properties of dust also influence the impact on visibility – the inorganic substances can include various metals, salts and radionuclides (Colls, 2002).

Aerosols in the atmosphere (both directly and indirectly) influence the atmospheric radiation balance, the scattering and absorbing of radiation components (and indirectly) by changing the optical properties and lifetime of clouds (Shao, 2008; Alfaro & Gomes, 2001; Myhre & Stordal, 1997). Over southern Africa, stable layers in the troposphere have significant effects on the

recirculation (Tyson *et al.*, 1996) resulting in a haze layer below the 20°S latitude comprising primarily of Aeolian dust (Piketh *et al.*, 1999).

High concentrations of particulates in the air pose a risk to human health and welfare. According to the World Health Organisation (WHO), no safe thresholds have been determined for particulate exposures resulting in a linear dose-response relationship for thoracic (PM_{10}) and respirable ($PM_{2.5}$) dust. Quantitative health risk assessments have provided alternatives to determine residual risks linked to a particular guideline value and these informed the WHO 2005 air quality guidelines and interim targets for PM_{10} and $PM_{2.5}$, relating mortality risks to air quality targets (WHO, 2005).

Wind erosion has a significant influence on air quality and human health (Goudie, 2009). Various studies have found a link between increased morbidity and mortality, especially amongst children and the elderly, and dust storm events (Ginoux *et al.*, 2012; Karanasiou *et al.*, 2012; De Longueville *et al.*, 2013). During a dust storm in Beijing for example, ambient dust concentrations were measured in the range 5 to 20 mg m^{-3} (Shao, 2008; Yabuki *et al.*, 2002). During the dust storm on the 23 September 2009 in eastern Australia, measured hourly PM_{10} and $PM_{2.5}$ concentrations reached 6 460 and 814 μg m^{-3}, respectively in the Central Business District of Brisbane. The PM_{10} fraction made up 68% of the total mass with $PM_{2.5}$ accounting for 10% (Jayaratne *et al.*, 2011). Modelled global fine particulate matter concentrations – specifically desert dust with an aerodynamic diameter 2.5 μm – were found to cause premature mortality, resulting in a global per capita motility rate of 0.014% per year and an estimated 1.7% of the total cardiopulmonary and lung cancer deaths (Giannadaki *et al.*, 2014).

Wind erosion is strongly variable in space and intermittent in time (Alfaro & Gomes, 2001; Lu & Shao, 2001). A number of parameters control the source strength and spatial distribution of dust concentrations and fallout. Particle entrainment, transport and deposition are the three processes for dust mobilisation by wind (Zender *et al.*, 2003). As shown in Figure 1, these are influenced by: atmospheric conditions (e.g. wind, precipitation and temperature); soil properties (e.g. soil texture, composition and aggregation); land-surface characteristics (e.g. topography, moisture, aerodynamic roughness length, vegetation and non-erodible elements); and land-use practice (e.g. farming, grazing and mining). The quantification and simulation of windblown dust is thus not a trivial task (Shao, 2008). Wind erodible materials vary spatially in composition (i.e. size distribution, moisture content, vegetation cover). The way these materials are dispersed in the atmosphere depends on the particle characteristics (i.e. particle size, shape, density) and the atmospheric conditions (wind speed, precipitation, surface elements). According to Alfaro and Gomes (2001) the only approach to parameterise the wind erosion process is through successive modelling of: (i) the dust production process; (ii) the transportation of particles once airborne; and (iii) the aerosol optical properties that determine the way it is transported in the atmosphere. The

area with the largest uncertainty remains the dust production process since there is no model that can account for all the variables influencing dust entrainment (Shao, 2008; Alfaro & Gomes, 2001; Lu & Shao, 2001).

Debate about the complexity of wind erosion physics and the quantification of wind-blown dust has been on-going for more than 70 years. A number of wind erosion modelling systems have been developed throughout the years, with the first major breakthrough research published by Bagnold in 1941 called *The Physics of Blown Sand and Desert Dunes*. The arrival of computers and electronic databases allowed for the quantifying and modelling of air pollutant emissions on a much larger and more extensive scale (Pulles & Heslinga, n.d.). The Bibliography of Aeolian Research, as updated by Stout in September 2013, contains 42 450 references to Aeolian research papers and reports (Stout, 2013). Over the years, research remained focused on dust-flux modelling and estimating the vertical dust profile. Wind tunnel and field experiments confirm an exponential decay function of dust concentrations with height because of its dependency on particle size distribution and wind speed (Bullard, 2006; Marticorena & Bergametti, 1995; Marticorena *et al*., 1997; Lu, 1999; Shao, 2008).

Two physical forces are responsible for wind erosion where aerodynamic forces (or wind shear stress) attempt to remove particles from the surface, and other forces, (such as gravity and inter-particle cohesion) resist removal (Pye, 1987; Shao, 2008; Marticorena & Bergametti, 1995). For wind erosion to occur, the wind speed needs to exceed a certain threshold, called the friction velocity (u^*). This threshold is linked to both gravity and the inter-particle cohesion that resists removal.

Surface properties (such as soil texture, soil moisture and vegetation cover) influence the removal potential. Conversely, the friction velocity or wind shear at the surface is related to atmospheric flow conditions and surface aerodynamic properties. For particles to become airborne, the wind shear at the surface must exceed the gravitational and cohesive forces acting upon them; the minimum wind velocity at which this occurs is called the threshold friction velocity (u^*_t) (Shao, 2008). According to Bullard (2006) one of the major challenges in Aeolian research remains the attempt to quantify accurately wind eroded dust emission rates, emphasising the importance of understanding the critical thresholds for particulate entrainment. The threshold friction velocity, in turn, is directly affected by moisture, non-erodible roughness elements, and the inter-particle cohesion of the bed material (Bullard, 2006; MacKinnon *et al.*, 2004; McKenna Neuman, 2004).
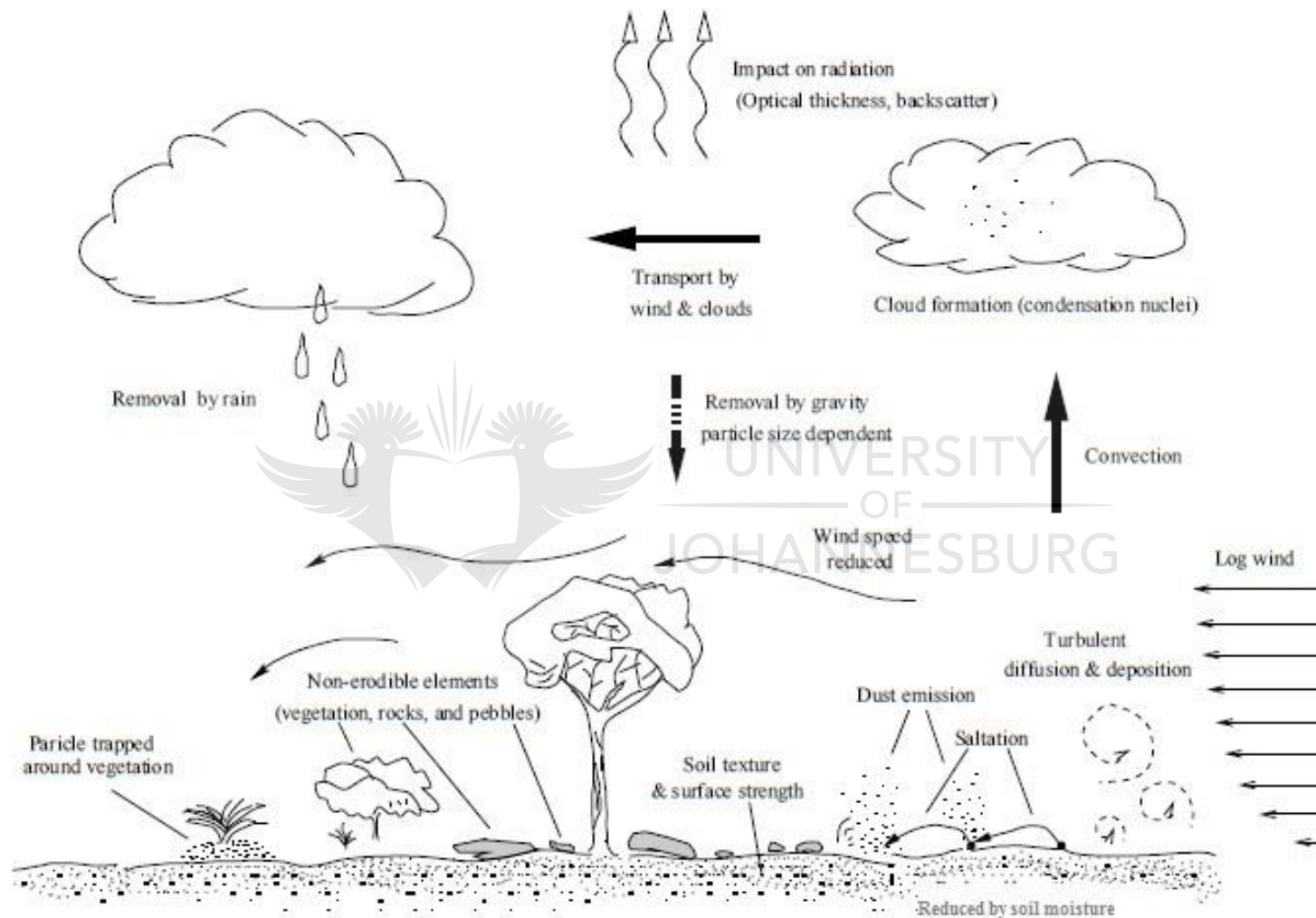
Figure 1: Diagrammatic illustration of the physical processes of dust emission and transport (after Lu, 1999).

In Southern Africa, wind-blown dust from natural arid soil surfaces, disturbed soil surfaces and mining-related-wind-erodible sources all contribute to the local and global dust load. Many regions within Southern Africa are arid with sparsely vegetated surfaces (i.e. southern and central Namibia, north-western South Africa Kalahari and central Botswana). Mining, a significant contributor to fugitive dust generation, is an important economic aspect both in these countries and in the rest of Africa (South Africa Info, 2012). Calculated annual dust emissions from South Africa indicate contributions from areas where the land-use is less than 30% to be 11 MT yr^{-1} with 13 MT yr^{-1} deriving from anthropogenic sources (land-use $> 30\%$). The total annual dust emissions quantified from topographical sources amount to 51 MT yr^{-1} (Ginoux *et al.*, 2012).

South Africa has been a mining intensive country since the discovery of gold in the mid-1800's and mining remains a significant contributor to the national Gross Development Product (Prinsloo, 2007). Gold mining is still an important mining sector, with most of the gold mines concentrated around the Witwatersrand (Gauteng) and northern Free State regions. Historical gold mining has left a legacy of dormant gold tailings storage facilities, in and around the Witwatersrand, with many residential areas having been developed around and close to the base of these tailings facilities (Ojelede *et al.*, 2012; Phakedi, 2011; Annegarn, 2006; Annegarn *et al.*, 2000; 2010).

The Vaal Triangle Airshed Priority Area Air Quality Management Plan identified wind-blown dust from dormant gold mine tailings storage facilities to be one of the main contributing sources of elevated thoracic dust concentrations in the Soweto area (Liebenberg-Enslin *et al.*, 2009). Aside from gold mining, South African mines produce 78% of the world platinum supply, 36% of the palladium and 84% of the worldwide rhodium (Prinsloo, 2007). Waste streams from these mines include waste rock (comprising larger boulders and rocks) and tailings material (constituting the finely milled material). Without appropriate control of the tailings facilities, the material is prone to wind erosion under conditions of high wind speed (Blight, 1989; Blight, 1991; Blight & Amponsah Da Costa, 2001; Blight, 2008). This erosion poses a significant risk to communities located near these tailings storage facilities (Ojelede *et al.*, 2012; Phakedi, 2011; Annegarn, 2006; Annegarn *et al.*, 2000; 2010).

South Africa relies heavily on coal for electricity production. Coal mines are spread all over the Mpumalanga Province (in the north-eastern region of the country). This is also home to most of the country's coal-fired power stations. Ash, a waste product from the combustion process at coal-fired power stations, is typically stored in ash storage facilities and comprises both bottom ash and fly ash. Similar to tailings storage facilities, these ash facilities can be significant sources of wind-blown dust if not controlled (Liebenberg-Enslin *et al.*, 2009). Apart from the visual and

nuisance impacts caused by wind-blown material, the ash contains toxic trace elements in a bio-accessible form, posing a potential risk to human health and well-being (Griffin *et al.*, 1977).

1.2   Motivation for Study

Wind-blown dust from desert and arid areas has been the focus of Aeolian research for many years (Goudie, 2009). Several dust emission schemes have been developed over the years, aiming to estimate accurately the dust emission rate from various soil types and surfaces (Marticorena & Bergametti, 1995; Shao *et al.*, 1996; Lu & Shao, 1999; Shao, 2004). Wind-blown dust from smaller area sources such as mine waste facilities has not been much researched (Kon *et al.*, 2007). In recent years, the concern for environmental and health impacts from mine waste facilities has been given more prominence, calling for better techniques in determining dust emissions and its impacts (McKenna Neuman *et al.*, 2009).

The United States Environmental Protection Agency (US EPA) developed emission factors for the quantification of wind erosion from industrial storage piles. These emission factors apply only to dry, exposed surfaces of mixed size aggregate with limited erosion potential. These emission factors have been based on the highest wind speed event occurring between material disturbances. A uniform particle distribution is assumed and variations in moisture content, particle density, roughness elements or large surface areas have not been considered (US EPA, 2006). The more complex dust models – as developed by Marticorena and Bergametti (1995), Alfaro and Gomes (2001), Lu and Shao (2001), Shao (1996; 2004; 2011) and Zender *et al.* (2003) – have considered these additional parameters. Even though these models use the same parameters to calculate horizontal and vertical fluxes, applying these parameters to the different bed material can result in different emission rates. The models also differ in sensitivity to the various input parameters (such as clay content, moisture content and roughness length). It is therefore necessary to determine the most appropriate modelling scheme for a specific source type.

Burger *et al.* (1997) developed a wind erosion model for the South African electricity supplier, Eskom, to assist with the quantification of wind-blown dust from ash storage facilities associated with the coal-fired power stations. The Airborne Dust Dispersion Model from Area Sources (ADDAS) has been based on the dust emission model proposed by Marticorena and Bergametti (1995) and aims to provide a user-friendly model for the computation of ambient concentrations and depositions levels. The model attempts to account for the variability in source erodability through the parameterisation of the erosion threshold (based on the particle size distribution of the source) and the roughness length of the source surface (Burger *et al.*, 1997; Burger, 2010). In the quantification of wind erosion emissions, the model incorporates the calculation of two important parameters, viz. the threshold friction velocity of each particle size, and the vertically integrated horizontal dust-flux, in the quantification of the vertical dust-flux (i.e.

the emission rate). The model has been updated to allow for the reduction in wind erosion caused by surface soil crusting (Burger, 2010). This update has been based on the research conducted by Gillette *et al.* (1982) and Goossens (2004). Gillette related friction velocity to specific soil crust thickness and modulus of rupture; Goossens investigated the physical crust strength relationship with the horizontal and vertical sediment fluxes. This model has, however, not yet been validated to determine the sensitivity of the input parameters and accuracy of calculated wind-blown dust emissions.

Air quality regulatory compliance studies use off-the-shelf dispersion models and typically account for a range of dust generating activities. Empirical models specific to wind erosion – such as the Wind Erosion Equation (WEQ), the Revised Wind Erosion Equation (RWEQ) and Wind Erosion Prediction System (WEPS) – are not generally applied. In South Africa, the US EPA regulatory Gaussian plume and puff models are most readily used for compliance assessments. Other Gaussian plume models – such as the Atmospheric Dispersion Modelling System (ADMS), developed by the Cambridge Environmental Research Consultants (CERC) – are also used. The disadvantage of using Gaussian Plume models is that the spatial varying of wind fields, because of topography or other factors, cannot be included. In addition, the range of uncertainty of the model predictions is given to be -50% to +200%. The accuracy improves with fairly strong wind speeds, during neutral atmospheric conditions and with longer averaging periods (Hanna *et al.*, 1999). The accurate prediction of instantaneous peaks are the most difficult and analysis of these peaks is normally performed with more intricate dispersion models – specifically fine-tuned and validated for specific locations. The duration of these short-term, peak concentrations is often only a few minutes and on-site meteorological data are then essential (MFE, 2004).

Air quality compliance assessments rely on approved published methodologies – such as the US EPA emission factors – for quantification of fugitive dust emission rates and regulatory dispersion models. The uncertainty around applying the US EPA wind erosion emission factor equations to large waste storage facilities and exposed areas is not known. Furthermore, the physical processes determining wind erosion and the source strengths are still not well understood – especially around the quantification of the threshold friction velocity (Bullard, 2006; Marticorena & Bergametti, 1995; Marticorena *et al.*, 1997; Lu, 1999; Shao, 2004). According to Shao (2008) dispersion simulations of dust particles cannot be done with sufficient accuracy unless the atmospheric patterns and turbulence properties are adequately pre-defined. More accurate predictions could probably be made with Computational Fluid Dynamic (CFD) models but, again, these models are complex and time intensive. A review of the application of atmospheric models for particle dispersion by Holmes and Morawska (2006) assessed a range of Box, Gaussian, and Lagrangian/ Eulerian, CFD models, and models (including aerosol dynamics). The models could not be ranked in order of best-to-worst performance since the order is dependent on the modelling

timescale required, domain environment and nature of the emission sources. The authors highlighted the lack of studies for which modelled results had been validated alongside the study's observations (Holmes & Morawska, 2006). Toraño *et al.* (2007) used CFD modelling to determine the influence of storage pile shapes on wind erosion and determine the best engineering design for storage piles. Follow up work by Diego *et al.* (2009) improved the algorithms in the CFD modelling system to simulate wind flow around storage piles and complex yards whilst quantifying the total fugitive dust from these sources. The application of CFD models remain to be complex and resource intensive and not yet suitable for use in air quality impact assessmens.

The accuracy in quantifying wind erosion dispersion from mine waste facilities and ash storage facilities is therefore reliant on two components, namely:

- the accurate quantification of wind erosion from specific source types;

- the accurate simulation of ground level dust concentrations as a result of wind erosion.

The relevance of determining a standardised emissions estimation and dispersion modelling approach for wind-blown dust (for the purpose of compliance assessment and informing authority decisions) has been confirmed. There will always be a degree of uncertainty around the quantification of wind-blown dust emissions and dispersion simulations of ambient concentrations – but the range of uncertainty should be known and described.

1.3 Hypothesis, Aim and Objectives

1.3.1 Hypothesis

It is possible, with appropriate parameterisation and modern dispersion models, to simulate wind-blown emissions from mine tailings and ash storage facilities with sufficient accuracy to aid in the environmental impact assessment and management of mine residue tailings.

1.3.2 Aims and objectives

The two main aims are:

- To evaluate the available algorithms for simulating wind erosion, by systematic testing of parameterisation and validation using empirical data from two mining sectors, and from coal fired power plant waste streams;

- To derive practical best-practice prescriptions for the use of dispersion models in management of mining atmospheric emissions.

The major objectives are:

(i) to test the functional dependence of selected dust emission schemes on influencing variables using a generic dataset;

(ii) to determine the most appropriate scheme for different source types: gold tailings material, platinum tailings material and coal ash;

(iii) to simulate windblown dust from mine tailings storage facilities on a local scale using a regulatory Gaussian plume model and verify the results with observed data.

1.4 Methodology

This study sets out to determine an improved, practical approach to wind erosion emissions schemes for use in local-scale dispersion modelling using standard regulatory dispersion models. Essential site-specific input parameters are identified through testing the functional dependence of wind erosion modelling systems to the input variables.

Three source types are included, namely: gold mine tailings, platinum mine tailings; and ash storage facilities. Gold tailings from the AngloGold Ashanti Vaal River North operations – located in the North West Province of South Africa (26°56'21.15"S, 26°43'39.29"E) – were used, and for platinum tailings, the Impala Platinum Mine in the central part of the North West Province of South Africa (25°31'15.37"S, 27°11'54.61"E) was selected as the research site. Because of the particle size range of ash and the size of such storage facilities, the same approach was tested on the Tutuka Ash Storage Facility – located in the central part of Mpumalanga, South Africa (26°46'31.58"S, 29°23'29.93"E) and the Majuba Ash Storage facility, located approximately 55 km further south-east (27°06'57.12"S, 29°44'28.08"E).

Material samples were collected from six gold- and one platinum- tailings storage facilities and from two ash storage facilities. These were analysed for: particle size distribution; moisture content; clay content; silt content; particle density; and bulk density. The wind erosion models were tested with the various source materials using the same generic wind speed data. Wind erosion emission rates were quantified with site-specific wind field data and simulated using a regulatory dispersion model. The US EPA regulatory Gaussian plume AERMOD dispersion model was used for all applications. Simulated ambient near surface concentrations were validated with ambient monitored data for the same period used in the model.

The outcome was a standard methodology for wind erosion emission quantification and dispersion simulations.

Figure 2 provides a schematic of the overall research design.

	A functional dependence analysis of wind erosion modelling system parameters to determine a practical approach for wind erosion assessments		
Objectives	Functional dependence analysis of influencing variables	Wind blown dust emissions from various source types	Dispersion simulation of wind blown dust on a small scale
Data & Analytical solutions	– Test existing horizontal saltation flux sensitivity – Test existing vertical dust flux sensitivity – Use generic source data (i.e. particle size range, moisture content, clay content & particle density) – Use generic wind field	– Particle size analysis & source specific material characteristics – Generic meteorological dataset – Google images – Apply selected dust emission schemes to gold and platinum tailings & ash material	– Site specific ambient & meteorological data – Source parameters (size, height) – Coupling of dust emission schemes with AERMOD – Measures & modelled data – Impact evaluation
Analysis & Results	– Functional dependence if influencing variables – Sensitivity analysis – Discussion	– Sensitivity analysis – Comparison of the two selected dust flux schemes – Discussion	– Model results verification – Impact assessment – Discussion
	Discussion of main findings and conclusion		

Figure 2:   Schematic of the overall research design.

1.5   Framework

A brief overview of the existing dust emission schemes is provided in Chapter 2, with the emphasis on the background and modelling of dust emissions. Research on modelling approaches is evaluated, with reviews of existing wind erosion studies for specifically tailings storage facilities and studies conducted in South Africa.

A functional dependence analysis, of the input parameters of a number of the horizontal saltation flux and vertical dust-flux modelling schemes is the focus, of Chapter 3. This chapter opens with a review of the physics and methods on dust emissions modelling. The analysis and assessment uses a generic material dataset and set wind speeds for all the dust modelling schemes. The chapter concludes with the findings of the most sensitive parameters influencing wind erosion estimation.

Chapter 4 details the assessment of the dust emission models on the actual datasets for the gold and platinum tailings facilities, and the ash storage facilities. Background studies on similar sources and approaches are discussed, with the assessment using source specific data. The same generic wind speeds as used in Chapter 3 are applied. The main findings from the assessment are reported at the end of the chapter.

Chapter 5 examines the validity of applying a regulatory Gaussian plume model for the simulation of ambient concentrations from wind-blown particles. The estimation of wind-blown dust – from two of the gold and one of the platinum tailings storage facilities – are done using the methods identified in Chapter 4, with site-specific wind field data for a set timeframe. Predicted ambient ground level concentrations are validated with available ambient monitored data for the same timeframe. The chapter concludes with the findings from this assessment.

The study concludes with Chapter 6 providing a summary of the main findings, recommendations for an improved, practical dust emissions parameterisation for use in calculating emission factors for mine tailings, and conclusions reached.

2   Literature Review

Saltation and suspension are the two modes of airborne particles in the atmosphere. The former mode relates to larger sand particles that hop across the soil surface and are deposited when the wind speed reduces or changes. Suspension refers to the finer dust particles that, once airborne, remain suspended in the atmosphere for longer and can be dispersed and transported over large distances (Shao, 2008). A third mode of surface material movement is surface creep, accounting for particles too big to be lifted, which are pushed along the surface by wind shear forces (Zender, 2005). Wind erosion and transportation primarily depend on particle size and wind speed (Kok *et al*., 2012). Wind erosion models distinguish soil texture into the typical soil class index for particle size fractions of sand (63 µm – 2 mm), silt (2 – 63 µm) and clay (<2 µm) (Gillette *et al*., 1980; Hillel, 1980; Zender *et al*., 2003; Shao, 2008).

Silt fraction or loading in surface dust is the main determining factor in most of the US EPA emission factor equations for dust suspension estimation. The US EPA in their *Procedures for sampling surface/bulk dust loading* specifies the analysis of specifically silt content and moisture content (US EPA, 1993). Dust is generally defined as comprising of silt and clay particles (Shao, 2008).

Parameterisation of wind-blown dust covers the two dimensions of the vertical flux (through the sandblasting process and the entrainment of dust into the upward vertical mass flux) (Gillette, 1977).

2.1   Horizontal Dust Flux

Bagnold (1941) concluded that the threshold friction velocity is dependent on the drag and gravity forces acting on particles and that these differ between particle sizes. Particle movement will only commence once the aerodynamic drag, wielded by the wind on the particle, is greater than the particle's gravitational force directed opposite to the wind direction. Once particles are in motion, the threshold friction velocity decreases – because a proportion of the momentum needed to initiate new particle movement is now supplied by the particles already in motion (Zender, 2005). Iversen and White (1982) determined, through wind tunnel experiments, that the forces acting on a resting particle include: drag; gravity (weight); lift; inter-particle cohesion; and rotational inertia (Figure 3) (Lu, 1999; Zender, 2005). The airflow over the particle influences the lift, drag and moment forces – whereas the weight is determined by the particle size and density (Pye, 1987; Zender, 2005). Several kinds of cohesive forces are at play such as van der Waals forces and the adsorption capacity of the soil through its clay content and electrostatic forces (Kok *et al*., 2012). Iversen and

White (1982) developed a formula to account for the effect of inter-particle cohesion forces and this formula was used in the dust emission model developed by Marticorena and Bergametti (1995).

Owen (1964) developed a theory describing the saltation of uniform particles, indicating that the saltation layer behaves as an aerodynamic roughness where the height is proportional to the thickness of the layer as far as the outer layer of flow is concerned. This is called the saltation roughness length and according to Raupach (1991), this roughness can be considered equivalent to the effect of a vegetation canopy on airflow. Owen's second hypothesis assumed the total momentum transfer in the saltation layer to be constant, with particle momentum flux (τ_p) decreasing and air momentum flux (τ_a) increasing monotonically with height (Shao, 2008). Owen (1964) suggested that the horizontal flux of saltating particles (Q) varies with the cube of the wind friction velocity during saltation (u^*_s).
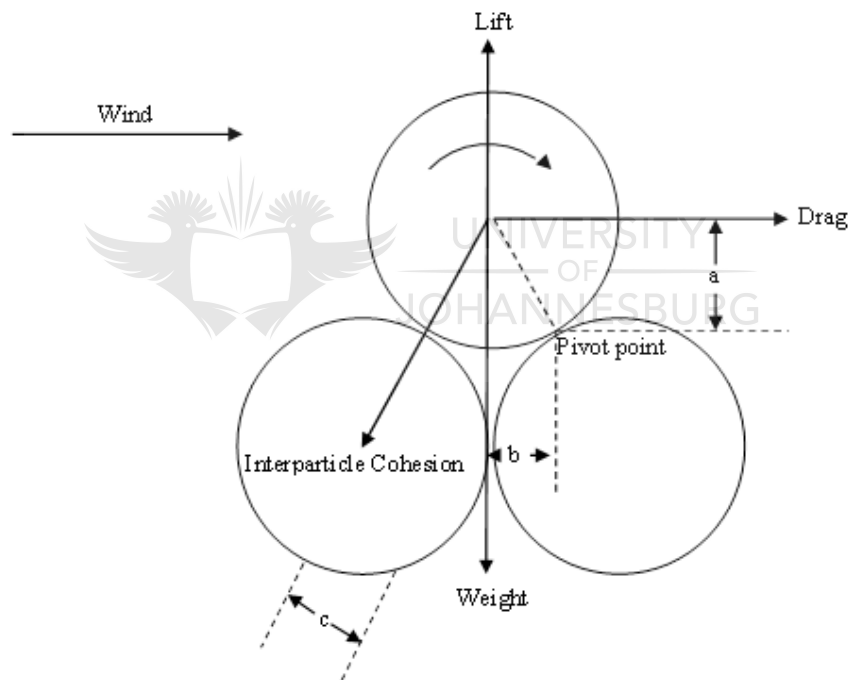
Figure 3: **Forces acting on an erodible spherical particle. a, b and c are moment arms (Greeley & Iversen, 1985).**

Kawamura's (1964) theory for stream-wise saltation flux was further developed by White (1979) who noted that the total stream-wise saltation flux is a product of downward mass flux of saltating particles per unit area per unit time (F_s) and total stream-wise distance (L). Shao *et al.* (1996) developed a theory for stream-wise saltation flux that differs slightly from the Kawamura/White formulation by accounting for the inter-particle binding energy that must be overcome to free the dust particle from the soil surface (Zender, 2005). The dust emission model developed by Marticorena and Bergametti (1995) attempts to account for the variability in source

erodability through the parameterisation of the erosion threshold (based on the particle size distribution of the source) and the roughness length of the surface. In the quantification of wind erosion emissions, the model considers the dust-flux (i.e. the emission rate) to be proportional to the saltation flux with the ratio dependent on the clay content.

Based on the work of Owen (1964), who suggested that the vertical dust-flux is proportional to μ^*_4, Gillette and Passim (1988) developed a model taking into account the effect of soil roughness and field length. Shao *et al.* (1996) in response suggested that new parameters are needed to fully account for soil resistance to dust emission. In 2004 Shao provided a simplified emission scheme to allow for the influence of saltation bombardment and aggregate disintegration where the emission from unconsolidated soils is proportional to μ^*_4 (Shao, 2004). Even though the modelled relationship compared well with previously generated datasets, this model did not account for soil textures influencing the breakage potential of aggregates and ability to eject finer particles into suspension (Bullard, 2006). Raupach and Lu (2004) followed this approach but added several generalised treatments of mobilisation and dry deposition. The approach considers the uniform particles of mass at a steady state of saltation (Zender, 2005). According to Zender (2005), none of these theories can accurately account for the relationship between the mean initial vertical velocity of saltating particles and friction velocity (μ^*).

2.2   Vertical Dust Flux

Vertical dust-flux is primarily caused by aerodynamic lift, saltation bombardment and aggregate disintegration (Burger, 2010). Most dust emission models are based on the relationship between the horizontal flux of saltating particles (Q) and the vertical mass flux (F) (Zender, 2005). Experiments conducted by Iversen and White (1982) determined that saltation-sandblasting produces dynamic dust size distributions which change with wind friction velocity. The kinetic energy of the saltating particle (saltator) determines the dust aerosol size released by sandblasting. The dust size distribution, in turn, is dependent on the parent soil aggregate size distribution and the wind friction velocity (Burger, 2010). High kinetic energy saltators release small dust aerosols; low kinetic energy saltators release large dust aerosols (Shao *et al.*, 1996).

The energy causing dust generation is typically short-lived. Winds associated with gusty conditions (i.e. violent winds with upward diffusion) or levels of high turbulence are needed to project dust – vertically to great heights above the ground – and sustained energy is required to transport the dust over long distances.

According to Marticorena and Bergametti (1995), the suspension-saltation boundary is controlled by the ratio of the threshold friction velocity and the thermal velocity of the particles. Greeley and Iversen (1985) suggested a suspension-saltation boundary, of approximately 50 μm,

where particles below this limit required very high threshold friction velocities to break the strong inter-particle cohesion forces.

The model developed by Gillette and Passi (1988) has been based on the work of Owen (1964) and accounts for the effects of soil roughness and field length. Conversely, Shao (1996) suggested that the saltation impact causes the inter-particle bonds between dust grains to break. Thus, the number of saltation impacts per unit area and unit time will determine the number of dust particles ejected by impact based on the mass of dust particles (Lu, 1999). Marticorena and Bergametti (1995) assumed that the ability of a soil to produce dust is related to its clay content (Gillette, 1978; Prospero, 1981; Glaccum & Prospero, 1980). This approach is, however, not relevant to soils with clay content higher than 20% – i.e. soils, which tends to form crusts that can cause the surface to be highly resistant to wind erosion (Gillette, 1978). This raises another important parameter influencing the ability to move and lift soil particles – namely biological and physical soil crusts. Gillette *et al.* (1982) related friction velocity to specific soil crust thickness and modulus of rupture; whereas Goossens (2004) investigated the physical crust strength relationship to the horizontal and vertical sediment fluxes. This physical strength relationship has been demonstrated by Goossens (2004), who modified the wind erosion models of Marticorena and Bergametti (1995), and Alfaro and Gomes (2001) who were also allowing for soil crusting. Physical and biological crusting can either protect surfaces from weathering or exacerbate these processes – depending on the surface's location, structure and substrate (Bullard, 2006).

Alfaro *et al.* (1997) determined, through wind tunnel experiments, that the size distribution of aerosols, released by sandblasting from any given soil, is dependent on wind conditions. This resulted in the theory that the binding energy of an aerosol particle within the soil is a decreasing function of its size. This allows for the conversion from the horizontal mass flux to the vertical dust mass flux through the sandblasting mass efficiency (Alfaro *et al.*, 1997). Alfaro and Gomes (2001) combined the 1997 sandblasting model and the saltation model of Marticorena and Bergametti (1995) to allow the computation of the amounts and the size distributions of aerosols released by a given soil in given wind conditions. It was found that the ratio, of the vertical mass flux of particles smaller than 20 µm to the soil aggregate horizontal flux, is largely dependent on the wind friction velocity and not directly conditioned by the soil clay content.

Recent research has focused on the vertical profiles of wind velocity and mass flux (Bullard, 2006). Field studies (Han *et al*., 2004) and wind tunnel studies (Liu & Dong, 2004) have shown an exponential decay function of blown sand concentration with height, varying with grain size and wind speed (Bullard, 2006). Dong *et al.* (2004) found that the maximum horizontal sand flux over a sandy surface is at the surface; conversely over a gravel surface the maximum horizontal sand flux is at heights above the surface. The velocity of particle movements in an airstream is, therefore, not only influenced by wind speed but also by bed and inter-particle collisions (Bullard, 2006). Lately

the focus has been on improving the understanding of critical thresholds for particle entrainment. Stout (1998) formulated the relationship between saltation activity and relative wind strength to calculate wind thresholds at five-minute intervals. Other parameters also influencing the critical threshold value include: moisture (Wiggs *et al.*, 2002); non-erodible roughness elements (MacKinnon *et al.*, 2004); and inter-particle cohesion (McKenna Neuman, 2004).

The work by McKenna Neuman and Nickling (1989) identified a relationship between the cohesion reinforcement because of moisture and the erosion threshold of sand. They suggested that the wet threshold friction velocity for sand could be determined by the moisture tension. The electrostatic forces wielded on the water molecules depend on the soil properties where water absorption is low for sand but increase continuously with soil clay content (Hillel, 1980). A combination of the capillary forces ($w_{capillary}$) of the interstitial moisture and the adsorbed moisture (w') cause the threshold friction velocity to increase. Fécan *et al.* (1999) found that increased soil moisture also has an impact on the roughness length and thereby established a coefficient to express the influence of moisture on the threshold for different soil textures.

2.2.1 *Input parameters*

Input parameters to the various horizontal and vertical flux models are listed in Table 1, with the parameter symbol and associated units provided. Where constants have not been provided, the parameter is typically measured or quantified. The symbols may vary between references, with Q often used as the symbol for the vertical dust-flux. The symbols provided in Table 1 are for uniform referencing throughout this study.

Table 1: **Input parameters for theoretical emission models.**

Parameter Symbol	Parameter Description	Parameter unit	Constant used
F	Vertical dust-flux	g m^{-2}	
Q	Horizontal / saltation dust-flux	g m^{-2}	
u^*	Friction / drag velocity	cm s^{-1}	
u^*_t	Threshold friction velocity	cm s^{-1}	
u	Wind speed / velocity	cm s^{-1}	At height z
p_p	Grain / particle density	g cm^{-3}	2.65 g cm^{-3} as typical of quartz
p_b	Bulk soil density	g cm^{-3}	
p_a	Air density	g cm^{-3}	0.00122 g cm^{-3} as typical of atmosphere
g	Acceleration because of gravity	cm s^{-2}	980 cm s^{-2}
d	Mean grain/ particle diameter	cm	
z_0	Surface roughness length	cm	
z_{0s}	Smooth roughness length	cm	$z_0^s \approx {d_p}/{30}$

Parameter Symbol	Parameter Description	Parameter unit	Constant used
λ	Roughness density / propagation distance / frontal area index	-	Drag partition
Re	Particle friction Reynolds number		Re = u
K	Von Karman's constant		0.4
A	Empirical coefficient		*A* = 0.2 for $0.03 \leq R_e \leq 0.3$ *A* = 0.129 for $0.3 \leq R_e \leq 10$ *A* = 0.12 for $R_e \geq 10$
R	Rupture strength	Bar	
θ	Total soil moisture	%	Combination of $w_{capillary}$ *and* $w_{adsorbed}$ (*w'*)
w'	Adsorbed moisture	%	
C_0	Proportionality constant		1.5; 1.8; 2.8 (Bagnold, 1941) 0.83 (Zing, 1958) 1.8 – 3.1 (Kawamura, 1964) 2.6 (White, 1979) $0.25 + \frac{wt}{3u^3}$ (Owen, 1964) 4.2 (Lettau & Lettau, 1978)
τ	Crust strength	Pa or bar	
c	Particle cohesion	-	
σ	Standard deviation	-	
P	Soil plastic pressure	N m^{-2} or bar	
	Horizontal pressure	N m^{-2} or bar	
M	Modulus of rupture	N m^{-2} or bar	
η_c	Percentage clay	%	
f_i	Total volumetric fraction of dust in sediment	-	

2.3 Wind Erosion from Tailings and Ash Storage Facilities

Wind-blown dust from mine waste facilities can be a significant source of dust emissions. High concentrations of wind-blown dust can occur near mining sites, affecting both the environment and human health (Annegarn, n.d.; Formenti *et al*., 1998; McKenna Neuman *et al*., 2009; Ojelede *et al*., 2012). Health risk assessments evaluate the probability that exposure to a certain air pollutant will result in a given adverse effect in an individual or defined population. For risk associated with the inhalation pathway, ambient air quality standards and guidelines, such as those published by the World Health Organisation (WHO, 2005), are aimed to provide safe daily exposure levels for the majority of the population throughout an individual's lifetime. When these ambient air quality guidelines or standards are exceeded, the potential for health risk exist. The US EPA defines Health Risk as *Hazard x Exposure*, where the hazard associated with substances or pollutants has been

established to great extent by animal experiments and human studies and the potential for health effects is linked to the magnitude or level of a specific substance or pollutant and the duration of exposure.

2.3.1 Mineral composition of mine tailings and ash

Aside from the dust concentrations associated with potential health concerns, tailings material comprises of a number of elements. Maseki (2013) conducted a risk assessment of inhaled and ingested airborne particles in the vicinity of gold mines in the Witwatersrand Basin, and found large variation between the elemental concentrations within the tailings storage facility profiles. The elemental concentrations also varied largely between the four gold mine tailings facilities assessed. Elements with the largest variability included potassium (K), chromium (Cr) manganese (Mn), nickel (Ni), cadmium (Cd), gold (Au) and lead (Pb). Iron (Fe), zinc (Zn), arsenic (As) and uranium (U) indicated small variations between the tailings facilities. The variability within the tailings storage facility profiles were attributed to the difference in geological strata (Maseki, 2013) but could also be a result of wind and water erosion, weathering and decomposition, and chemical reaction (Robertson & Skermer, 1988). Radionuclides are also associated with dust particles from gold tailings storage facilities.

The elemental composition of platinum tailings material from a storage facility in South Africa contained sodium (Na), magnesium (Mg), aluminium (Al), phosphorus (P), potassium (K), calcium (Ca), titanium (Ti), vanadium (V), chromium (Cr), manganese (Mn), iron (Fe), cobalt (Co), nickel (Ni), copper (Cu), zinc (Zn), strontium (Sr), zirconium (Zr) and barium (Ba). The elemental concentrations also showed variation within the tailings storage facility profile and chromium was the only element exceeding the relative enrichment factor of ten – where enrichment was defined as a factor greater than 10 relative to the global crustal average (SGS, 2011).

Similarly, elemental concentrations in fly ash from three power plants in the Philippines showed large variation between the samples. The main elements found in the fly ash were arsenic (As), cadmium (Cd), calcium (Ca), chromium (Cr), cobalt (Co), copper (Cu), lead (Pb), manganese (Mn), mercury (Hg), nickel (Ni) and zinc (Zn). The variation was mainly attributed to the different types of coal burnt by each power station (Brigden & Santillo, 2002). Similar metals with the addition of magnesium (Mg), aluminium (Al), iron (Fe), sodium (Na), phosphorus (P) and potassium (K) were found in the ash storage facility at Tutuka Power Station in South Africa (Von Gruenewaldt, 2012).

2.3.2 Health risk from mine tailings and ash storage facilities

The US EPA Integrated Risk Information Systems (IRIS) has established a database providing information on health effects from various elements that may result from exposure to

environmental contaminants. These are reported in the form of chronic and sub-chronic inhalation reference concentrations and cancer unit risk factors. According to the IRIS database metals classified as carcinogenic in humans through the inhalation pathway include for example arsenic (As), hexavalent chromium (Cr(VI)), cadmium (Cd) and nickel (Ni) (IRIS, 2014).

The health risk assessment conducted by Maseki (2013) reported an annual average PM_{10} concentration of 135 µg m^{-3} calculated from a two-week long dust storm at one of the gold tailings storage facilities. The hazard indices for non-cancer risks associated with the elemental concentrations in the tailings material showed acceptable levels of below one for the population residing near the tailings storage facility. Cancer risks associated with arsenic (As), cadmium (Cd) and hexavalent chromium (Cr(VI)) for inhalation and ingestion indicated acceptable levels of 1 in 10 000 to 1 in 1 million (Maseki, 2013).

The air quality assessment conducted for the Tutuka Power Station Ash Storage Facility reported potential acute health effects from the wind-blown ash material. Metals of concern were arsenic (As), mercury (Hg), phosphorus (P) and cadmium (Cd). Cancer risks were reported to be low with the highest level of 5 in 100 000 for chromium (Von Gruenewaldt, 2012).

2.3.3   *Physical processes of wind-blown dust from mine tailings and ash storage facilities*

A major limitation in air quality impact assessments from mine waste facilities is that methods to quantify emissions and determine the impacts have not been widely investigated – most wind erosion models were developed for agricultural lands or sand dunes (Kon *et al*., 2007).

Research conducted by Blight (1989; 1991; 2003; 2008) and Blight & Amponsah da Costa (1999; 2001) showed, through observations and measurements, that the main parameter of wind erosion from gold tailings facilities, aside from slope length and angle, is either surface shear strength or surface hydrological roughness. Findings from earlier research indicate that most erosion occurs from the side slopes of the tailings impoundments with very little emanating from the near-horizontal top surfaces. Field measurements indicate total erosion from these unprotected side slopes may be as high as 500 tons per hectare per annum – this reduces to approximately 100 tons per hectare per annum when the slopes are fully grassed (Blight, 1989; Blight, 1991). Follow-up wind tunnel experiments determined an amplification factor for the differences in wind speed (at a given height above the surface) to the speed (at a standard height) with the maximum amplification factor occurring just upwind of the windward crest, indicating this area is the most susceptible to wind erosion (Blight, 2008). This amplification factor has been based on a logarithmic increase in wind speed over flat terrain with height above ground level. De Kok *et al.* (1993) related increased heights of the ash storage facility to increased wind speeds using the same logarithmic relationship. An increase in the storage facility height therefore results in higher wind velocities, thereby increasing the probability for dust entrainment. These unique physiognomies of

mine waste and coal ash facilities need to be accounted for in the wind-blown dust approach. Similar research on the behaviour of sand dunes indicated wind velocities to be at a maximum over the crest of dunes with shear stress reaching its peak on the steepest part of the windward slope. Depending on the steepness of the slope, the shear stress required to mobilise the sand will be higher at a steep slope in relation to a flatter slope near the crest. It was found that maximum erosion occurs when the shear stress is at its peak on the steepest part of the windward slope, with the maximum deposition potential upwind of the point of flow separation (Pye & Tsoar, 2009). The shear stress profile of turbulent winds over barchans and transverse dunes have been accounted for by the Navier-Stokes equations (Kok *et al*., 2012).

Wind erosion from various material types is directly dependent upon the surface winds (Schmechtig *et al*., 2011). Average wind speeds of between 0.2 and 0.6 m s^{-1} are required to initiate particle movement with higher velocities of between 3.9 and 12.7 m s^{-1} required for poorly sorted wind erodible material (Pye, 1987). According to the US EPA (2006), a threshold wind speed in excess of 5 m s^{-1} is required to initiate erosion from a coal storage pile with wind speeds higher than 6 m s^{-1} required for desert surfaces (Clements *et al*., 1963; Pye, 1987). Mian & Yanful (2003) calcuated that a wind velocity of more than 9 m s^{-1} is required to initiate wind erosion from two tailings storage facilities in in New Brunswick and Ontario, Canada. Blight & Amponsah da Costa (2001) conducted wind tunnel tests to model tailings dam profiles and reported that hourly average wind speeds in exceedance of 12.5 m s^{-1} are needed for uranium material *pick-up* – the velocity that will transport material at a nominal small rate of 20 kg m^{-2} hr^{-1}. Gold tailings material had an even higher *pick-up* threshold of 16.7 m s^{-1}.

Field measurements from near surface gold tailings storage facilities indicate threshold wind velocities of between 2 and 3 m s^{-1}. These are significantly lower than the typical wind speed threshold given by the US EPA (2006) for storage piles of 5.4 m s^{-1}, implying that gold tailings material is more susceptible to wind erosion. One explanation may be that the fine particles in the gold tailings material are less cohesive because of the mechanically generated colloidal shapes. Also the clay content in tailings, and similarly in coal ash, only resembles the size fraction but does not have the same electro-static functions as clay in natural soils. As with natural soils, the amount of dust generation remains a function of both the kinetic energy and the dust fraction available within the material. The clay content still affects the adsorption and absorption of moisture in the material, therefore clay still influences the threshold friction velocity (u^{*}_{t}).

Similar to mine tailings, ash storage facilities are comprised of uniform fine (sub-micron) material, providing an incessant source of erodible material (Burger *et al*., 1997). Research on dust suppression and modelling, initiated in the 1990's by Eskom – South Africa's power supplier, resulted in extensive field measurements coupled with wind erosion quantification and modelling methodologies for coal ash storage facilities (Snow & Held, 1998). Dust monitoring was conducted

at a number of the Eskom power station ash storage facilities to evaluate the amount of wind-blown material because of variable meteorological and surface conditions. A wind erosion model – called ADDAS (Airborne Dust Dispersion from Area Sources) – was developed for the computation of ambient concentrations and depositions levels. Three wind erosion schemes; Bagnold (1941); Cowherd *et al.* (1988) and Marticorena and Bergametti (1995), were incorporated into the ADDAS (Burger *et al.*, 1997).

2.4   Influence of meteorological conditions on wind-blown dust

Meteorological conditions influence the spatial distribution and temporal variations of wind erosion. For wind erosion to occur, strong near-surface winds are required to lift the particles from the surface and strong turbulence or convection is needed to disperse and transport the particles over large distances (Shao, 2008; Schmechtig *et al.*, 2011).

2.4.1   *Macro-scale circulation over South Africa*

Atmospheric processes govern the spatial, diurnal and seasonal variation in the wind field and stability changes (Goldreich & Tyson, 1988). Macro- and meso-scale processes need to be considered to accurately parameterise the atmospheric dispersion potential of a particular area since site-specific meteorological conditions can become very different in diverse geographical settings.

The macro-scale circulation over southern Africa is influenced by systems that originate in the tropics in the north, and temperate latitudes to the south. The lower tropospheric circulation over southern Africa is predominantly anticyclonic (Garstang*, et al.*, 1987, Tyson *et al.*, 1996). Topical easterly waves provide for dry winds from the northeast and north during the South African summer months, but the steep lapse rates give rise to afternoon thunderstorms. The air moving over the Indian Ocean has higher moisture content, resulting in more frequent thunderstorms – especially over the eastern and central parts of the country. Severe storms occur when moist air penetrates the capping inversion over the north-eastern interior, linking this to larger-scale synoptic circulations and the meso- and local-effects (Garstang*, et al.*, 1987). The rainy season, at its peak during January and February, is determined by the location of the Inter-tropical Convergence Zone (ITCZ) – the convergence of the north-eastern monsoons, the south-easterly trade winds and the very moist Congo north-westerly airflow. The drier air limits the rainfall to thunderstorms and showers, which gradually become more infrequent (Torrance, 1972). Westerly disturbances, peaking in spring and autumn (Tyson *et al.*, 1996), result in rainfall due to unstable air at the rear of the surface through and stable clear conditions at the front of it (Preston-Whyte & Tyson, 1988). Associated with these westerly troughs are cut-off lows, responsible for most of the flood-producing rains in South Africa. Propagating westerly waves during winter months result in cold fronts with characteristic cloud cover and wind changes causing gustiness (Preston-Whyte & Tyson, 1988).

A distinct consequence of the anticyclonic wind fields over South Africa is the high occurrence of stable atmospheric layers, especially during winter, resulting in little cloud cover and rainfall, and high solar radiation (Tyson *et al*., 1996; Piketh *et al*., 1999). These stable layers confine the transport of aerosols and trace gasses to remain between these layers by preventing vertical dispersion. Over the interior plateau of South Africa, three layers were observed during the Southern African Fire-Atmosphere Research Initiative (SAFARI) – one typically at 700 hPa, a second at 600 to 450 hPa and the third at 200 hPa, with the second layer occurring for 78% of the time. These stable layers in the troposphere have a significant effect on the recirculation over South Africa (Tyson *et al.*, 1996) resulting in a haze layer south of 20°S of which Aeolian dust in the main constituent reaching 70% percentage contribution during winter (Piketh *et al*., 1999).

The main synoptic conditions conducive to development of strong winds are thunderstorms and extra-tropical cyclones – the passing of cold fronts. Thunderstorms are the main cause of in-land wind gusts during summer when maximum winds occur during the passages of "gust fronts" preceding the rainfall (Kruger *et al*., 2010). These are typically of short duration and not constant in space and time (Kruger *et al*., 2013). Wind gusts associated with the passing of cold fronts mainly affect the coastal parts of the country, but in the northern interior wind gusts occur east of the actual fronts moving in from the west and are also a result of the coastal low pressure systems on the eastern and south-eastern coasts. Four other wind producing mechanisms were identified – ridging of the Atlantic or Indian Ocean high-pressure systems; convergence towards isolated low-pressure systems; or deep coastal low-pressure systems (Kruger *et al*., 2010).

These synoptic conditions influence the boundary layer meteorology, which in turn, has a direct effect on the local meteorological conditions.

2.4.2   *Influence of meso-scale wind speed*

Changes in terrain can significantly influence the wind speed and direction – hills or rough terrain influence the wind speed, wind direction and turbulence characteristics. Significant valleys can cause persistent drainage flows and restrict horizontal movement whereas sloping terrain may help provide katabatic or anabatic flows (Preston-Whyte & Tyson, 1988).

Winds within valleys are complex and influenced by the orientation of the valley walls towards the sun. As the sun rises in the east, the western slope warms up during the morning resulting in the air above the slope to heat and rise. In the afternoon, the same happens with the eastern slope whilst the western slope cools down. As the temperature gradient develops between the mount of the valley and the head of the valley, the up-slope winds start to weaken with valley winds initiated by early afternoon. These again weaken in the late afternoon as the slopes cool down. Typical of day-time airflow under cloudless skies, up-valley winds will prevail whereas the situation is reversed during the night (Preston-Whyte & Tyson, 1988). A study done by

Wiggs *et al*. (2002) on valley flow in the Gaub drainage basin in Namibia (characterized by low relative relief with the slope gently grading down toward the north), has given some insights into the implications for sediment transport in valleys. The study made use of measurement arrays for which the fractional speed-up ratio was calculated. The results compared well with wind tunnel studies (Beniston *et al*., 1989; Kalthoff *et al*., 2000) and suggested that, in areas of relative low relief, valley topography can have a marked impact on wind velocity and direction.

Land-sea breeze circulations also a significant influence on local meteorological conditions. The wind flow pattern is influenced by the presence of the cold ocean, especially during weak wind periods when dilution is at a minimum. The large heat capacity of oceans reduces water-surface temperature change to near-zero values during a diurnal cycle. The land surface warms and cools more dramatically because of the small molecular conductivity and heat capacity in soil prevents the diurnal temperature signal from propagating rapidly away from the surface. As a result, the land is warmer than the water during the day and cooler at night. During the morning, the nocturnal (stable) surface boundary layer gradually erodes as air begins to rise over the warm land, i.e. the development of an unstable layer close to the ground, known as the thermal internal boundary layer (TIBL). The cooler air from the ocean flows in to replace it (i.e. the sea-breeze). However, the unmodified ocean air may develop an elevated inversion cap above the warm air over land. At night, land surfaces usually cool faster than the neighbouring water bodies, reversing the temperature gradient that was present during the day – the result is a land breeze. Cool air from land flows out to sea at low levels, warms, rises, and returns aloft toward land (anti-land-breeze) where it eventually descends to close the circulation (Preston-Whyte & Tyson, 1988). The influence of land-sea interaction on local meteorological conditions will only influence wind erodible sources located near the coast.

2.4.3   *Wind speeds in South Africa*

Cape Point in the Western Cape is the windiest place in South Africa according to the South African Weather Services, with an average wind speed of 14.1 m s^{-1} and 42.1% of the wind speeds greater than 8 m s^{-1}. The strongest wind gust recorded in South Africa was 51.7 m s^{-1} (186 km hr^{-1}) at Beaufort West in the Western Cape (SAWS, 2013).

Maximum hourly wind velocities of more than 7.9 m s^{-1} are rare in windstorms over the South African Highveld, but wind gusts of as high as 36.1 m s^{-1} have been recorded (Blight & Amponsah da Costa, 2001). Goliger *et al*. (2009) reported a gust factor of 2.0 for the interior of South Africa to correct for the 2-3 second gusts in hourly mean wind speeds, in relation to 1.6 for coastal areas (Kruger *et al*., 2013). These infrequent gusts, typically lasting for only a few seconds to a few minutes, are the main cause of wind erosion from mine waste and tailings storage

facilities. Site-specific meteorological data is therefore of the essence to accurately quantifying wind-blown dust from small-scale sources.

Kruger *et al*. (2013) analysed 5-minute wind data from 76 weather stations in South Africa to characterise the strong wind climate of the country. The study confirmed the intricate pattern of the strong wind climate in the country, which is mainly influenced by meso-scale thunderstorms and synoptic scale frontal systems. The proposed 1:50 year quantiles of annual maximum gusts indicated a general decrease from the south to the north, with the Eastern Cape the area with the highest values. The annual maximum gusts over the interior plateau range between 30-40 m s^{-1}. The proposed 1:50 year quantiles of annual maximum hourly mean wind speeds reflected a similar trend across the country with the interior plateau ranging between 15-25 m s^{-1}.

2.5   Dispersion Modelling

Dispersion models compute ambient concentrations as a function of source configurations, emission strengths and meteorological characteristics, thus providing a useful tool to ascertain the spatial and temporal patterns in the ground level concentrations arising from the emissions of various sources. Whereas ambient monitoring provides actual ambient concentrations for specific pollutants at set locations, atmospheric dispersion models can be used to simulate any number of pollutants and determine the impacts at any location within the modelling domain (MFE, 2004).

Increasing reliance has been placed on ground level air pollution concentration estimates from models as the primary basis for environmental and health impact assessments, risk assessments and determining emission control requirements. In the selection of a dispersion model it is important to understand the complexity of the dispersion potential of the area (i.e. the terrain and meteorology), and the potential scale and significant significance of potential effects (i.e. other sources that might have an influence on the ground level concentrations) (MFE, 2004).

Health risk assessment is the evaluation of the probability that exposure to a certain air pollutant will result in a given adverse effect in an individual or defined population. Air quality impact assessments typically follow either a qualitative or quantitative approach; characterising the baseline air quality and applying dispersion models to assess the significance of ground level concentrations. The World Bank Group (WBG) International Finance Corporation (IFC) requires internationally recognised or comparable dispersion models to be used in impact assessments. The dispersion modelling methodology should be based on local atmospheric, climatic and air quality data and include source data and emission rates as quantified through recognised methods (IFC, 2007).

The establishment of an emissions inventory comprises the identification of sources of emissions, and the quantification of each source's contribution to ambient air pollution concentrations. Strong links exist between emissions inventories, monitoring and modelling data (MFE, 2001). Coupling emission rates with dispersion models provides a useful tool to determine compliance with ambient air quality standards, to assist in health and environmental risk assessment and to provide information for monitoring network design. The combination is also a useful tool in assessing source contributions to air quality concentrations (Figure 4) (MFE, 2004; MFE, 2001). Kon *et al.* (2007) confirmed the value of linking a wind erosion model with a dispersion model to determine the environmental impacts from industrial wind erosion.

The significance of wind-blown dust from gold tailings storage facilities on human health has been proven in recent research (Ojelede *et al*., 2012; Maseki, 2013). Not only is there concern about how air quality affects human health, but also the impact on ecosystems and crops (National Research Council, 2001).
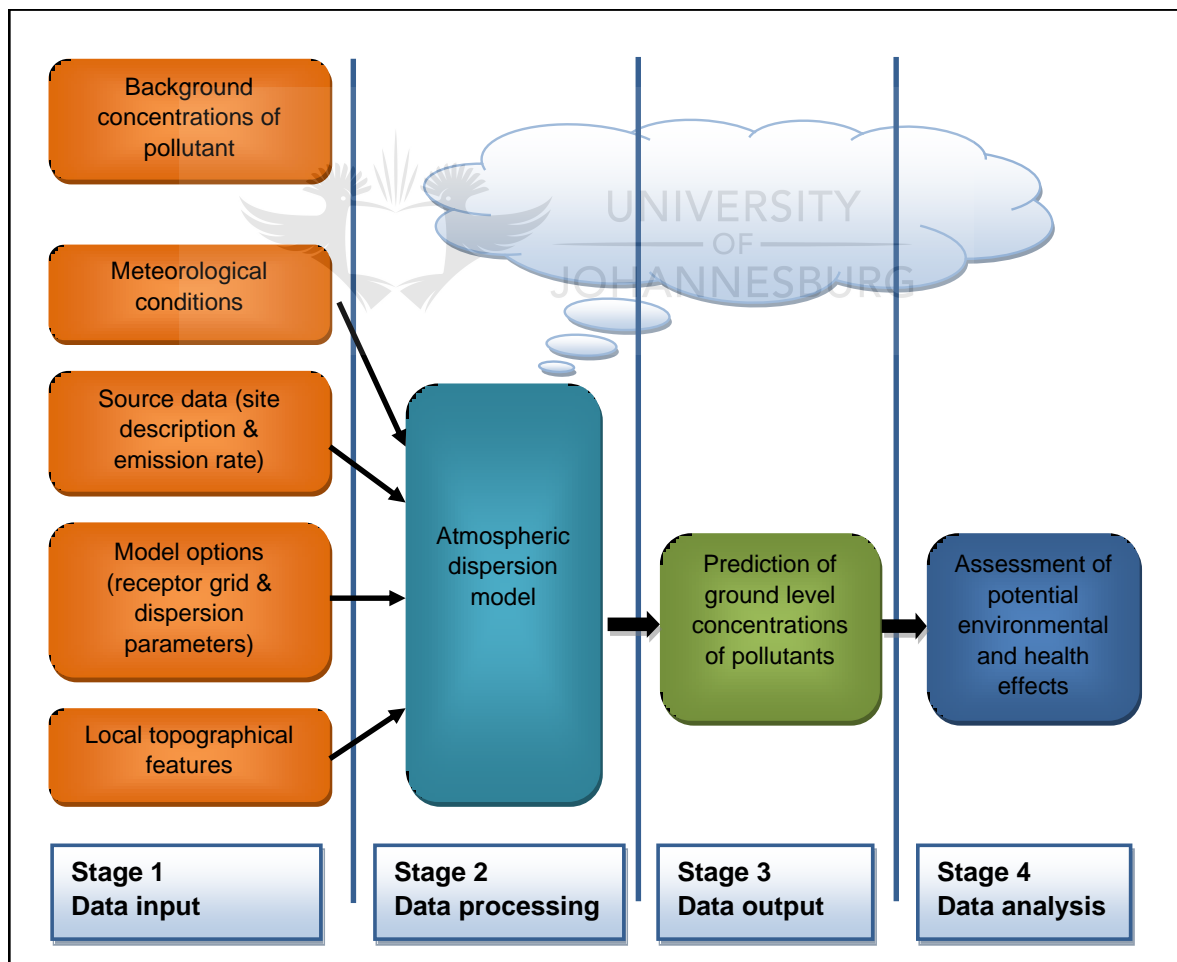
Figure 4: **Overview of air pollution modelling procedure (MFE, 2004).**

Gaussian plume models are best used for near-field applications where the steady-state meteorology assumption is most likely to apply. The most widely used Gaussian plume model is the AERMET/AERMOD dispersion model suite – the regulatory model of the US EPA. The AERMET/AERMOD suite was developed, with the support of the AMS/EPA Regulatory Model Improvement Committee (AERMIC), whose objective was to include state-of-the-art science in regulatory models.

- AERMOD is an advanced new-generation model, designed to predict pollution concentrations from continuous point, flare, area, line, and volume sources. AERMOD offers new and potentially improved algorithms for plume rise and buoyancy, and the computation of vertical profiles of wind, turbulence and temperature, but retains the single straight-line trajectory limitation (Hanna *et al*., 1977).

- AERMET is a meteorological pre-processor for AERMOD, using both surface and upper air data. Input data can be taken from hourly cloud cover observations, surface meteorological observations and twice-a-day upper air soundings. Output includes surface meteorological observations and parameters and vertical profiles of several atmospheric parameters (Hanna *et al*., 1977).

- AERMAP is a terrain pre-processor designed to simplify and standardise the input of terrain data for AERMOD. Input data includes receptor terrain elevation data that can be recorded as digital terrain data. Output includes locations and height scales for each receptor – i.e. elevations are used for the computation of airflow around hills (Hanna *et al*., 1977).

Unlike Gaussian-puff models, the Gaussian-plume models cannot account for spatial varying wind fields and does not accurately reflect the influences of topography or other factors. Typically, these models are reported to have an uncertainty range of -50% to 200%, improving with higher wind speeds and during neutral atmospheric conditions (Hanna *et al*., 1977).

These uncertainties in the model results are a combination of errors in the model physics and the stochastic uncertainty – including source term and associated emission strengths, measured concentrations, and meteorological data. Solutions depend on the covariance function of noise – in time and in space (Friederichs *et al*., 2009). This implies that the variability between modelled concentrations and measured concentrations can be large depending on the location of the ambient monitoring station in relation to the source of emissions, and the sample size. Errors in data input can be a major contributor to the uncertainty in modelled results, translating directly into the error magnitude of the model results (MFE, 2004; MFE, 2001).

2.5.1 Meteorological data requirements

AERMOD requires two specific input files generated by the AERMET pre-processor, and designed to be run as a three-stage processor operating on three types of data (upper air data, on-site measurements, and the national meteorological database).

2.5.2 Preparation of source data

AERMOD is able to model point, area, volume, pit and line sources. Sources such as tailings- and ash-storage facilities can be modelled as area sources. Dimensions and height are both required for input to the model, together with an emission rate in $g\,m^{-2}\,s^{-1}$. The model allows for varying emissions to be included – such as an hourly emission rate file where an emission rate for every hour of the meteorological data period is included.

2.5.3 Preparation of receptor grid

Gaussian-plume models are most accurate at distances between 100 m and 10 km from the source and are therefore widely applied to mining and plant operations. The model allows for evenly or unevenly spaced Cartesian or Polar grids, with the former most widely applied in air dispersion modelling.

2.5.4 Topographical influences

Topography, especially near the air pollution source, can significantly influence the wind speed, wind direction and turbulence characteristics, and subsequently the pollution dispersion potential. Gaussian-plume models are less accurate in complex terrains.

3 Functional Dependence Analysis of Influencing Variables on Selected Dust Emission Schemes

Extensive research on the physics of wind erosion came about over the past decade compelling the re-evaluation of previously applied techniques. This chapter investigates the various horizontal and vertical dust-flux models and the sensitivity around the variations of the several input parameters that determine the threshold velocity and the magnitude of the flux once the threshold velocity has been exceeded.

3.1 Data Selection

3.1.1 Particle size distribution

Soils prone to wind erosion contain particles of various sizes including: clay-size ($d < 2.5$ µm); silt size ($2.5 < d < 60$ µm); and sand-sized particles ($d > 60$ µm). Clay and silt sized particles are not easily mobilised by wind because of the inter-cohesive forces binding it together. Sandblasting caused by saltation bombardment is needed to disaggregate the finer particles and inject these into the air (Zender *et al.*, 2003).

When the wind velocity is strong enough to overcome the resisting forces of particle size and weight, or inter-particle cohesion, the particle is moved and may either slide, roll, bounce (saltation) or go into suspension. Large particles (of 500 µm or more) are usually too heavy to be lifted and will role and slide – this movement is called surface creep. Saltation is when sand particles are lifted and bounce across the surface during periods of high wind speeds. This occurs mainly within 1.5 m from the surface and the particle sizes range between 70 and 500 µm. Particles smaller than 70 µm can be suspended into the air and remain there for longer (Pye, 1987).

For the purpose of testing the sensitivity of the various input parameters (Table 1), a single dataset was derived from the Friedman and Sanders (1978) Size Class Terminology (Table 2).

Six particle sizes were selected for use in the sensitivity analysis including: $d = 250$ µm and $d = 75$ µm as representative of sand particles; $d = 45$ µm, $d = 20$ µm and $d = 10$ µm as representative of silt particles; and $d = 2$ µm representing clay particles – these six classes are shaded in Table 2. Clay particles, where $d < 2$ µm, fall within the respirable dust fraction, typically given as $d < 2.5$ µm. A particle size of $d = 10$ µm (called thoracic dust) is, together with respirable dust, associated with health impacts; $d = 75$ µm is regarded as the optimal particle size for saltation to occur (Iversen & White, 1982).

Table 2:   The Friedman and Sanders (1978) modified version of the Udden-Wentworth particle size scale used in sedimentology (Shao, 2008).

Size (*d*) (mm)	Size class terminology of Friedman and Sanders (1978)	Common name
1 024 – 2 048	Very large boulders	Gravel
512 – 1 024	Medium boulders	
256 – 512	Small boulders	
128 – 256	Large cobbles	
64 – 128	Small cobbles	
32 – 64	Very coarse pebbles	
16 – 32	Coarse pebbles	
8 – 16	Medium pebbles	
4 – 8	Fine pebbles	
2 – 4	Very fine pebbles	
1 – 2	Very coarse sand	Sand
0.5 – 1	Coarse sand	
0.25 – 0.5	Medium sand	
0.125 – 0.25	Fine sand	
0.063 – 0.125	Very fine sand	
0.031 – 0.063	Very coarse silt	Silt
0.016 – 0.031	Coarse silt	
0.008 – 0.016	Medium silt	
0.004 – 0.008	Fine silt	
0.002 – 0.004	Very fine silt	
< 0.002	Clay	Clay

Notes: The shaded size classes are the particle sizes selected for use in the sensitivity analysis.

3.1.2   *Generic wind speed*

A generic wind speed dataset was compiled to provide comparative horizontal saltation and vertical dust-flux rates. The selected wind speeds ranged between 4.9 and 23.3 m s^{-1}. The equivalent friction velocities were calculated using the logarithmic wind profile applicable under neutral atmospheric conditions of:

$$u(z) = \frac{u_*}{K} \ln\left(\frac{z}{z_0}\right) \tag{1}$$

where K is the von Karman constant (0.4) and z_0 is the aerodynamic roughness length.

A roughness length of 0.0009 m was used, based on the field data from Gillette *et al*. (1982), for a soil sample comprising of 20% clay, 44% silt and 36% sand. The resulting threshold velocities ranged between 0.2 and 1 m s^{-1}.

The wind profiles will differ under unstable and stable conditions. A slightly modified version of the neutral equation can be used when the atmosphere is not neutral:

$$u(z) = \frac{u^*}{K} \varphi \left(\frac{z}{L}\right) \qquad (2)$$

where:

STABLE ($z/L > 0$)	NEUTRAL ($z/L = 0$)	UNSTABLE ($z/L < 0$)
$\ln(\frac{z}{z_o}) + \frac{\beta}{L}(z - z_o)$	$\ln(\frac{z}{z_o})$	$2(\arctan(b) - \arctan(b_0)) - \ln \frac{(b+1)(b_0 - 1)}{(b-1)(b_0 + 1)}$
		where $\quad b = (1\frac{\gamma}{L}z)^{1/4}$
		$b_0 = (1 - \frac{\gamma}{L}z_0)^{1/4}$
		and $\gamma = 15$ (Businger *et al.*, 1971)

The Monin-Obukhov length (*L*) is the buoyancy length scale, providing a measure of the importance of buoyancy generated by the heating of the ground and the mechanical mixing generated by the frictional effect of the earth's surface. Physically, this can be thought of as representing the depth of the boundary layer within which mechanical mixing is the dominant form of turbulence generation (CERC, 2004). The parameters used to define *L* are: the friction velocity (u^*); von Karman's constant; gravitational acceleration; ambient air temperature and the kinetic heat flux.

The horizontal dust-flux is proportional to u^3_* and thus using the correct u^* is very important in estimating wind erosion (Burger, 2010).

3.2 Horizontal Saltation Flux Models

Over the years, a number of analytical models have been developed to describe the horizontal flux, also referred to as the saltation flux (Table 3). Most of these equations use either friction velocity or threshold friction velocity as a function of the emission rate (Shao, 2008).

Table 3: **Summary of different horizontal saltation flux models for calculating the wind-generated saltation-flux *Q* from aggregate surfaces (Shao, 2008).**

Source	Expression for *Q*	Constant Value
Bagnold (1937)	$C_0 \left(\dfrac{d}{D}\right)^{1/2} \dfrac{P_a}{g} u_*^3$	D = 250 μm C0 = 1.5 (uniform sand) C0 = 1.8 (natural granted sand) C0 = 2.8 (poorly sorted sand)
Zingg (1953)	$C_0 \left(\dfrac{d}{D}\right)^{3/4} \dfrac{P_a}{g} u_*^3$	D = 250 μm C0 = 0.83
Kawamura (1964)	$C_0 \dfrac{P_a}{g} u_*^3 \left(1 - \dfrac{u_t^*}{u^*}\right)\left(1 + \dfrac{u_t^*}{u^*}\right)^2$	C0 = 1.8 to 3.1
White (1979)	$C_0 \dfrac{P_a}{g} u_*^3 \left(1 - \dfrac{u_t^*}{u^*}\right)\left(1 + \dfrac{u_t^*}{u^*}\right)^2$	C0 = 2.6
Owen (1964)	$C_0 \dfrac{P_a}{g} u_*^3 \left(1 - \dfrac{u_t^{*2}}{u_*^2}\right)$	C0 = $0.25 + \dfrac{\omega t}{3u_*}$
Lettau and Lettau (1978)	$C_0 \left(\dfrac{d}{D}\right)^{1/2} \dfrac{P_a}{g} u_*^3 \left(1 - \dfrac{u_t^*}{u^*}\right)$	C0 = 4.2

3.2.1 *Functional dependence of saltation models to different particle sizes*

Horizontal mass flux depends on a number of parameters as indicated (equations in Table 3). These parameters include: a constant (C_0) (that varies depending on the model); relative density of air (p_a); particle grain size (*d*); acceleration rate because of gravity (*g*); threshold velocity (u^*) and threshold friction velocity (u^*_t). The schemes are fundamentally similar, all using the threshold velocity to the power of three (u^3_*). The main difference in the later schemes is the incorporation of the threshold friction velocity (u^*_t). The threshold friction velocity (u^*_t) in turn depends on: particle density (p_p); relative density of air (p_a); acceleration rate because of gravity (*g*); and particle grain size (*d*).

The constant value (C_0) and relative density of air (p_a) would remain constant in the natural environment. Emphasis is therefore placed on the parameters that could vary, depending on the source material and prevailing environmental conditions (viz. weather).

The first set of analyses, applied the six horizontal saltation-flux models to the six particle size categories (i.e. 250 μm; 75 μm; 45 μm; 20 μm; 10 μm and 2 μm) and the varying threshold velocities (u^*), based on the generic wind velocities (Section 2.2).

The second set of analyses looked at the functional dependence of each horizontal saltation flux model on the threshold friction velocity (u^*_t) in relation to varying threshold velocities (u^*).

Thirdly, the sensitivity of the threshold friction velocity (u^*_t) to the various input parameters was tested. Initially the process compared the three different methods used to quantify u^*_t and followed by testing the sensitivity of each scheme to the various input parameters.

3.2.2   Saltation flux model functional dependence

The first analysis assesses the variation in the prediction of Q between the different saltation flux models using the same input parameters. The horizontal saltation flux (kg m^{-1} s^{-1}) for the six particle sizes, in relation to a constant friction velocity (u^*) of 1 m s^{-1} and a constant threshold friction velocity (u^*_t) of 0.2 m s^{-1} for the different models, is presented in Figure 5. The variation of Q with particle size differed qualitatively and quantitatively: the first three models did not include a size-dependent term; the later three models showed increasing Q with particle size, along similar trends but differing by a factor of up to x5 in magnitude.
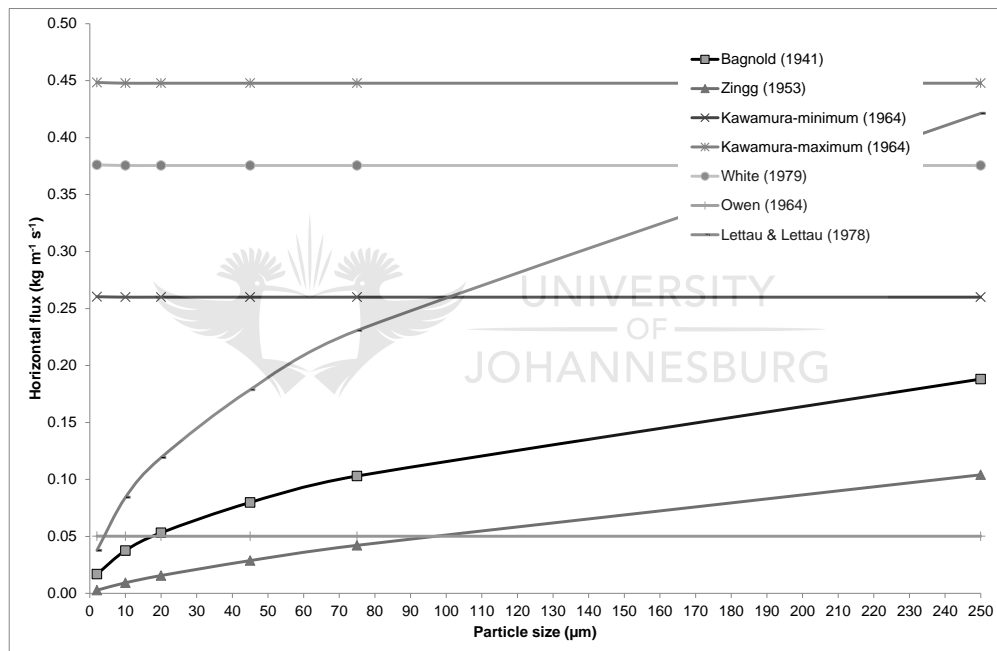
Figure 5:   **Comparison of the horizontal saltation flux predictions for six different particle sizes using a friction velocity of 1 m s^{-1}.**

The models of Bagnold (1941) and Zingg (1953) did not use u^*_t whereas the later models all included u^*_t (Table 2). The models of Kawamura (1964), Owen (1964) and White (1979) only accounted for the particle size (d) indirectly through its dependency on u^*_t, therefore their results showed no variation between the particle sizes for u^* and u^*_t. Horizontal saltation flux rates (as calculated with Owen's model) are nine times lower than those calculated by the Kawamura (1964) model – using the maximum ($C_0 = 3.1$) – and five times lower using the minimum constant ($C_0 = 1.8$). The models of Bagnold (1941), Zingg (1953) and Lettau and Lettau (1978) are directly related to the particle size (d) and resulted in an increase in emission rates with increases in particle sizes. Zingg's (1953) model was most sensitive to the particle size variation – with the dust-flux

rate for $d = 250$ µm at a level of 37 times higher than for $d = 2$ µm. Both Bagnold (1941) and Lettau and Lettau (1978) models resulted in the emission rate for $d = 250$ µm being 11 times higher than for $d = 2$ µm.

For varying friction velocities (u^*) and particle sizes (Figure 6), the model of Kawamura (1964), where $C_0 = 3.1$, resulted in the highest saltation flux rates irrespective of the friction velocity and the particle size. For a particle size of 250 µm (Figure 6a), Owen's model (1964) resulted in the lowest emission rate but, when applied to a 75 µm particle size (Figure 6b), Zingg's model (1953) provided a lower emission rate when $u^* > 0.47$ m s^{-1}. The emission rate from Zingg's model was reduced as the particle size decreased. For example, the saltation flux rate, at a friction velocity of 1 m s^{-1}, is 15 times lower for a particle size of 2 µm (Figure 6f) than for a particle size of 75 µm (Figure 6b). Both Bagnold's model (1941) and Lettau and Lettau's model (1978) resulted in a reduction in the emission rate, by a factor of six, for particles sized between 75 µm to 2 µm.

The ratio between the minimum and the maximum saltation flux rates remained the same for all particle sizes tested. The model of Lettau and Lettau (1978) showed the highest sensitivity to friction velocity (u^*), with saltation flux rates 1 814 times higher at $u^* = 1$ m s^{-1} than at $u^* = 0.21$ m s^{-1}, irrespective of particle size. The models of Bagnold (1941) and Zing (1954) were less sensitive to wind speed, with the lowest variation between $0.21 < u^* < 1$. Owen's (1964) model showed the second highest sensitivity to u^*, with a difference of 1 115 times between the minimum and the maximum u^* in the saltation flux rate. Kawamura (1964) and White (1979) showed a higher emission rate 685 times at $u^* = 1$ m s^{-1} than at $u^* = 0.21$ m s^{-1}.
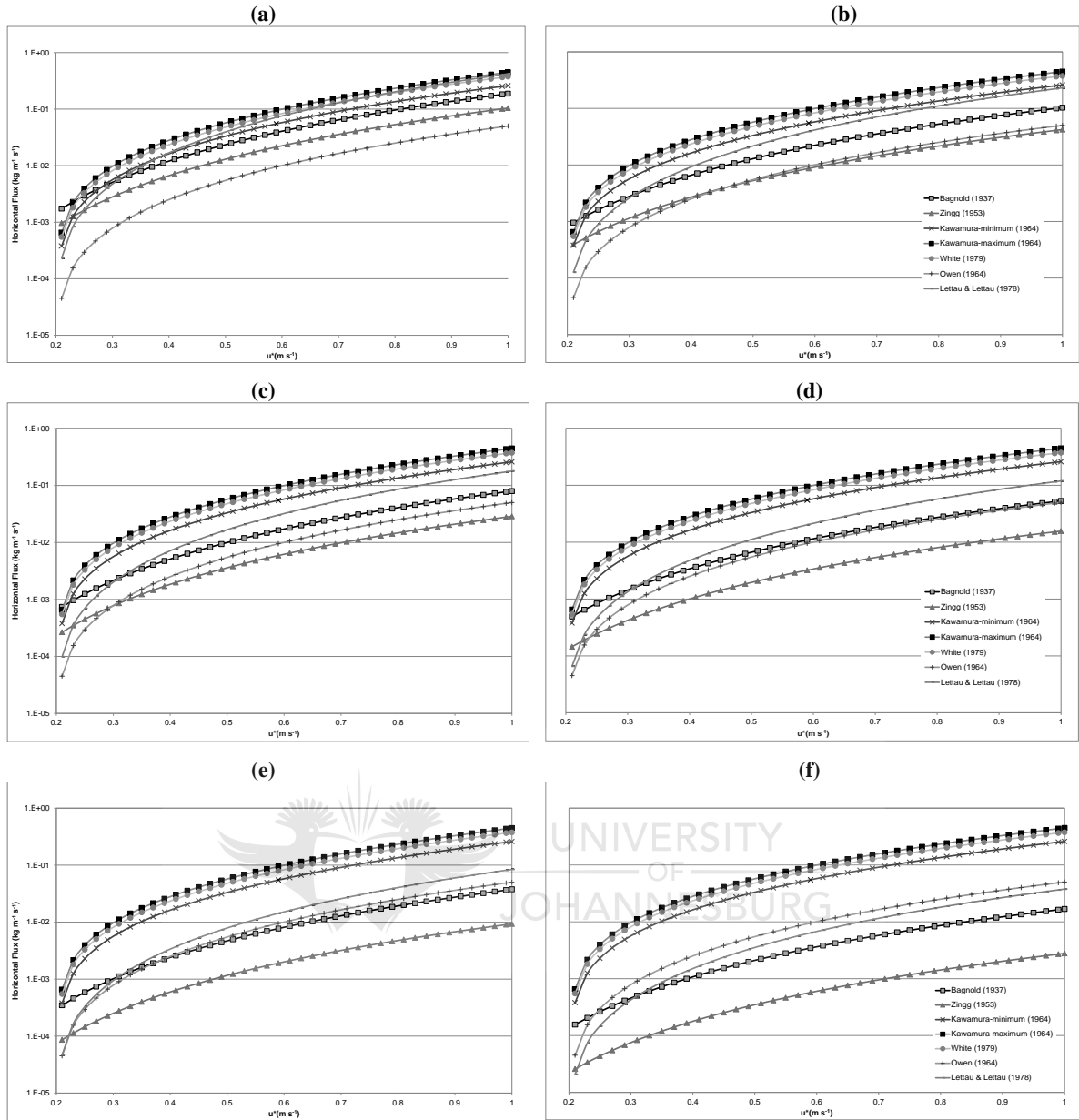
Figure 6: **Comparison of horizontal saltation flux predictions for particles with a diameter of**
(a) *d* = 250 µm; (b) *d* = 75 µm; (c) *d* = 45 µm; (d) *d* = 20 µm; (e) *d* = 10 µm and (f) *d* = 2 µm.

3.2.3 Saltation flux models dependence on the threshold friction velocity

The sensitivity of each of the models to both the threshold friction velocity (u^*_t) and the particle size was tested. For wind erosion to occur, the wind speed needed to exceed a certain threshold – called the threshold friction velocity (u^*_t). This threshold is related to the forces of gravity and inter-particle cohesion that act to resists particle mobilisation. Surface properties – such as soil texture, soil moisture and vegetation cover – influence the threshold friction velocity. Conversely, the friction velocity or wind shear at the surface is related to the atmospheric flow conditions and surface aerodynamic properties. Thus, for particles to become airborne, the wind shear at the surface must exceed the gravitational and cohesive forces acting upon them. The threshold friction velocity (u^*_t) is therefore primarily a function of the soil surface characteristics rather than the particle size. The particle size can, however, be used to determine u^*_t under ideal conditions (Shao, 2008).

Bagnold (1941) established a relationship – between u^*_t and the mean particle size – to determine the critical threshold velocity at which the particles on a surface will start to move. This is expressed by:

$$u^*_t = A \sqrt{\frac{P_p - P_a}{P_a} g d} \tag{3}$$

where: A = empirical coefficient of 0.129 relating to a Reynolds number of Re > 3.5

p_a = air density (g cm^{-3}) taken as 0.00123 g cm^{-3}

p_p = particle density (g cm^{-3}) based 2.65 g cm^{-3} for quartz

g = gravimetric acceleration (cm s^{-1}) given as 981 cm s^{-1}

d = mean particle diameter (µm)

Bagnold (1941) suggested that the smaller averaged particle sizes ($d < 80$ µm) are more resistant to aerodynamic lift because of the smooth surface, resulting in an increase in u^*_t. Bagnold's expression did not incorporate this as an effect, however – such terms were incorporated in later works (Iversen & White, 1982; Lu & Shao, 1999).

Numerous follow-up experiments – by among others Chepil and Woodruff (1963), Belly (1964) and Iversen *et al.* (1976) – confirmed this relationship between the particle diameter and u^*_t. The later studies by Sagan and Bagnold (1975), Iversen *et al.* (1976) and Iversen and White (1982) suggested that the upturn point of u^*_t below around $d < 80$ µm is primarily because of stronger inter-particle cohesion rather than because of the Reynolds number effects (Pye, 1987). Gravitational forces are therefore more important for movement of larger particles, with the cohesive forces dominating smaller particles (Lu & Shao, 2001; Shao, 2008).

Iversen and White (1982) developed an expression between u^*_t and mean particle size to allow for the effect of inter-particle cohesion forces when expressed as a function of the Reynolds number (Marticorena & Bergametti, 1995; Lu, 1999).

For 0.03 < Re < 10, the expression is:

$$u^*_t(d) = \frac{0.129 \times K}{(1.928 \times Re^{0.092} - 1)^{0.5}}$$ (4),

whereas for Re > 10, the expression is:

$$u^*_t(d) = 0.129 \times K[1 - 0.0858\, exp(-0.0617(Re - 10))]$$

where: $K = \left(\frac{P_p g d}{P_a}\right)^{0.5} \times \left(1 + \frac{0.006}{P_p g d^{2.5}}\right)^{0.5}$ and

$Re = 1331\, d^{1.56} + 0.38$

The increases in u^*_t for smaller particle sizes, (i.e. d less than 75 μm) as indicated by the field measurements of Gillette (1978) because of the inter-particle cohesion forces, are shown in Figure 7. The Greeley-Iversen scheme is widely accepted and used in several wind erosion models (Marticorena & Bergametti, 1995; Shao & Lu, 2000; Alfaro & Gomes, 2001; Shao, 2004) because this scheme has been verified through high-quality wind tunnel measurements.

Lu (1999) pointed out that the approach by Greeley-Iversen, where the inter-particle cohesive force is proportional to $d^{1/2}$, may be physically incorrect and was more likely to be proportional to d. Shao and Lu (2000) developed a simpler expression for u^*_t through the explicit treatment of inter-particle cohesive forces. The combined cohesive force – including van der Waals forces, capillary forces, chemical binding and electrostatic forces – depends on the surface roughness elements, soil moisture and soil aggregation. The scheme by Shao and Lu (2000) accounted for viscous effects through a function incorporating the Reynolds number (Re). It took into account the increase in the gravitational force, through a combination of particle size (d), particle density (p_p) and air density (p_a). The expression (Figure 7) is as follows:

$$u^*_t(d) = \sqrt{B\left(\sigma_p g d + \frac{\gamma}{P_p d}\right)}$$ (5)

where: σ_p = particle-to-air density ratio

γ = vary between 1.65 x 10^{-4} kg s^{-2} and 5 x 10^{-4} kg s^{-2}

B = ranges between 0.01 and 0.04 with 0.0123 providing a good fit with measured data

The Bagnold (1941) scheme showed a linear relationship between a decrease in the threshold friction velocity (u^*_t) relative to a decrease in the mean particle size (d). The Iversen and White (1982) scheme and Lu and Shao (2000) scheme resulted in a decrease of u^*_t, with a decrease in the mean particle size (d) for the larger particles because of gravimetric forces. According to the Iversen-White approach, u^*_t starts to increase with a decrease in particle size – where d < 75 μm –

but, for particle diameters smaller than 10 µm, the deviation in u^*_t increases. The Lu-Shao scheme expresses u^*_t to be at a minimum when $d = 100$ µm; thereafter it increases with a decrease in d.
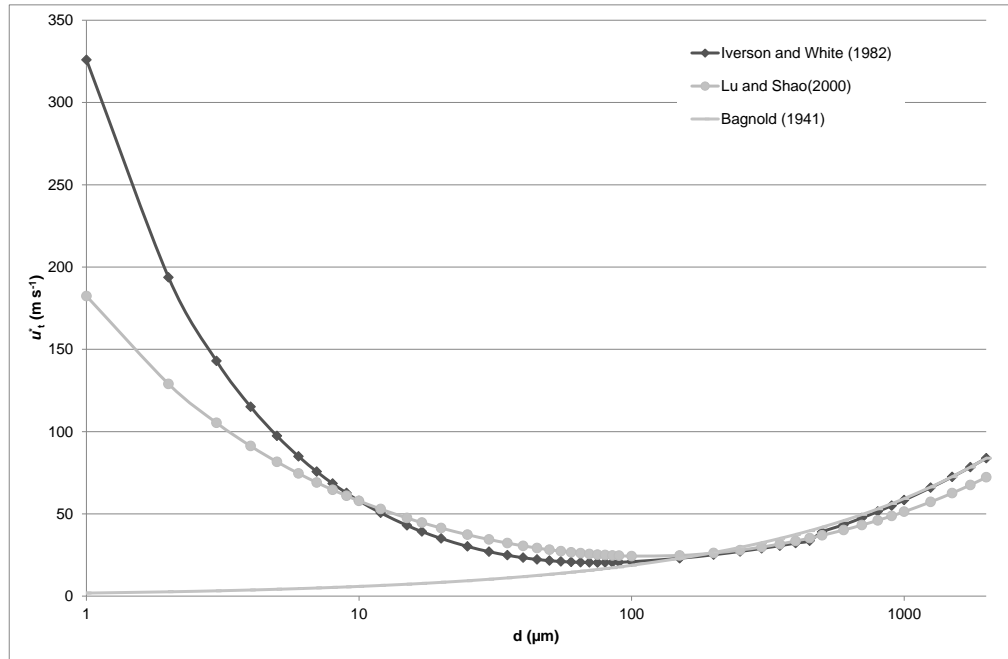
Figure 7: **Relationship of threshold friction velocity (u^*_t) to the particle diameter (d) per the schemes from Bagnold (1941); Iversen and White (1982); and Lu and Shao (2000).**

For testing the sensitivity of the six dust-flux models to a varying threshold friction velocity, u^*_t was calculated, with all other input parameters remaining constant, using the equation from Iversen and White (1982) (Equation 1). Friction velocities (u^*), ranging between 2 m s^{-1} and 6 m s^{-1}, were selected to ensure positive horizontal dust-flux rates results for all particle sizes. Figure 8 shows the difference, in u^*_t of 9.5 times between a clay particle (2 µm) and a silt particle (75 µm).

The models of Bagnold (1941) and Zingg (1953) showed constant reduction in horizontal flux relative to the decrease in particle size (Figure 8). The approaches by Kawamura (1964), White (1979) and Owen (1964) reflected the same horizontal flux rate increase between all particle sizes because of an increase in u^*_t – with the exception of $d = 2$ µm, which showed a sensitivity towards lower friction velocities ($u^* < 3.1$ m s^{-1}). The Lettau and Lettau (1978) and Owen (1964) models were most sensitive to u^*_t at small particle sizes and changes in the horizontal saltation flux rate for $d < 5$ µm was noted.
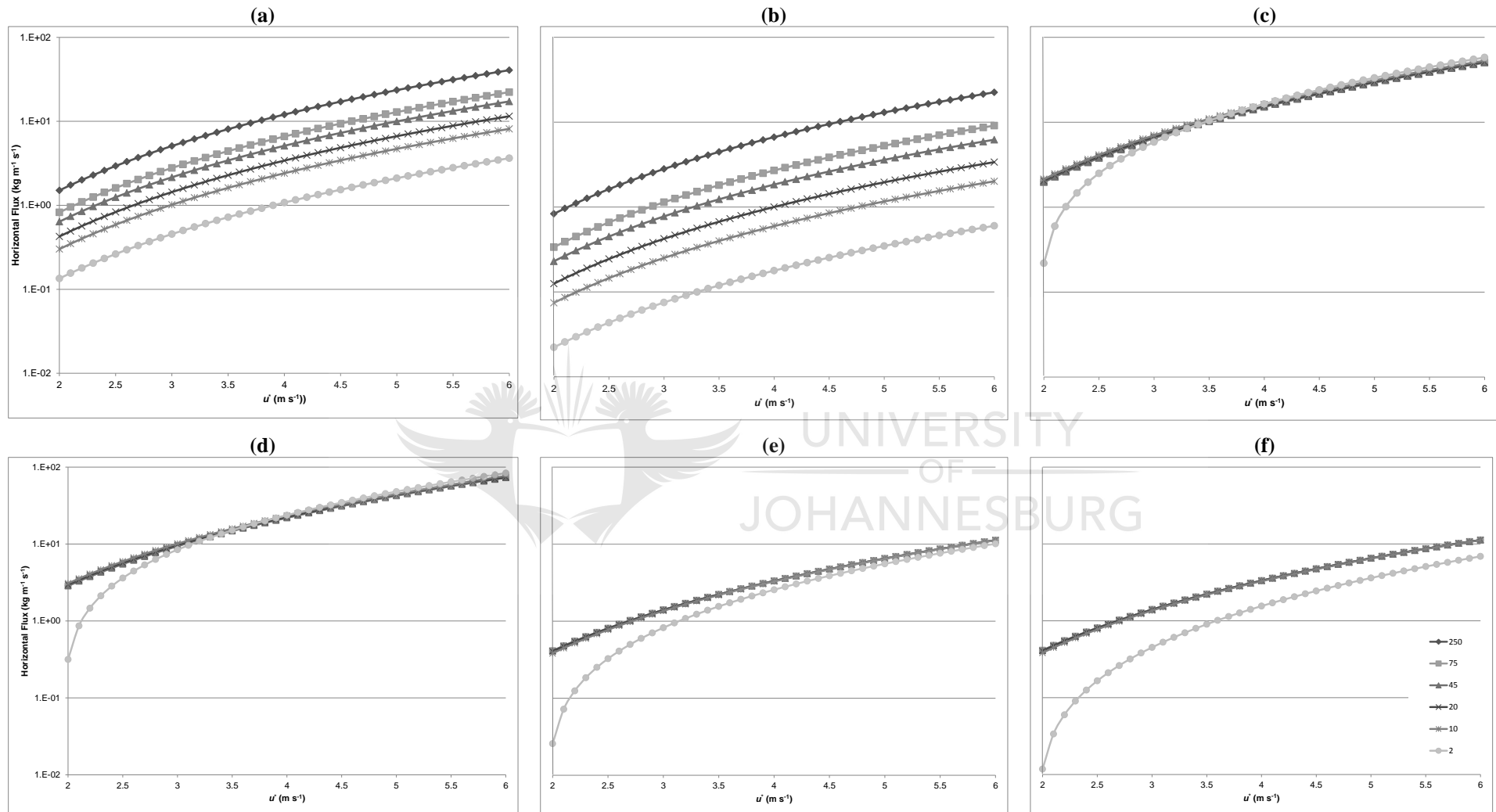
Figure 8: Comparison of the influence of threshold friction velocity ($u*_t$) and particle size distribution on the horizontal dust-flux models of (a) Bagnold (1941); (b) Zing (1953); (c) Kawamura (1964) maximum C_0; (d) White (1979); (e) Owen (1964) and (f) Lettau & Lettau (1978).

3.2.4   Sensitivity of the threshold friction velocity

The latest and most widely applied horizontal saltation flux models of Owen, White and Lettau and Lettau prompted the necessity to test the sensitivity of u^*_t in relation to its input parameters. In natural environments, the most significant influencing factor to u^*_t is the nature of the soil surface. Non-erodible elements (such as vegetation cover, pebbles, soil moisture and surface crust) increase the resistance of the surface material to disturbance, requiring a stronger force to move the surface particles.

Drag partition

The density of roughness elements on the surface affects the shear stress or momentum flux. Drag partition is the difference between the pressure drag from the wind on the roughness elements (Shao, 2008). Raupach (1991) developed a simplified approach accounting for the wakes around the roughness element (with limitations when applied to an increased roughness density). The aerodynamic roughness length (z_0), a measure of the terrain roughness as seen by the surface wind, can be an alternative approach to drag partitioning (Marticorena & Bergametti, 1995). Using the roughness length (z_0) to estimate the friction velocity (u^*) is discussed at Section 3.1.2, Equation 1. There is a close relationship between the roughness length (z_0) and frontal-area index or roughness density (λ), which describes the characteristics of the surface roughness elements. The relationship between Marshall's (1971) observed efficient friction velocity ratios and roughness lengths indicates that z_0 could be a relevant parameter for drag partitioning (Equation 5). MacKinnon *et al.* (2004) suggested a value of 12 255 cm (instead of 10 cm) applied for desert vegetation types, based on field measurements recorded in the central Mojave Desert, USA. A method to quantify the smooth roughness length (z_{0s}), instead of measuring, is given by $D/30$, where D is the mean particle size in the range of the erodable particles (Marticorena & Bergametti, 1995; Laurent *et al.*, 2006). The limitation of this scheme is that it only applies to solid obstacles and to small wakes ($z_0 <$ 1 cm) (Darmenova *et al.*, 2009).

$$R(z_{0,}z_{0s}) = 1 - \frac{ln\left(\frac{z_0}{z_{0s}}\right)}{ln\left[0.35\left(\frac{10}{z_{0s}}\right)\right]}$$

$$R(z_{0,}z_{0s}) = 1 - \frac{ln\left(\frac{z_0}{z_{0s}}\right)}{ln\left[0.35\left(\frac{12255}{z_{0s}}\right)\right]} \qquad (6)$$

where: D = the mean particle size within the erodible *psd*

z_0 and z_{0s} are in cm.

The *Owen effect* accounts for the increase in aerodynamic roughness length because of the development of the saltation layer, which acts as an additional sink of atmospheric momentum

during wind erosion events (Burger, 2010; Shao, 2004). The saltation roughness length can therefore be expressed as:

$$z_{0s} = c_{z0} \frac{u_*^2}{2g} \tag{7}$$

where the coefficient c_{z0} is found to be around 0.02 based on Owen's data (1964).

A drag partition correction suggested by Raupach *et al.* (1993) links the shear stress threshold of the bare erodible surface to the total shear stress of the surface, accounting for all roughness elements. The double drag effect caused by larger roughness elements − such as vegetation and smaller roughness elements − can be accounted for through parameterisation of λ, β, *m* and σ for both barren and vegetated surfaces (Darmenova *et al.*, 2009). This scheme can be expressed as:

$$R(\lambda) = (1 - \sigma_v m_v \lambda_v)^{-0.5} (1 + m_v \beta_v \lambda_v)^{-0.5} \left(1 - \sigma_B \, m_B \, \frac{\lambda_B}{1-A_v}\right)^{-0.5} \left(1 + m_B \, \beta_B \, \frac{\lambda_B}{1-A_v}\right)^{-0.5}$$

$$\tag{8}$$

where: σ = ration between the basal and frontal are of roughness elements.

m = accounts for the spatiotemporal variations of the stress of the underlying surface and ranges between 0 and 1.

β = the ratio of the drag coefficient for a single roughness length.

λ = the roughness density of the non-erodible elements.

Darmenova *et al.* (2009) indicated σ to be 1 for barren surfaces and 1.45 for vegetated surfaces; *m* is 0.5 (barren) and 0.16 (vegetated); with β provided as 90 for barren surfaces and 202 for vegetated surfaces.

Soil moisture

Soil moisture acts as a binding factor influencing the inter-particle cohesion and u_t^*. Soil moisture consists of molecular adsorption of water on particle surfaces and the capillary forces of free moisture between particle surfaces. The inter-particle capillary force is far stronger than the inter-particle force because of adsorption (*w'*) and therefore the main influencing force responsible for increasing u_t^*. (Fécan *et al.*, 1999; Shao, 2008). Only when the total soil moisture (*θ*) is more than the maximum adsorbed amount of water on the particle surface will u_t^* be affected (Marticorena & Bergametti, 1995). Belly (1964) showed, through wind tunnel experiments, that u_t^* can double with a 0.6 % increase in moisture when compared with dry sand. Experiments conducted by Chepil and Woodruff (1965) on silt loam soils also indicated a significant increase in u_t^*, with a moisture increase of less than 0.71% (Pye, 1987).

The Bagnold scheme can be modified – to account for moisture – as suggested by Belly (1964):

$$u_{t=}^* = A \sqrt{\frac{P_p - P_a}{P_a}} gD \ (1.8 + 0.6 \log 10 \, \theta) \tag{9}$$

where: θ is the total soil moisture as %.

The limitation of this approach is that it is applicable to sand, and therefore only accounts for the effect of capillary forces: loam and clay soils can also adsorb moisture.

McKenna Neuman and Nickling (1989) developed a model using the moisture tension to determine the threshold friction velocity for wet soils. This again applied to sand – and not to loam and clay soils. The effect of soil moisture on the inter-particle cohesive force, as proposed by McKenna Neuman (2004), affects γ per the Shao and Lu (2000) scheme. McKenna Neuman found that:

$$u_t^* = \sqrt{A_2^2 Re \left(\sigma_p gD + \frac{\gamma'}{P_p D^2} \right)} \tag{10}$$

where: $\gamma' = 10^{-8} - |\Delta P|(1.15 \times 10^{-8}d - 5.8 \times 10^{-5}d^2)$

$|\Delta P|$ = capillary suction pressure deficit (*Pa*) (the difference between the pressure within the water wedge and the atmospheric pressure)

A_2 = 1.14, 1.06, 1.06 and 1.25 for the particle sizes of 210, 270, 430 and 610 μm respectively

Re = 0.0123

The difficulty with this approach is that $|\Delta P|$ is derived from the surface tension and the difference between: (i) the inverse of the radius of curvature of the outside of the water wedge; and (ii) the inverse of the radius of curvature of the air-water interface. As these latter parameters depend on soil moisture and particle shape, there could be inaccurate quantification of $|\Delta P|$ from natural soils with different shapes or size profiles from those listed in equation 10, parameter A_2 (Fécan *et al*., 1999).

Fécan *et al.* (1999) introduced an empirical relationship between adsorbed moisture (*w'*) and soil clay content (η_c) showing good agreement with experimental data. This approach looked at both the capillary and adsorption of moisture in particles and is applied in the following way:

$$\frac{u_{tw}^*}{u_{td}^*} = 1 \qquad\qquad\qquad for \ w < w' \tag{11}$$

$$\frac{u_{tw}^*}{u_{td}^*} = [1 + 1.21(w - w')^{0.68}]^{0.5} \qquad for \ w > w'$$

where*:*

$$w' = 0.0014(\eta_c)^2 + 0.17(\eta_c) \text{ (\%)}$$

u^*_{tw} = wet erosion threshold velocity (m s^{-1})

u^*_{td} = dry erosion threshold velocity (m s^{-1})

The influences of soil moisture – for four soil moistures – 1%, 2%, 4% and 8% – on the threshold friction velocity for the three schemes are shown in Figure 9. A soil moisture of 1% when compared with dry soil, increases u^*_t by 80% using the modified Bagnold scheme. The moisture relationship as introduced by Fécan was applied to both the Iversen & White and the Shao & Lu schemes and resulted in a 44% increase in u^*_t for a soil with 1% soil moisture increase. By doubling the soil moisture from 1% to 2%, the Bagnold scheme increased u^*_t by 10% and the Iversen & White and the Shao & Lu schemes increased u^*_t by 14%. By doubling the soil moisture from 2% to 4%, and then to 8%, the Bagnold scheme resulted in a 9% and an 8% increase of u^*_t, respectively. For the Iversen & White and the Shao & Lu schemes, u^*_t increased by 17% for 4% moisture and by 20% for 8% moisture.

Particle density

Threshold friction velocity showed little sensitivity to particle density (Figure 10). The minimum and maximum particle densities from the Iversen & White (1982) experimental data – as reported by Lu (1999) – were selected for comparison, together with the particle density for quartz (p_p = 2.65 g/cm³). Relative density of air (p_a) and acceleration rate because of gravity (g) are considered likely to remain similar for the various particle sizes and densities. Figure 10 shows the threshold friction velocity (u^*_t) in relation to the selected particle sizes – based on particle densities of $p_p = 210$ kg m⁻³; $p_p = 2\,650$ kg m⁻³ and $p_p = 11\,350$ kg m⁻³. For the smaller particle sizes ($d < 10$ μm), the particle density has no effect on u^*_t. For $d = 10$ μm, the difference between the $p_p = 210$ kg m⁻³ and $p_p = 2\,650$ kg m⁻³ was 1%, with 3% difference between the lowest density and highest density. The sensitivity to the particle density increased with an increase in particle size. The difference in u^*_t for $d = 75$ μm between $p_p = 210$ kg m⁻³ and $p_p = 11\,350$ kg m⁻³ was a factor of 2.9 when compared with the recorded difference for $d = 250$ μm of 6.5.

Particle densities do not vary significantly between typical sand, loam and clay soils, and can therefore be disregarded as an important influencing parameter.
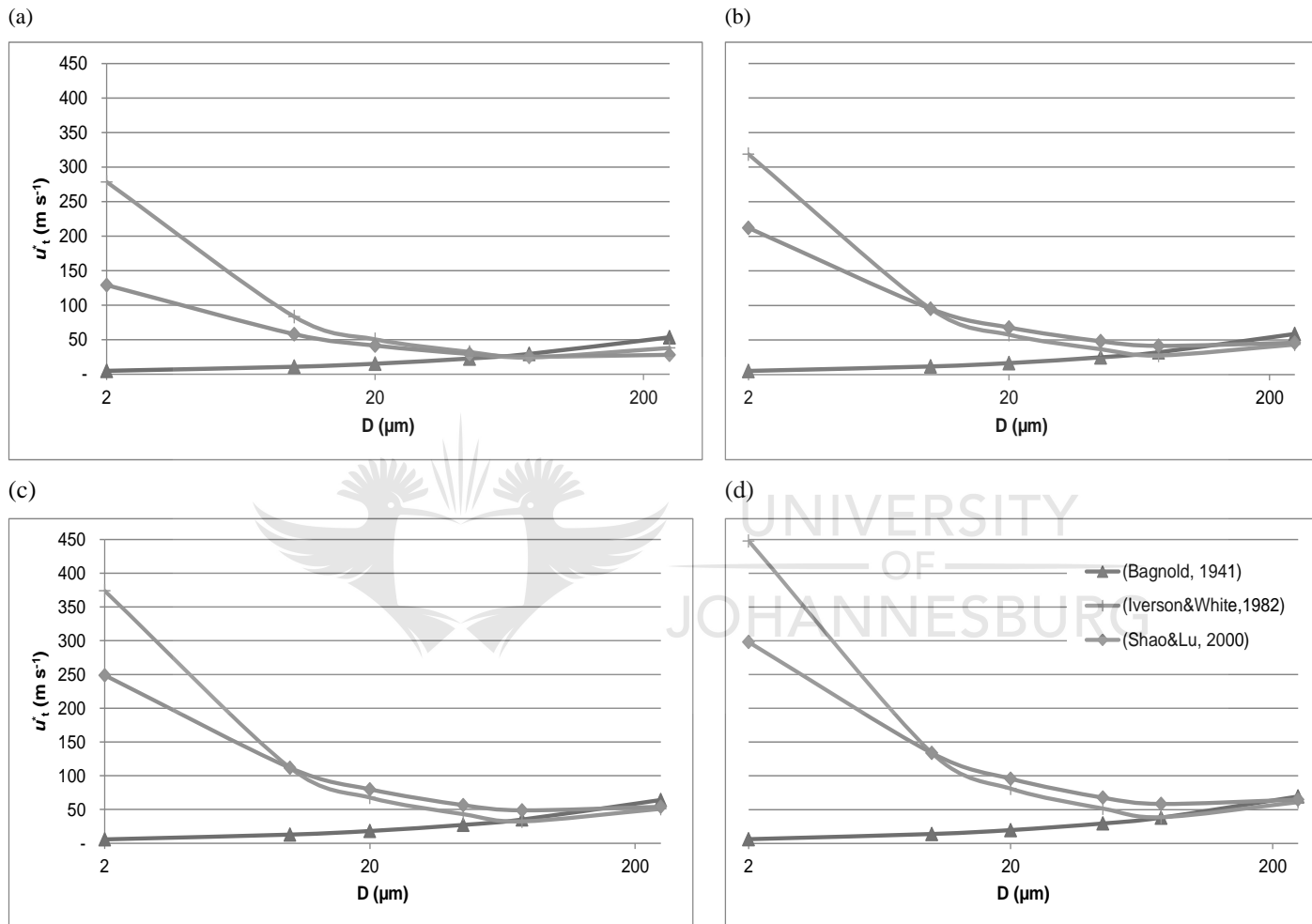
Figure 9: Relationship of threshold friction velocity (u*t) to the particle diameter (*d*) and total moisture content of (a) 1%; (b) 2%; (c) 4% and (d) 8%.
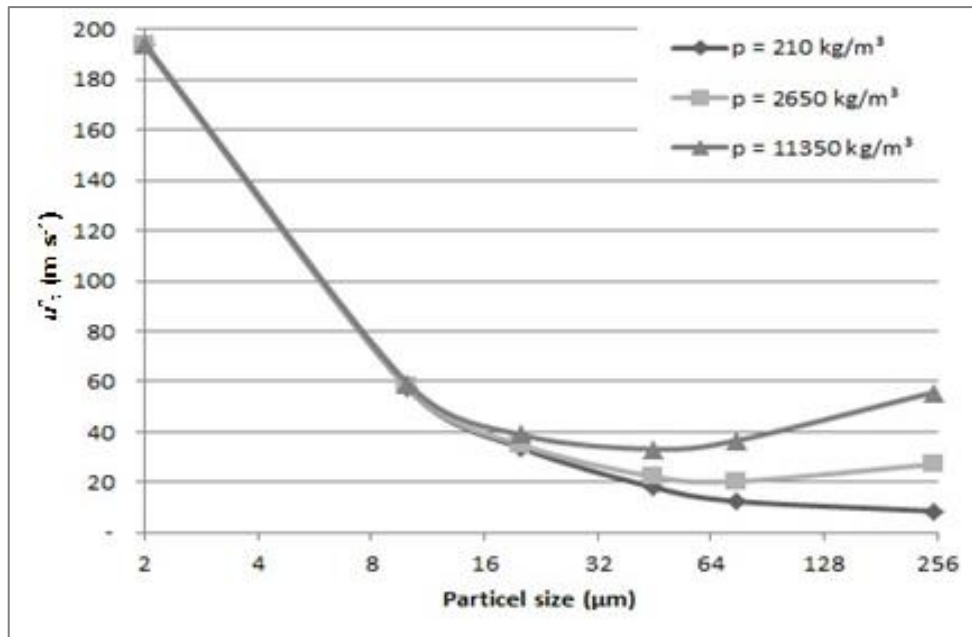
Figure 10: Relationship of threshold friction velocity (u*t) to the particle diameter (*d*) and particle density (P*p*) per the equations from Iversen & White (1982).

Surface soil crust

Physical crusts, formed when moisture evaporates from the soil, form faster and are stronger than biological crusts (Rice & McEwan, 2001). Gillette *et al.* (1980) tested the threshold friction velocities for wind erosion from natural desert soils. In his 1982 research, the focus was on the binding agents within the soil, looking at clay content, soil moisture, mineral content, organic material and salts. More specifically, the strength of soil crusts were tested, based on the modulus of rupture and the crust thickness (Gillette *et al.*, 1982). For desert soils, with a modulus of rupture (*M*) of less than 1 bar, the threshold friction velocity was shown to be less than 45 cm s^{-1}; conversely for $M > 2$ bars, the threshold velocity can be expressed by the regression formulae:

$$u_t^* = 42.9 + 12.1(M * thick^2) \tag{12}$$

for crust thickness < 1.9 cm and $(M * thick^2) \leq 20$ bar cm²

$$u_t^* = 324 + 705(M * thick^2)$$

for crust thickness < 1.9 cm and $(M * thick^2)$ 20 to 40 bar cm²

where: *thick* is the thickness of the crust

Gillette *et al.* (1982) found that even weak crusts effectively protect against soil erosion and that clay content may be the most influencing parameter in variable crust strength. Adding exchangeable sodium and combining calcium carbonate ($CaCO_3$) with the percentage clay proved

to be even more effective. Quantifying modulus of rupture (M) using the clay (η_c), salt and $CaCO_3$ content for two soil groups can be expressed as:

$$M = 0.122 \times (salt) + \begin{pmatrix} 0.45(for\ salt > 0.26) \\ 1(for\ salt < 0.26) \end{pmatrix} \tag{13}$$
$$\times \left\{ \left[\begin{pmatrix} 0.08(for\ non\ mica) \\ 0.0076(for\ mica) \end{pmatrix} + \begin{pmatrix} 0.033(for\ CaCO_3 > 1.7\%) \\ 0(for\ CaCO_3 < 1.7\%) \end{pmatrix} \right] \times \eta_c \right.$$
$$\left. + B \times ESP \right\}$$

where: *salt* is percentage of mass of water soluble matter

                  CaCO₃ is the percentage by mass of calcium carbonate

                  ESP is the exchangeable sodium content in milliequivalents per 100 grams (meq per 100 g)

                  B is a constant

                  mica has a clay mineralogy of ≥50% mica and ≤20% smectitie

Testing the sensitivity of Equation 11 to the clay, salt and $CaCO_3$ content indicated that mica soils are more dependent on salt content; however the clay percentage is the most important variable for non-mica soils. The relation between the soil clay, salt and $CaCO_2$ content was tested for the various soil sample data from Gillette *et al.* (1982), and showed a clear relation between increased clay content and increased crust strength and to a lesser extent, the percentage salt. The $CaCO_3$ content did not show a direct relation to increased crust strength. Limited data on *B* and *ESP* were reported but these seemed to have only a minor influence on the modules of rupture – ranging between an 18% (non-mica) and 23% (mica) difference – where E*SP* had been set to 100%.

Goossens (2004) looked at the relationship between the crust strength and the horizontal sand flux (Q) and vertical dust-flux (F). Both Q and F exponentially decay with an increase in crust strength. He found that the gradual bombardment of a soil crust by impacting particles does not have an immediate decaying effect on the crust but, once it perforates, the crust depletes quickly. He developed a relationship between crust strength (τ) and the horizontal (Q) and vertical (F) fluxes based on crust strength measurements and derived at the following ratio between un-crusted Q and F crusted horizontal saltation flux [K(Q)] and vertical dust-flux [K(*F*)]:

$$K(Q) = 5.2 \left(\frac{\tau}{10}\right)^6 - 55 \left(\frac{\tau}{10}\right)^5 + 201.6 \left(\frac{\tau}{10}\right)^4 - 300.6 \left(\frac{\tau}{10}\right)^3 + 255.2 \left(\frac{\tau}{10}\right)^2 - 15.8 \left(\frac{\tau}{10}\right) + 1$$

$$K(F) = -0.03 \left(\frac{\tau}{10}\right)^6 + 0.42 \left(\frac{\tau}{10}\right)^5 - 2.17 \left(\frac{\tau}{10}\right)^4 + 4.88 \left(\frac{\tau}{10}\right)^3 - 3.35 \left(\frac{\tau}{10}\right)^2 + 0.85 \left(\frac{\tau}{10}\right) + 1$$

(14)

with crust strength (τ) in kPa and measured with a torvane (Goossens, 2004).

By combining the methods of Gillette *et al.* (1982) and Goossens (2004), crust strength can be theoretically calculated based on the clay content alone. In addition, the crust thickness can be used to calculate u_t^* (Equation 7). The exponential decrease in both the horizontal (Q) and vertical (F) fluxes as the surface crust became stronger (Table 4). Equation 8 was used to calculate the modulus of rupture (M) and this is taken to be the same as the crust strength (τ).

Table 4:   The effects of surficial crust strengths on the horizontal saltation and vertical dust-flux.

	Clay (%)	M (bar)	M (kPa)	K(Q)	K(F)	K(Q)/K(F) ratio
Soil A	5.0	0.087	8.7	72.8	1.37	53
Soil B	10.0	0.125	12.5	137.1	2.23	61
Soil C	15.0	0.163	16.3	239.3	3.57	67

The physical measurement of soil crust strengths is not always possible and Fryrear (1996) and Fryrear *et al.* (1998) established soil crust factors based on the relationship between soil crust and the soil clay content. Under various abrasion conditions, crusts that form on silt loam and clay soils proved more effective in reducing overall wind erosion (Zobeck, 1991). Rajot *et al.* (2000) tested the influence of soil crusting on wind erosion for sandy soils and concluded that "sieving crusts" – i.e. crusts that formed as a result of in situ rearrangement of particles with no evidence of lateral movement due to runoff – do not protect soil from wind erosion and should not be taken into account.

Averaging time

Theoretical calculations of the threshold friction velocity (u_t^*) is typically based on hourly averages per the available meteorological data. Field measurements conducted by Stout (1998) allowed for the calculation of u_t^* for various averaging periods of 2, 5, 10, 20, 30 and 60 seconds. This indicated that, under typical field conditions with infrequent wind gusts, calculating u_t^* based on long averaging periods can result in considerable under-prediction of the wind erosion – around 20% (Burger, 2010).

3.3   Vertical Dust Flux Schemes

Shao (2008) stated that "…*dust-emission rate is the vertical mass flux of dust at the surface…*". The dust is comprised of the finer particles from the saltation layer (Marticorena & Bergametti, 1995). As demonstrated in Section 3.2.4, the threshold friction velocity increases with a decrease in particle size for d < 75 μm. However, once particles become airborne, the smaller particles tend to remain suspended in the atmosphere much longer and can be carried to higher altitudes, adding significantly to the atmospheric aerosol load. It is very difficult to measure dust concentrations in the air and, as an alternative, use is made of numeric dust-flux schemes to estimate dust emissions.

Previously, dust-flux was linked directly to the friction velocity representing the available energy – as presented by Gillette (1977) and Gillette and Passi (1988). Wind-tunnel experiments carried out by Loosmore and Hunt (2000) showed that the vertical flux because of saltation bombardment was significantly higher than from aerodynamic lift. The vertical flux is therefore generally derived from the horizontal flux (Marticorena & Bergametti, 1995). Table 5 provides a summary of the most widely applied dust emission schemes – as reported by Shao (2008) and including the simplified Shao 2004 scheme (Shao *et al*., 2011).

Figure 11 provides a comparison between the eight different vertical dust-flux models. The friction velocity ranged between 0.26 and 1.76 m s^{-1}, relating to wind velocities of between 1.5 and 10 m s^{-1} and with a threshold friction velocity of 0.20 m s^{-1}. Saltation flux rates (Q), as calculated with White's (1979) model, were applied. The input parameters selected for comparison (Table 6), are based on loamy soil characteristics. As reported by Lu (1999) loam soils tend to produce higher dust emissions than sandy soils because of the larger fraction of fine particles contained in the soil.

The model of Cowherd *et al.* (1988) resulted in the highest dust-flux rates (F) followed by the Gillette (1977), and Gillette & Passi (1983) models. In all three of these models, F depends only on u^*_t and is not a function of the horizontal saltation flux (as with the later models). The models of Shao (Shao *et al*., 1996; Shao, 2004; Shao *et al*., 2011), Marticorena & Bergametti (1995) and Lu & Shao (1999) resulted in much lower dust-flux rates when compared with Gillette & Passi (1983), ranging between a factor of 1 453 times to 150 065 times lower. The dust-flux rates (F) amongst these models are very similar with a maximum variation of 4.6 (between Shao *et al.*, 1996 and Shao *et al.*, 2011). The dust emission model developed by Lu & Shao (1999) can be manipulated through C_α to fit the other models and the Marticorena and Bergametti (1995) model is very sensitive to the clay content (assumed to be 5% for this comparison).

Table 5:   Summary of different dust-flux schemes.

Source	Expression	Where / for	
Gillette (1977)	$F = \alpha u_*^n$	α	(dimensional coefficient) = 1.24E-07
		n varies between 2.9 and 4.4	
Gillette & Passi (1983)	$F = \alpha u_*^4 \left(1 - \dfrac{u_t^*}{u^*}\right)$	α	(dimensional coefficient) = 2.5E-07
		for $u^* \geq u_t^*$	
Cowherd *et al.* (1988)	$F = 58(u^* - u_t^*)^2 + 25(u^* - u_t^*)$	for $u^* \geq u_t^*$ and $F = 0$ for $u^* \leq u_t^*$	
Marticorena & Bergametti (1995)	$F = Q \times 10^{0.134(\eta_c)-6}$	η_c (clay percentage) $\leq 20\%$	
Shao *et al.* (1996)	$F = \beta Q u_{*t,d}^{-2}$ $\beta = 10^{-5}[1.25\ln(d_s) + 3.28]exp(-140.7d_d + 0.37)$	d_s is sand particle size d_d is dust particle size	
Lu & Shao (1999)	$F = Q \times \dfrac{0.12 C_\alpha g f_i p_b}{\mathcal{P}}$	C_α is a dimensional coefficient P horizontal pressure (N m⁻²) or (Pa) f_i is the fraction of dust particles	
Shao (2004)	$F_i(d_s) = c_y f_i (1 - \gamma)(1 + \sigma_m)\dfrac{gQ}{u_*^2}$ $\sigma_m = 12u_*^2 \dfrac{p_b}{\rho}\left(1 + 14u^*\sqrt{\dfrac{p_b}{\rho}}\right)$	γ falls between 0 and 1 c_y is in the order of 0.1 f_i is the fraction of dust particles P horizontal pressure (N m⁻²) or (Pa)	
Shao *et al.* (2011)	$F(d_i) = c_y n_{mi}(1 + \sigma_m)\dfrac{gQ}{u_*^2}$	n_{mi} is the minimally disturbed dust particles	

Table 6:   Selected input parameters for the various dust-flux schemes.

Parameter	Value used	Source of value
η_c (clay percentage) $\leq 20\%$	5%	Generic value
d_s (sand particle size) (µm)	1 000	
d_d (dust particle size) (µm)	10	
C_α (dimensional coefficient)	0.015	Provides best fit in this study. (Kang, 2011) provides range of 0.001-0.0002
P horizontal pressure (N m⁻²)	10 000	(Shao, 2004; Kang, 2011) for loamy soils
f_i (fraction of dust particles)	5.13%	(Lu, 1999) fraction of $d < 20$ µm, same as $p_f(d)$
c_y	0.00003	(Kang, 2011) for loamy soils;
$p_f(d)$	5.13%	(Shao, 2004) Table 1
$p_m(d)$	70%	

The four dust-flux schemes, where F is derived from Q, will vary depending on the saltation flux model applied. For example, Marticorena and Bergametti (1995) based their dust-flux formulation on White's (1979) saltation model whereas Shao (2004) used Owen's (1964) saltation model. As discussed, Owen's model results in lower saltation flux rates (Q) of between 7 and 12 times to that of White (1979).
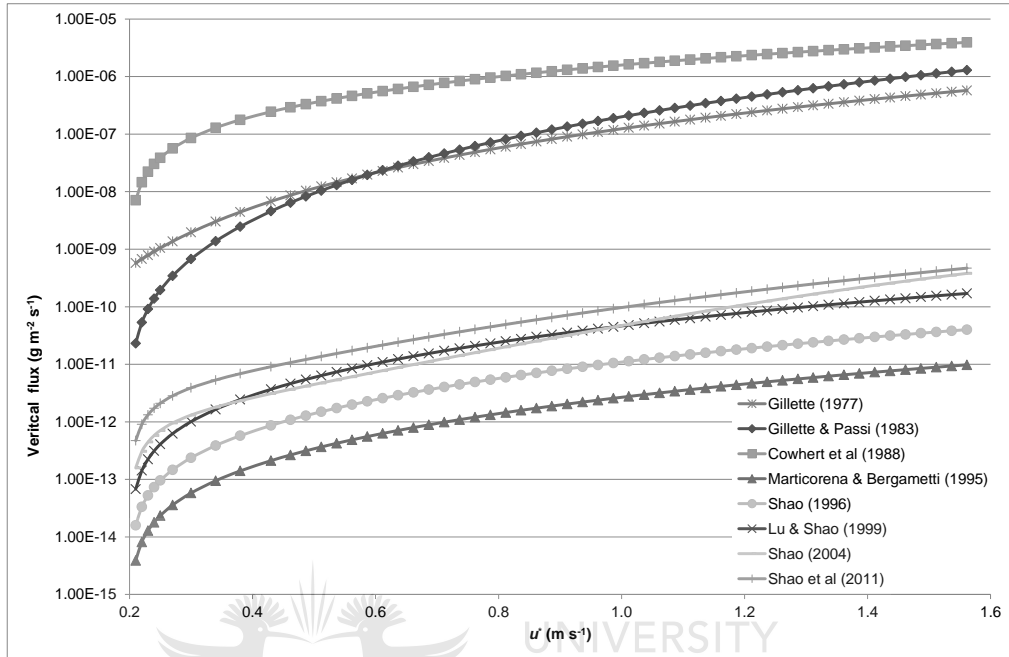
Figure 11:   **Comparison of the vertical dust-flux predictions.**

3.3.1   Integrated wind erosion schemes

The most widely applied dust-flux formulation seems to be the empirical approach of Marticorena and Bergametti (1995) and this has been used in a number of wind erosion schemes (Marticorena *et al.*, 1997; Alfaro & Gomes, 2001; Zender *et al.*, 2003; Goossens, 2004; Schmechtig *et al.*, 2011). A limitation of this approach is the over sensitivity to the soil clay content (η_c), – especially between 15% and 20%, – and therefore it can only be applied to soils with $\eta_c \leq 20\%$.

The various schemes developed by Shao (Shao *et al.*, 1996; Shao, 2004) and by Lu and Shao (1999) have been based on a theoretical treatment of the particle behaviours. The energy-based dust emissions scheme of Shao (1996) proposed that, for a given Q, F is proportional to the binding energy and initial kinetic energy of a dust particle and therefore related to the threshold friction velocity (u^*_t) of the dust particles (Shao, 2008). This approach results in a constant increase in F because of an increase in the dust particle size (d_d), keeping the sand particle size (d_s) constant. This is directly linked to a decrease in u^*_t. By keeping d_d constant while increasing d_s results in an insignificant increase in F.

A volume-removal-based dust emission scheme was developed by Lu and Shao (1999), considering the impacting particle velocity to be the main mechanism for removed volume of surface dust. This scheme uses soil plastic pressure or horizontal pressure (P) to estimate the dust-flux. Lu (1999) reported that, for hard surfaces with a large P, the dust rate is likely to be proportional to u^3_* and, for surfaces with a small P, F is proportional to u^4_*. Since F/Q is comparative to the dust fraction contained in the soil, there will be no F should the dust fraction (f_i) be zero (Shao, 2008). Limitations of this approach are that (i) the break-up of aggregates during saltation has not been taken into account; (ii) quantification of the removal volume may be too simplistic and (iii) the ratio between vertical and horizontal P and the contact area cannot be accurately described (Lu, 1999; Shao, 2008). This scheme proves most sensitive to P, where with an increase in the horizontal pressure (P), as would be expected, F decreases. The dust-flux scheme shows a set increase in F with an increase in the dust fraction (f_i), the bulk density and C_α. These findings have been confirmed by the sensitivity analysis conducted by Kang (2011). It should be noted that the P values reported by Lu (1999) were found to be too high (Shao, 2004) therefore values as reported by Shao (2004; 2008) and Kang (2011) were used in this evaluation. The scheme by Lu and Shao (1999) resulted in similar dust-flux rates as those of Marticorena and Bergametti (1995) and Shao (1996; 2004) when a value of 0.015 was used for C_α.

Following on his work with Lu (Lu & Shao, 1999), Shao (2004) developed a spectral dust-emission scheme accounting for dust emission rates for given particle size ranges accounting for the disaggregation into various particle sizes because of high velocity winds. As with the previous schemes, F is proportional to Q, but this ratio is determined by the soil texture and soil plastic pressure (Shao, 2008). The dust-flux is dependent on the dust fraction (f_i) in the soil, a combination of the free dust fraction (minimally disturbed particle size distribution) and the aggregated dust fraction (fully disturbed particle size distribution). It further depends on the soil plastic pressure (P) and saltation impact velocity determining the difference between the mass ejected by bombardment and the mass of the impacting particle (Shao, 2004). Lu (1999) distinguished between the minimally- and fully-disturbed particle size distribution (at ($p_m(d)$) and($p_f(d)$) respectively), based on the observations made by Alfaro *et al*. (1997). Whereas $p_m(d)$ can be determined though typical particle size analysis with no disturbance to the soil sample, the analysis of $p_f(d)$ requires the mechanical breakup of aggregates (Shao *et al*., 2011). A value γ falling between 0 and 1 accounts for the release of aggregated dust, where $\gamma = 0$ indicates aggregate dust release only during strong erosion events and $\gamma = 1$ represents free dust that can be released during weak erosion events. The sensitivity to the plastic pressure (P) and related coefficient c_y, has been reported by Kang (2011), with the sensitivity f_i similar to that of Lu and Shao (1999). The main difficulty with this dust emission scheme is the estimation of $p_f(d)$ and P, and fitting c_y relative to P in the absence of field data.

In 2011, Shao *et al.* (2011) published a simplified version of the 2004 equation not dependent on $p_f(d)$ and dismissed the calculation of the weighted average of the sand particle (d_1 and d_2). This provides a more practical approach, given the limitations in obtaining field data for $p_f(d)$. Comparison of the more basic scheme where γ is assumed to be equal to 1, seems to correlate well with the Shao (Shao, 2004) model, falling within a range of 0.31 and 0.75.

Fundamentally, these schemes are similar, with the main differences lying in the way the threshold friction velocity (u^*_t) is determined and the dust-flux (F) is computed (Shao, 2008).

3.4 Discussion

In this chapter, various wind erosion schemes were evaluated and the sensitivity of the input parameters tested to determine the most practical and appropriate scheme for application in commercial approaches.

All the horizontal saltation flux models depend on: the relative density of air (p_a); the gravimetric acceleration rate (g); and the friction velocity (u^*). The saltation flux models of Kawamura (1964), Owen (1964) and White (1979) are only indirectly sensitive to varying particle sizes because of its dependency on the threshold friction velocity (u^*_t). These models are not sensitive to u^*_t – except for particle sizes $d \leq 2\,\mu m$ – which shows a sensitivity towards lower friction velocities ($u^* < 3.1\,\mathrm{m\,s^{-1}}$). Saltation flux rates (Q), as calculated by the models of Bagnold (1941), Zingg (1953) and Lettau and Lettau (1978), increased with the increase in particle size (d) but did not account for u^*_t. All the saltation flux models evaluated showed sensitivity to the friction velocity (u^*) – with the model of Lettau and Lettau (1978) most sensitive to u^* and the models based on Kawamura (1964) and White (1979), the least sensitive.

The Iversen and White (1982) equation for quantifying u^*_t relies on the particle density (p_p), the relative density of air (p_a), the gravimetric acceleration rate (g) and the particle size (d). This model was found to be most sensitive to particle sizes where $d < 75\,\mu m$, resulting in an exponential increase in u^*_t for $d < 10\,\mu m$. This approach reflects the strong inter-particle cohesion forces amongst smaller particles and is widely accepted (based on the verification through wind tunnel experiments). Although the more simplified method of Lu and Shao (1999) provides a similar sensitivity to the smaller particle sizes, the dependency on γ (given to vary between 1.65×10^{-4} kg s^{-2} and 5×10^{-4} kg s^{-2}) can result in a difference in u^*_t for the smaller particle sizes of up to 1.7 times.

Although u^*_t is calculated independently from the friction velocity, u^* depends on the wind speed and the surface roughness length (z_0) with the latter depending again on u^*_t in certain equations. The threshold friction velocity is highly sensitive to the inclusion of roughness elements and it is important to ensure any drag partitioning scheme is selected where input parameters are

available because assumptions based on limited input parameters will significantly increase the uncertainty around the threshold friction velocity. The approach suggested by Marticorena and Bergametti (1995) requires fewer input parameters (that are more readily available) than the more complex approach by Raupach *et al.* (1993). The Owen effect results in extremely high threshold friction velocities, yielding no wind erosion. As a rule, the smooth roughness length (z_{0s}) can be determined through D/30 the height of the roughness elements (Callot *et al.*, 2000; Laurent *et al.*, 2006).

As expected, any binding agent (such as soil moisture and surface crust formation) would result in a decrease in saltation flux because of an increase in u^{*}_{t}, mostly affecting the particle sizes smaller than 10 μm. Both the approaches of Belly (1964) and McKenna Neuman and Nickling (1989), when accounting for the higher threshold friction velocity for wet soils, only apply to sandy soils and not to loam and clay soils. In addition, the difficulty of the McKenna Neuman and Nickling (1989) method to quantify accurately $|\Delta P|$ in natural soils limits this application. The simplified approach by Fécan *et al.* (1999), to account for the adsorbed moisture by the clay particles in specifically loam and clay soils, shows good agreement with experimental data.

The effect of soil crusting on the threshold friction velocity has been researched by Gillette *et al.,* (1982), Eldridge and Leys (2002) and Goossens (2004). Gillette related friction velocity to specific soil crust thickness and modulus of rupture, while Goossens investigated the physical crust strength relationship to the horizontal and vertical sediment fluxes. Even though both methods require physical measurement of soil crust strengths (which may not be practical), the combination of these two approaches results in a fairly simple method to determine the effect of surface crust strength on both the horizontal saltation flux (Q) and the vertical dust-flux (F).

In general the dust-flux schemes of Shao (1996), Marticorena and Bergametti (1995), Lu and Shao (1999) and Shao (2004) are in good agreement with each other. The Marticorena and Bergametti wind erosion scheme is based on an empirical approach whereas the ones from Shao and Lu and Shao are based on a theoretical treatment of the particle behaviours, using different input parameters. The appropriate selection of a horizontal dust-flux model is therefore not that obvious. The most practical dust-flux schemes based on the analysis regarded are those of Shao (2011), because of the simplification of the Shao (2004) wind erosion scheme, and that of Marticorena and Bergametti (1995). The application of the Marticorena and Bergametti (1995) should be restricted to soils with a clay content of less than 20%, whereas the simplified scheme from Shao *et al.* (2011) still requires specifying P, which is difficult to determine. For the purpose of this study, the methods proposed by Gillette *et al.* (1982) in quantifying modulus of rupture are used to determine plastic pressure (P). This will be investigated in the following section.

4 Quantification of Wind-Blown Dust from Mine Tailings and Ash Storage Facilities

Wind-blown dust from mine waste facilities can be a significant source of dust emissions, influencing the environment and affecting human health. Methods to quantify emissions and determine the impacts from mine tailings and ash storage facilities have not been widely investigated. Currently available wind erosion models have been developed primarily for application to agricultural lands or sand dunes. This section evaluates the applicability of the most widely used dust-flux schemes in the quantification of emissions from gold and platinum tailings; and ash storage facilities. Site specific particle size distribution data, bulk density and moisture content are used and considered to be representative of typical gold tailings, platinum tailings and coal ash storage facilities. The applicability of the dust-flux schemes are evaluated based on the availability of the various input parameters and the uncertainties within these parameters. The sensitivity of the emission rates to wind frequencies is also evaluated.

4.1 Project Scope

4.1.1 *Gold tailings storage facilities*

South African gold mines are located within the central parts of the country, with the largest gold reef deposit found in the Witwatersrand (Mining Intelligence Database, 2013). AngloGold Ashanti's Vaal River North operations, situated on the western extent of the Witwatersrand reef (26°56.107'S; 26°44.360'E), include six tailings storage facilities (TSFs) (Figure 12). The TSFs are scattered around the Stilfontein area, approximately 9 km southeast of the town of Klerksdorp, and vary in both age and size and are regarded as representative of typical gold tailings material. TSFs were developed at various stages during the operational life of the mines – through different deposition methods, and reflect the variations in composition and grain size distribution depending on both the geological strata of the mines and the prevailing milling technologies at the time.

4.1.2 *Platinum tailings storage facilities*

Impala Platinum Rustenburg is located approximately 14 km north-northwest of the town of Rustenburg in the North West Province of South Africa (Figure 13). Current mining operations include underground workings and opencast areas where the Merensky and UG2 reefs are mined. Impala has one dormant tailings dam, designated as No. 1 tailings dam (25°31.256'S; 27°11.910'E), and one active TSF, designated as No. 2 tailings dam (25°31.075'S; 27°13.940'E). These are located in close proximity to the settlement of Ga-Luka (Figure 13). Only No. 2 tailings dam (TSF

7) is of concern – with regard to the potential for wind-blown dust – because the No. 1 tailings dam is completely vegetated (Figure 14).

Figure 12: Locations of the six tailings storage facilities at AngloGold Ashanti Vaal River North operations Facilities (Image source: Google Earth 2014).
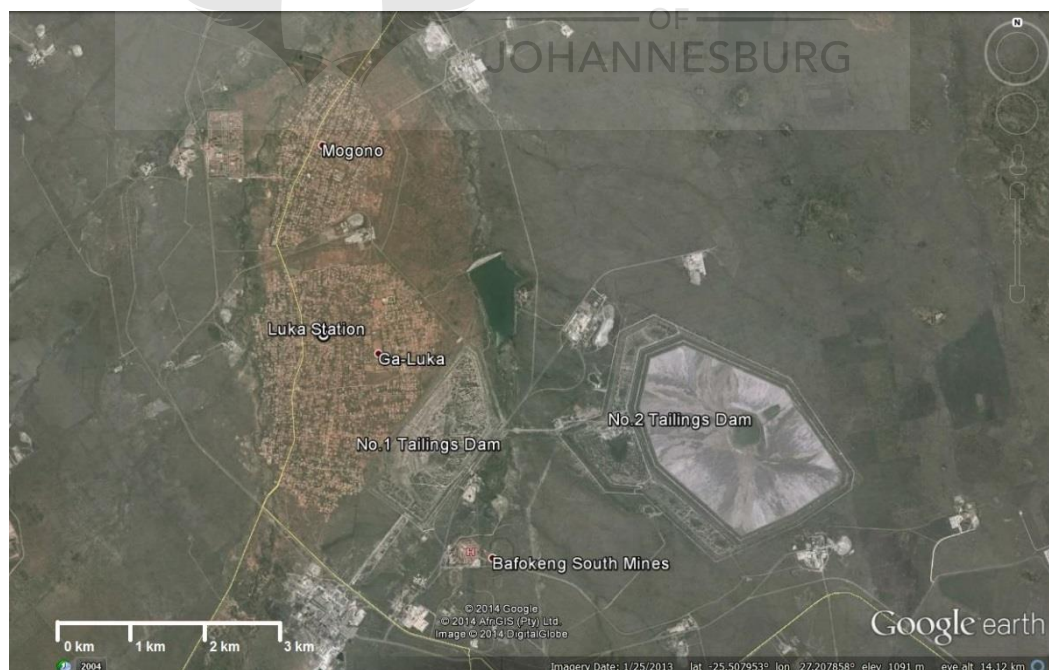
Figure 13: Locations of Impala Platinum Rustenburg Mine's Two Tailings Storage Facilities (Image source: Google Earth 2014).

**Figure 14:   Image of the rehabilitation status of No. 1 tailings dam
(Image courtesy of Impala Platinum Rustenburg).**

4.1.3   Coal-fired power station ash storage facilities

South Africa's coal-fired power plants are situated mainly in the north-eastern parts of the country, in the Mpumalanga Province, where most of the coal reserves are located. The Tutuka and Majuba Power Stations were selected as representative of Ash Storage Facilities (ASFs). The two power stations are approximately 54 km apart.

Tutuka Power Station is situated approximately 21 km north-northeast of the town of Standerton and 27 km to the west-southwest from Morgenzon at 26°46.644'S; 29°20.371'E. Tutuka's ASF is situated 3 km directly east of the power station (Figure 15).

The Majuba ASF is located at 27°6.952'S; 29°44.468'E, 1 km southwest of Majuba Power Station and 17 km northeast from the town of Amersfoort. Figure 16 shows the location of Majuba ASF in relation to the power station.

Both ASFs are the main dust generating sources in the immediate area, and are surrounded predominantly by agricultural land.

Figure 15: **Location of Tutuka Power Station ash storage facility (Image source: Google Earth 2013).**

Figure 16: **Location of Majuba Power Station ash storage facility (Image source: Google Earth 2013).**

4.2   Methodology

Emission rates for gold and platinum tailings, and ash storage facilities were quantified using the dust emission scheme of Marticorena and Bergametti (1995) referred to as MB95 (from this point forward) and Shao (2011) (referred to as SH11). The main components of these schemes are schematically represented in Figure 17 for MB95 and Figure 18 SH11. SH11 is the basic SH04 scheme discussed under Section 3.3. All input parameters in these schemes, that were not measured as part of this work, have been drawn from or calculated using referenced methodologies as discussed in Section 3.

4.2.1   *Tailings and ash sample analysis*

All the tailings and ash samples were obtained from previous studies conducted for the mines and power plants, with the sample locations not reported. Composite samples were taken at various locations on the TSFs and ASFs – surface, crest and side slope – to provide a representative sample of the overall particle size distribution. These samples were taken a few centimetres below the surface to represent erodible material but also to avoid material on the surface that have been deposited through transfer from other sources.

Particle size distribution (*psd*) for the tailings and ash samples were measured using laser diffraction (in the form of a Malvern Mastersizer® 2000 particle sizer-counter). The laser diffraction method determines the particle size through its light scattering properties where the light scattering angle and intensity is a logarithmic function of the particle size. The Malvern Mastersizer® 2000 can measure particle sizes ranging from 0 – 2 000 µm. Laser diffraction can be carried out on either wet (in liquid suspension) or dry samples. The dry process entails using air pressure for the break-up of aggregates through acceleration; the wet process sonication uses a fluid (such as water) to ensure the material is adequately dispersed for the separated individual particles to pass through the laser beam (USGS-NASA, 2007). The particle size distribution for the TSFs and ASFs were measured using the wet suspension method.

These *psd* results were used as input to the dust emission schemes of MB95 and SH11. The data analysis and results are described in more detail for each Case Study.

1   Input parameters

u^* (m s^{-1}): friction velocity

u^*_t (m s^{-1}): threshold friction velocity

η_c (%): clay content

θ (%): total soil moisture

w' (%): adsorbed soil moisture

z_0 (m): surface roughness length

z_{0s} (m): smooth roughness length

D_{ls} (m): mean distance between roughness elements

f: fraction of erodible area

psd (m): particle size distribution

p_b (kg m^{-3}): bulk soil density

p_a (kg m^{-3}): air density

g (m s^{-2}): acceleration due to gravity

$p(di)$: dust mass fraction of jth particle-size bin

---

2   Threshold friction velocity

2a *Threshold friction velocity over smooth surface*

$$u^*_t(d) = \frac{0.129 \times K}{(1.928 \times Re^{0.092}-1)^{0.5}} \qquad 03 < Re < 10$$

$$Re > 10$$

$$u^*_t(d) = 0.129 \times K[1 - 0.0858\, exp(-0.0617(Re - 10))]$$

$$where:\ K = \left(\frac{P_p g d}{P_a}\right)^{0.5} \times \left(1 + \frac{0.006}{P_p g d^{2.5}}\right)^{0.5}$$

$$Re = 1331\, d^{1.56} + 0.38 \qquad (eq.4)$$

2b *Drag partition correction (R)*

$$R(z_0, z_{0s}) = 1 - \frac{ln\left(\frac{z_0}{z_{0s}}\right)}{ln\left[0.35\left(\frac{D_{ls}/30}{z_{0s}}\right)^{0.8}\right]} \qquad (eq.6)$$

2c *Moisture correction (H)*

$$\frac{u^*_{tw}}{u^*_{td}} = 1 \qquad\qquad w < w'$$

$$\frac{u^*_{tw}}{u^*_{td}} = [1 + 1.21(w - w')^{0.68}]^{0.5} \qquad w > w'$$

$$w' = 0.0014(\eta_c)^2 + 0.17(\eta_c) \qquad (eq.11)$$

$$u^*_t(d; \lambda; w) = \frac{u^*_{ts}(d)}{R(z_0, z_{0s})}(w)$$

---

3   Horizontal Saltation Flux (WH79)

$$Q(d) = C_0 \frac{P_a}{g} u_*^3 \left(1 - \frac{u^*_t}{u^*}\right)\left(1 + \frac{u^*_t}{u^*}\right)^2 \qquad C_0 = 2.6$$

$$Q = \int_{d_0}^{d_n} Q(d)$$

(kg m^{-1} s^{-1})

4a **Crusting correction (K_h)**

$$F_{crusted} = \frac{F_{uncrusted}}{K_h}$$

$$K_h = -0.03\left(\frac{\tau}{10}\right)^6 + 0.42\left(\frac{\tau}{10}\right)^5 - 2.17\left(\frac{\tau}{10}\right)^4 +$$

$$4.88\left(\frac{\tau}{10}\right)^3 - 3.35\left(\frac{\tau}{10}\right)^2 + 0.85\left(\frac{\tau}{10}\right) + 1 \qquad (eq.14)$$

4b *Accounting for emissions per particle size group ($p(di)$)*

$$p_m(dj) = \frac{1}{d} \times \sum_{j=1}^{N} \frac{w_j}{\sqrt{2\pi}\sigma_j} exp\left[-\frac{(lnd - lnD)^2}{2\sigma_j^2}\right] \qquad (m^{-1})$$

$$(eq.15)$$

---

4   Vertical Dust Flux (MB95)

$$F(d) = 10^{(0.134\, x\, \eta c - 6)} \times Q \times p(dj) \times \frac{1}{K_h}$$

(kg m^{-2} s^{-1})

Figure 17:   Schematic diagram of parameterisation options and input parameters for the Marticorena and Bergametti (1995) dust-flux scheme – referred to as MB95.

1 Input parameters

u_t^* (m s^{-1}): threshold friction velocity

θ (%): total soil moisture

w' (%): adsorbed soil moisture

z_0 (m): surface roughness length

z_{0s} (m): smooth roughness length

p_b (kg m^{-3}): bulk soil density

pa (kg m^{-3}): air density

g (m s^{-2}): acceleration due to gravity

P (Pa): horizontal pressure

σ_p: particle-to-air density ratio

D_{ls} (m): mean distance between roughness elements

psd (m): particle size distribution

f_j : fraction of erodible dust of jth particle-size bin

$p(d_j)$: dust mass fraction of jth particle-size bin

η_{fj} (d): fully disturbed dust fraction of jth particle-size bin

η_{mj} (d): minimum disturbed dust fraction of jth particle-size bin

---

2 Threshold friction velocity

2a Threshold friction velocity over smooth surface

$$u_t^*(d) = \sqrt{B\left(\sigma_p g d + \frac{\gamma}{P_p d}\right)} \qquad B = 0.0123$$

$\gamma = 1.65 \times 10^{-4}$ kg s^{-2} and 5×10^{-4} kg s^{-2} (eq.5)

2a Drag partition correction (R)

$$R(z_0, z_{0s}) = 1 - \frac{ln\left(\frac{z_0}{z_{0s}}\right)}{ln\left[0.35\left(\frac{D_{ls}/30}{z_{0s}}\right)^{0.8}\right]} \qquad (eq.6)$$

2c Moisture correction (H)

$\frac{u_{tw}^*}{u_{td}^*} = 1 \qquad\qquad w < w'$

$\frac{u_{tw}^*}{u_{td}^*} = [1 + 1.21(w - w')^{0.68}]^{0.5} \qquad w > w'$

$w' = 0.0014(\eta_c)^2 + 0.17(\eta_c)$ (eq.11)

$$u_t^*(d; \lambda; w) = \frac{u_{ts}^*(d)}{R(z_0, z_{0s})}H$$

---

3 Horizontal Saltation Flux (WH79)

$$Q(d) = C_0 \frac{P_a}{g} u_*^3 \left(1 - \frac{u_t^*}{u^*}\right)\left(1 + \frac{u_t^*}{u^*}\right)^2 \quad C_o = 2.6$$

$$Q = \int_{d_0}^{d_n} Q(d)$$

(kg m^{-1} s^{-1})

4a Minimally and fully disturbed psd fraction

$$p_m(d_j) = \frac{1}{d} \times \sum_{j=1}^{N} \frac{w_j}{\sqrt{2\pi}\sigma_j} exp\left[-\frac{(lnd - lnD)^2}{2\sigma_j^2}\right]$$

$$\eta_{fj} = \int_{d_0}^{d_n} p_f(d_j)\,\delta(d_j)$$

$$\eta_{mj} = \int_{d_0}^{d_n} p_m(d_j)\,\delta(d_j) \qquad (eq.15)$$

4(i) Vertical Dust Flux (SH04)

$$F_i(d_s) = c_y f_i (1 - \gamma)(1 + \sigma_m)\frac{g}{u_*^2} \times Q$$

$$\sigma_m = 12u_*^2 \frac{p_b}{P}\left(1 + 14u^*\sqrt{\frac{p_b}{P}}\right) \quad \gamma = 0 \text{ or } 1$$

(kg m^{-2} s^{-1})

4(ii) Vertical Dust Flux (SH11) *(simplified version of SH04)*

$$F(d_j) = c_y n_{mi}(1 + \sigma_m)\frac{g}{u_*^2} \times Q$$

(kg m^{-2} s^{-1})

Figure 18: Schematic diagram of parameterisation options and input parameters for the Shao *et al.* (2011) dust-flux scheme – referred to as SH11.

4.2.2   Quantification of dust-flux scheme input parameters

The simplified Shao (2004) equation (Shao *et al*., 2011) only references the *minimally dispersed particle fraction $p_m(d)$* per option 4(ii) in Figure 18. The $p_m(d)$ is defined as the limited amount of dust that can be released from a unit soil mass under weak erosion potential in which no aggregation break-up occurs. The Shao (2004) equation in option 4(i) of Figure 18, and discussed in Section 3.3, accounts for both the $p_m(d_j)$ and the *fully dispersed particle fraction $p_f(d_j)$* for the jth bin of the particle size distribution (*psd*). The latter refers to the break-up of aggregates through mechanical processes (Shao, 2008; Shao *et al*., 2011). Both $p_m(d)$ and $p_f(d)$ are linked to the soil particle-size distribution and can only be approximated. Equation 14 was used to estimate the $p_m(d)$ for each gold and platinum tailings storage facility (TSF) and ash storage facility (ASF).

$$d \times p(d) = \sum_{j=1}^{N} \frac{w_j}{\sqrt{2\pi}\sigma_j} exp \left[- \frac{(lnd - lnD)^2}{2\sigma_j^2} \right] \tag{15}$$

where w_j is the weight of the jth mode of the particle size distribution and D_j and σ_j are centroid diameter and width for the lognormal distribution of the jth mode.

A chi-square least squares fitting technique was used to determine the parameters of w_j, D_j and σ_j for a multi-mode lognormal mathematical model to the measured size distributions. The particle size distribution of the various material types determines the number of modes, but field studies have shown that three or four modes ensure a good fit with data (Shao, 2008). Strictly speaking, the Malvern Mastersizer® 2000 technique (as used in all the particle size distribution analyses) will cause the break-up of aggregates, resulting in a fraction closer to the fully dispersed $p_f(d)$ than the minimally dispersed $p_m(d)$. For the purpose of this study, the particle size distribution from the Malvern Mastersizer® 2000 technique was taken to be representative of the $p_m(d)$ per the methodology used in Shao *et al.* (2011).

An example of the calculated minimally dispersed $p_m(d)$ is provided for one of the TSFs to demonstrate the methodology. Distributions for the other TSFs and ASFs samples are presented in Appendix B. As an initial selection, three modes were chosen. For each jth mode a characteristic particle diameter Dj, represented as the particle radius R_j, was selected with its associated concentration N_j – in this case the *psd* fraction – and an estimated standard deviation σ_j. The "solver" function in Excel was used to determine the best fit for the variance. In the example provided in Figure 19 for TSF1, the three modes are clearly visible within the overall logarithmic display of the *psd*. Mode 1 has a D_1 of 11.5, a concentration (N_1) of 8.90 and a standard deviation (σ_1) of 4.06. The large standard deviation of Mode 1 covered the entire array, overlapping with Modes 2 and 3, but provided the best fit with the *psd* distribution. The coefficients for Mode 2 and Mode 3 are displayed in Figure 19.

The parameters used to quantify $p_m(d)$ are the lognormal distribution for each of the three modes (Table 7). Four particle size bins were applied – PM$_{2.5}$, PM$_{10}$, PM$_{75}$ and PM$_{477}$ – as representative of the respirable dust fraction; the thoracic dust fraction; the total suspended dust fraction; and the upper limit of the *psd* (for the purpose of air quality impact assessment studies), respectively. The resulting $p_m(d)$ is the sum of each bin.
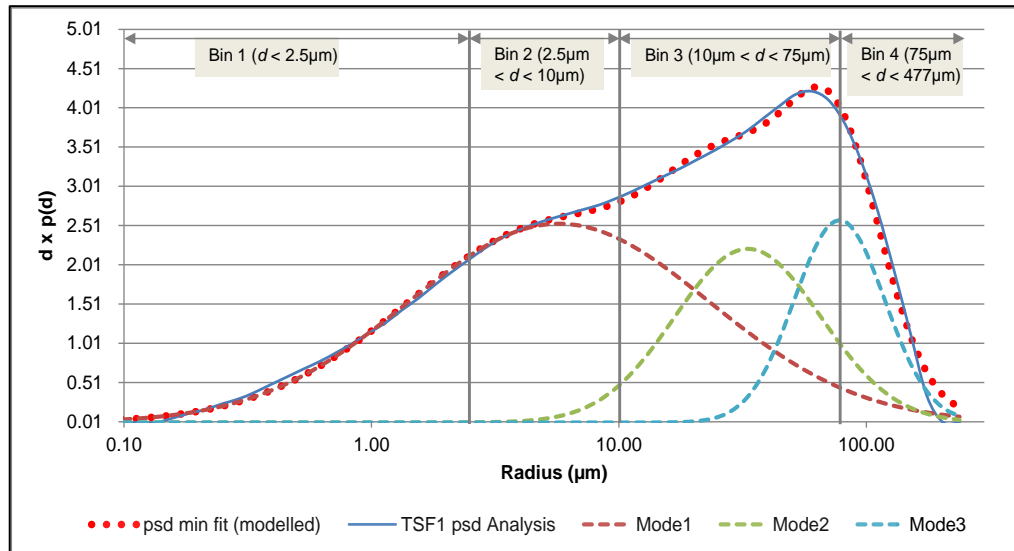
Figure 19: **Least squares fit of a three-mode model applied to the measured particle size distribution of sample of tailings material from the AngloGold Ashanti West Extension (TSF1).**

Table 7: **Minimally dispersed particle fraction $p_m(d)$ for the four particle size bins of PM$_{2.5}$, PM$_{10}$, PM$_{75}$ and PM$_{477}$ for the three selected modes.**

Modes	Dj (µm)	σ (µm)	w	Percentage of $p_m(d)$ fractions			
				Bin 1	Bin 2	Bin 3	Bin 4
				(d < 2.5 µm)	(2.5 µm < d < 10 µm)	(10 µm < d < 75 µm)	(75 µm < d < 477 µm)
Mode 1	11.5	4.1	0.58	7.8	21.0	24.7	4.4
Mode 2	66.4	1.98	0.25	0.0	0.1	15.3	9.3
Mode 3	156	1.52	0.18	0.0	0.0	1.1	16.6
	Total $p_m(d)$ (%)			7.8	21.0	41.0	30.2

In addition to quantifying $p_m(d)$, the resistance of the soil to wind erosion needed to be established through the parameterisation of plastic/ horizontal pressure (*P*) which was assumed to be equal to the modulus of rupture (*M*) (as defined by Gillette *et al.* (1982)). *P*, as indicated before, is difficult to estimate and even field and laboratory measurements seem to provide varying results – ranging between 3 000 Pa (Gillette *et al.*, 1982) and 107 Pa (Rice *et al.*, 1997). The field data collected by Goossens (2004) ranged between 12 000 Pa and 37 000 Pa.

P can be quantified using material mineralogy through the application of Equation 13. This equation requires the clay content of the material, the calcium carbonate- ($CaCO_3$) and salt- ($NaCl$) content, the cation exchange capacity (CEC) and exchangeable sodium percentage (ESP). The latter two parameters not readily measured. Even for the $CaCO_3$ and $NaCl$, analysis is typically limited to calcium (Ca) and sodium (Na) only.

The tailings mineralogy mirrors that of the parent rock from which the gold and platinum are extracted; conversely the coal ash undergoes considerable morphological changes through being exposed to high temperature (1 300°C) in pulverised fuel injection furnaces. All the TSFs and ASFs materials were taken to be non-mica in nature and Equation 13 for non-mica soils was applied, relying primarily on the clay (taken in this context purely as a size descriptor) content. It should be noted that Equation 13 defines clay as $d < 4$ µm (Gillette *et al*., 1982) and not $d < 2$ µm per the typical soil classification provided by Friedman & Sanders (1978). For the tailings and ash samples, the mineral composition was only available for the calcium (Ca) and sodium (Na) content, and these parameters were used as surrogates for $CaCO_3$ and $NaCl$, respectively, in the quantification of P (Table 8). The effect of exchangeable sodium (ESP) in clays was ignored by setting B and ESP to 0 because the clays in mechanically crushed ores do not have the same electro-static functions as clays in natural soils.

Another approach would be to interpolate the provided range of P, assuming P to be 5 000 Pa for sandy soils, 17 500 Pa for silt soils and 30 000 Pa for clay soils (Shao, 2008; Kang, 2011). The interpolation uses the relationship between the percentage sand, silt and clay (in this case $d < 2$ µm) applied to the allocated P values for each category.

$$A = \frac{(x_1 y_1 - x_2 y_2)}{(x_1 y_3 - x_3 y_1)}$$

$$c = \frac{A(v_3 x_1 - v_1 x_3) - (v_2 x_1 - v_1 x_2)}{A(z_3 x_1 - z_1 x_3) - (z_2 x_1 - z_1 x_2)}$$

$$b = \frac{(v_2 x_1 - v_1 x_2) + c(z_1 x_2 - z_2 x_1)}{(x_1 y_2 - x_2 y_1)}$$

$$a = \frac{v_1 - (b y_1 + c z_1)}{x_1} \tag{16}$$

where:

	x	y	z	P (Pa)	Cy
Clay	0.001	0.001	0.998	5 000	0.0001
Silt	0.001	0.998	0.001	17 500	0.00003
Sand	0.998	0.001	0.001	30 000	0.00001

The quantified values for P are provided in Table 8, based on Equation 13, and the interpolated values based on Equation 16. There is a difference in the quantified and interpolated values between 1.53 (platinum tailings) and 7.7 (ash). On average, the difference is 2.4 for the gold tailings and 5.1 for the ash storage. For the purpose of this study, P based on interpolation, was used because of the large uncertainty surrounding the quantified values.

Table 8: Mineral composition of calcium carbonate, sodium and potassium from the gold tailings-, platinum tailings- and ash storage facilities.

	Source	Source Code	Clay (<4 μm)	CaCO$_3$	Na	P (non-mica)	P (mica)	P (inter-polated)
			(%)	(%)	(%)	(Pa)	(Pa)	(Pa)
Gold Tailings Facilities	West Extension	TSF1	12.8	0.58	0.26	15 620	15 202	14 130
	West Complex	TSF2	13.7	0.55	0.22	13 414	12 369	14 717
	South East	TSF3	18.1	0.54	0.59	17 004	15 617	16 652
	East Complex	TSF4	11.9	0.54	0.59	7 508	15 596	13 247
	South Complex	TSF5	18.1	0.54	0.59	8 006	15 617	16 652
	Sulphur Dam	TSF6	6.8	0.47	0.08	6 238	8 889	10 073
	Average	-	13.6	0.54	0.39	11 298	13 882	14 245
	Standard deviation	σ	2.7	0.02	0.17	4 213	2 514	2 245
Platinum	Impala Tailings No. 2	TSF7	2.90	2.78	0.62	8 834	8 607	12 106
	Standard deviation	σ	1.40	0.13	0.03	417	462	-
Ash Facilities	Tutuka	ASH1	6.4	3.12	0.40	1.28E+04	5 215.51	1.28E+04
	Majuba	ASH2	2.7	0.43	0.14	1.45E+04	1 883.36	1.45E+04
	Average	-	4.6	1.77	0.27	3.55E+03	3.35E+03	1.37E+04
	Standard deviation	σ	1.9	1.35	0.13	1 666.07	1 658.34	835.63

The particle size dependent coefficient c_y was also estimated through interpolation per Equation 16. The range applied by Shao (2008) fell between 1×10^{-5} for clay soils, 3×10^{-5} for silt soils and 5×10^{-5} for sandy soils.

4.2.3   Meteorological data

The sensitivity of the dust-flux schemes to wind frequency was also tested. Regulatory dispersion models require hourly averaged meteorological parameters as input to the model. Consequently, wind dependent emissions rates were limited to hourly averages as the minimum time interval and did not account for the highly variant wind speeds associated with South African Highveld weather conditions (Section 2.4.3). Wind speeds and directions can change drastically within a few minutes, resulting in highly variable wind speeds within an hour. To correct for the 2-

3 second gusts in hourly mean wind speeds in the interior of South Africa a gust correction factor of 2.0 is proposed (Goliger *et al*., 2009).

Two separate meteorological datasets with variable wind speeds were used for the analysis: one reflects 10-minute averages and the other 5-minute averages. The 10-minute dataset for a period of one year (2010) was obtained from the Impala Platinum Luka ambient monitoring station (25°30.410'S; 27°11.031'E), located within the Ga-Luka settlement as shown in Figure 13. The 5-minute dataset, also for a period of one year (2012), was obtained from the South African Weather Services weather station in Klerksdorp (26°54.048'S; 26°37.050'E). This station is located to the north-west of the AngloGold Ashanti TSFs (Figure 12).

Emissions were quantified in two ways:

- calculating emissions for sub-hour intervals before averaging these to hourly emission rates;

- calculating hourly emission rates based on hourly averaged wind speed data.

4.2.4 Methodology Assumptions

The assumptions applicable to the TSF and ASF emission quantification methodology can be summarised as follow:

- All *psd* data in this study were derived from the Malvern Mastersizer® 2000 analyses methodology and taken to represent the *minimally dispersed fraction* $p_m(d)$. In this study, $p_m(d)$ is referred to as the *free dust fraction*;

- *P*, was determined through interpolation by applying Equation 16 and assuming the range for sand, silt and clay from natural soils was applicable to tailings and ash material;

- c_y for each source was estimated through the interpolation of referenced c_y for clay, silt and sandy soils based on the percentage sand, silt and clay (Equation 16);

- The threshold friction velocity is very sensitive to the surface vegetation and roughness elements. The correction from drag partitioning (*R*) was accounted for in both dust-flux schemes (Figures 17 and 18) through the MB approach, with the local roughness length (z_{0s}) and the roughness length (z_0) the only input parameters required. The input parameters for the Raupach *et al.* (1993) approach were more difficult to attain (i.e. ratio of the drag coefficient for a single roughness element, roughness density of the non-erodable elements) resulting in larger uncertainties around the final u^*_t. The limitation of the MB95 approach is that it only applies to solid obstacles and to small wakes ($z_0 < 1$ cm). The roughness over smooth surfaces z_{0s} was calculated as $D/30$ of the mass median diameter of the coarse mode of undisturbed particles, taken in this study to be $d > 60$ μm;

- The effect of moisture (H) on u^*_t was accounted for through the Fécan parameterisation (Equation 11) in both the MB95 (Figure 17) and SH11 (Figure 18) schemes. Darmenova *et al.* (2009) reported that the Shao moisture parameterisation (Shao *et al*., 1996) provides an unrealistically large threshold friction velocity for moisture content above 0.05 cm³/cm³ – resulting in no dust emissions – and the Fécan parameterisation is more justified;

- Saltation flux was determined with White's (1979) equation, using a generic wind field for demonstration purposes, ranging between 5.3 and 39.5 m s^{-1} for PM$_{75}$ and 14.4 to 63.0 m s^{-1} for PM$_{10}$;

- The correction for the effect of crusting was only applied to the MB95 dust-flux schemes through Equation 14 (Goossens, 2004). The crust strength (τ) was measured in Pa and the horizontal pressure (P) (as used in the SH11 dust-flux scheme) was used to estimate the correction factor for crusting. The effect from crusting was accounted for through the horizontal pressure (P) parameter in the SH11 dust-flux scheme and therefore the correction for crusting was not applicable to SH11;

- The soil classification, i.e. clay, silt and loam, was based on the Friedman and Sanders (1978) classes (Table 2) where the clay fraction was $d < 2$ µm;

- The MB95 dust-flux scheme was treated to reflect the particle size groups through the application of Equation 15;

- The simplified SH04 scheme, referred to as the SH11 dust-flux scheme, was used in this study.

4.3 Gold Tailings Storage Facility Case Study

4.3.1 Data collection and analysis

Composite samples were taken at each of the tailings complexes and analysed for particle size distribution (*psd*) using the Malvern Particle Size Analyser. Particle sizes less than 477 µm were reported. The *psd* for selected particle sizes are listed in Table 9 with the input data provided in Appendix A.

The younger TSFs (South Complex; South East and West Complex) are comprised of larger fractions of fine material than the older TSFs (Sulphur Paydam; East Complex and West Extension) which contain more material in the coarse fractions. This is understood to be a result of changes in the mine processing methods over the years, with newer technology resulting in finer milling fractions. The lognormal size distribution (Figure 20) shows two modes at 9 µm and 48 µm for the South Complex and the South East respectively. The East Complex and West Complex reflected a similar, but slightly coarser particle distribution, with the modes at 9 µm and 104 µm

respectively. Sample tailings material from the West Extension had a mode size of 120 μm; the Sulphur Paydam size was 164 μm. The Sulphur Paydam samples had a very small percentage of material in the fine fraction (15% < 10 μm).

Using the nonlinear least-squares fitting techniques to determine the modes, three modes provided the best fit for all the TSFs. Graphical representations for the six TSFs are provided in Appendix B, with the fractions for $PM_{2.5}$, PM_{10}, PM_{75} and PM_{477} provided in Table 9. Table 11 lists all the parameters used in the dust emission scheme calculations.

The clay fraction in the gold tailings showed a small variation between the six TSFs – as indicated by the standard deviation (σ) of 1.9 μm in Table 10. A much larger variation was noted for the coarser fractions – with σ = 14 μm for silt and σ = 16 μm for sand.

By using Equation 12 to estimate horizontal pressure, P fell within a range of 10 073 Pa and 16 652 Pa with low variability (σ = 2 245) (Table 11). The range for P was within the silt and silty clay soil range. The use of Equation 13 for non-mica soils resulted in similar horizontal pressure (P) for TSF1, TSF2 and TSF3; the other three TSFs had slightly lower values for P. The interpolated values for P was used because of the uncertainties linked to the input parameters for Equation 16 (viz. sum of the sodium and potassium content was taken to be representative of the total soluble salts and the calcium content was assumed equal to the $CaCO_3$ content). Interpolated values for c_y, using Equation 16, ranged between 4×10^{-5} and 7×10^{-5}.
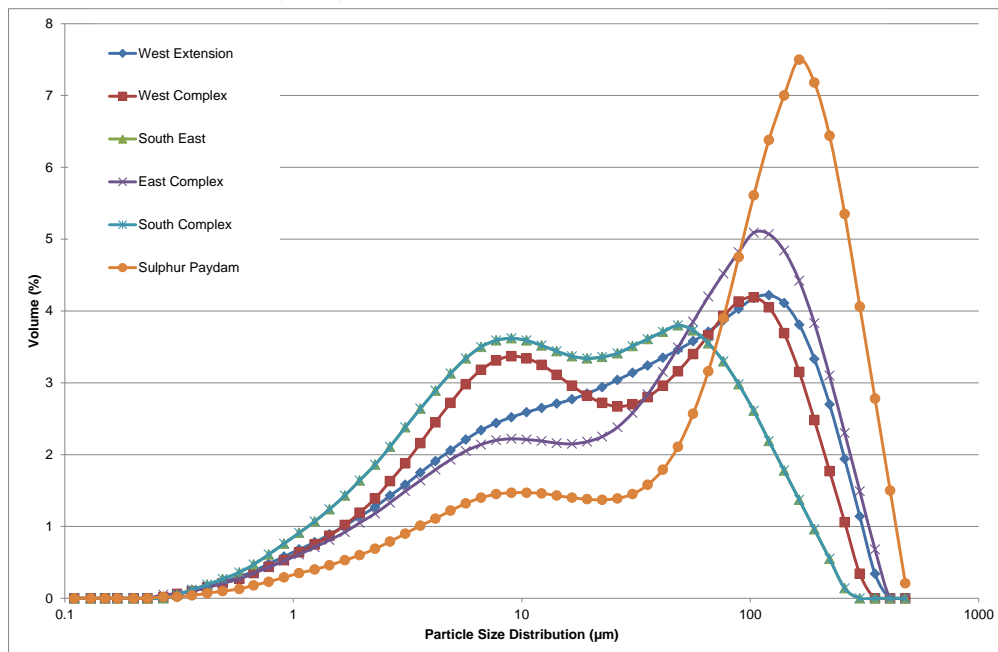
Figure 20:   Particle size distribution for the West Extension, West Complex, South East, East Complex, South Complex and Sulphur Paydam TSFs at the Vaal River North operations.

Table 9: **Minimally dispersed particle fraction $p_m(d)$ for the three particle size bins of PM$_{2.5}$, PM$_{10}$ and PM$_{75}$ for the six TSFs.**

Modes	Percentage of $p_m(d)$ fractions		
	PM$_{2.5}$ $(d < 2.5\ \mu m)$	PM$_{10}$ $(d < 10\ \mu m)$	PM$_{75}$ $(d < 75\ \mu m)$
TSF 1	0.08	0.29	0.70
TSF 2	0.08	0.34	0.74
TSF 3	0.11	0.41	0.87
TSF 4	0.07	0.26	0.64
TSF 5	0.11	0.41	0.87
TSF 6	0.04	0.16	0.41

4.3.2   *Emission quantification and results*

The effect of moisture and drag partitioning on u^*_t was accounted for in the horizontal dust-flux, resulting in an increase in the threshold friction velocity (u^*_t) from 0.20 m s^{-1} (no moisture or roughness elements were accounted for) to 0.31 m s^{-1} for MB95 (Figure 17) and 0.36 m s^{-1} for SH11 (Figure 18). The roughness length (z_0) was taken to be 0.003 m as representative of *bare sand* – according to the roughness lengths for different surface configurations reported by Burger (Burger, 1986). The median D was taken to fall between 60 μm $< d <$ 477 μm. An average moisture content of 0.20% was used – samples were obtained from various areas on two of the gold TSFs: West Extension and the East Extension. The surface areas sampled included the inner beach, the outer beach, the crest, the slope and the toe of the TSFs.

The PM$_{75}$ vertical dust-flux rates (g cm^{-2} s^{-1}) for MB95 and SH11 are shown in Figure 21 for the six TSFs. In general, a good correlation was found between the two models, with SH11 resulting in emission rates, on average, of between 1.5 and 7 times higher emission rates than those from the MB95 model. This excluded the Sulphur Paydam, which provided the worst correlation between the two models, with SH11 on average displaying emissions 31 times higher than MB95. This could be because of the composition of the Sulphur Paydam is comprised of a larger fraction of coarse particles and has a η_{mi} fraction equal to 0.42. The other five TSFs displayed a η_{mi} fraction between 0.64 and 0.87.

Table 10: Lognormal particles size distribution for the six gold TSFs for minimally dispersed particle size distribution.

Source	Source Code	Clay (<2 µm)	Silt	Sand	Mode 1			Mode 2			Mode 3		
					w_1	$(D)_1$	σ_1	w_2	$(D)_2$	σ_2	w_3	$(D)_3$	σ_3
		(%)	(%)	(%)		(µm)	(µm)		(µm)	(µm)		(µm)	(µm)
West Extension	TSF1	6.8	59.5	33.7	0.58	11.5	1.40	0.25	66.4	0.68	0.18	156.0	0.42
West Complex	TSF2	6.6	64.6	28.8	0.66	10.7	1.23	0.00	20.0	0.84	0.34	104.2	0.57
South East	TSF3	9.1	75.0	15.9	0.60	7.5	1.22	0.12	20.0	0.96	0.28	68.0	0.64
East Complex	TSF4	6.2	53.6	40.2	0.49	10.0	1.36	0.33	79.4	0.61	0.18	164.7	0.43
South Complex	TSF5	9.1	75.0	15.9	0.60	7.5	1.22	0.12	20.0	0.96	0.28	68.0	0.64
Sulphur Dam	TSF6	3.4	33.9	62.7	0.33	11.8	1.37	0.28	100.0	0.51	0.39	198.1	0.43
Mean		6.9	60.3	32.8									
Standard deviation (σ)		1.9	14.1	16.0									

Table 11: Selected input parameters from the gold TSFs for the various dust emission schemes.

Source	Source Code	% Clay (<4 μm)[a]	% Salt[b]	% CaCO$_3$[c]	% Moisture content[d]	Particle density (kg m^{-3})[e]	*P* interpolated (Pa)	*P* calculated non-mica (Pa)	K(Q) crusting ratio[f]	K(F) crusting ratio[f]	*Cy*
West Extension	TSF1	6.8	1.24	0.58	0.2	2 625	14 130	15 620	183.4	2.76	5.22E-05
West Complex	TSF2	6.6	1.01	0.55	0.2	2 625	14 717	13 414	180.1	2.97	4.88E-05
South East	TSF3	9.1	1.28	0.54	0.2	2 625	16 652	17 003	248.5	3.71	3.93E-05
East Complex	TSF4	6.2	1.28	0.54	0.2	2 625	13 247	7 507	84.8	2.46	5.69E-05
South Complex	TSF5	9.1	1.28	0.54	0.2	2 625	16 652	8 006	173.3	3.71	3.93E-05
Sulphur Dam	TSF6	3.4	0.73	0.47	0.2	2 625	10 073	6 238	48.2	1.61	7.33E-05
Average		6.9	1.13	0.54	0.2	2 625	14 245	11 298	153.1	2.87	5.16E-05
Standard deviation (σ)		1.9	0.21	0.03		-	2 245	4 213	66.9	0.73	1.16E-05

[a] Definition for clay content as used in Equation 8 (Gillette *et al.*, 1982).

[b] Sum of sodium and potassium content.

[c] Based on calcium content.

[d] Moisture content as an average between the inner and outer beach areas, the crest and the slope from West Extension.

[e] Average air dried moisture content because of evaporation from the inner beach; the outer beach; the crest; the slope and the toe at the West Extension and East Extension TSFs (Agreenco, 2010). West Complex was assumed to have the same moisture content as West Extension with all the rest linked with the East Extension because of similarity in locality.

[f] Based on the interpolated horizontal pressure (*P*).

For the three TSFs: West Extension; West Complex and South East, the correlation between the two schemes improved with an increase in wind speed; for the other three (East Complex; South Complex and Sulphur Paydam) a contrasting trend was shown where the correlation between the two schemes declined at higher wind speeds and improved at lower wind speeds (Figure 21).

The effect of crusting on the MB95 scheme, through the application of F_{MB95}/K_F, is shown in Figure 22. The emissions decreased by 69%, resulting in a poor correlation between the two dust-flux schemes. The SH11 dust-flux emissions were on average 17.5 times higher than those of the MB95 scheme. This increased the disparity between the two dust-flux schemes by a factor of 2.

The correlation between the two dust-flux schemes was similar for the PM_{10} fraction (Figure 23). The same method was followed to calculate the free dust fraction for PM_{10} as for PM_{75} – with d in Equation 10 set to 10 µm. The free dust fraction (η_{mi}) for PM_{10} was applied to the MB95 scheme to correct for the predictions in the PM_{10} particle size group (Shao, 2008). On average, the correlation between MB95 and SH11 for PM_{10} was similar to that of PM_{75}, with the average emissions from SH11 between 1.7 and 8.2 times higher than those from the MB95 model. The Sulphur Paydam showed a similar poor correlation with the PM_{75} emissions by a factor of 37.

The effect from crusting on the PM_{10} MB95 emissions was the same as for PM_{75} with an overall reduction in emissions of 69%. This had a negative effect on the correlation between the two dust schemes with the difference between the SH11 and MB95 emissions increasing by an order of 20 times (Figure 25).

Field measurements on PM_{10} and $PM_{2.5}$ emission potentials from soils by Chandler *et al.* (2002) provide a relation between the fraction of free dust (η_{mi}) and aggregated dust (η_{fi}) of 0.22. As indicated in Section 4.2, the η_{mi} as obtained from the Malvern Analyser is closer to the η_{fi} and this could be the cause for the higher emissions provided by the SH11 dust-flux scheme. By correcting for the η_{mi} fraction – through the Chandler ratio (referred to as $CF\eta_{mi}$ from here onwards), the correlation between the two dust schemes improved significantly resulting in an average correlation between 0.4 and 1.8 for SH11/MB95 (Figure 25). The correlation in the emission from the Sulphur Paydam also improved to 8 times for SH11/MB95.

Comparison between the PM_{75} and the PM_{10} emissions indicated PM_{75} to be 1.2 times higher, on average, than PM_{10} using the SH11 scheme. A similar relation applied to the MB95 scheme where the difference between the PM_{75} and the PM_{10} emissions was 1.3 times. This indicates that the free dust fraction or the minimally disturbed dust fraction (Table 9) within each size bin has a similar influence on both dust-flux schemes.
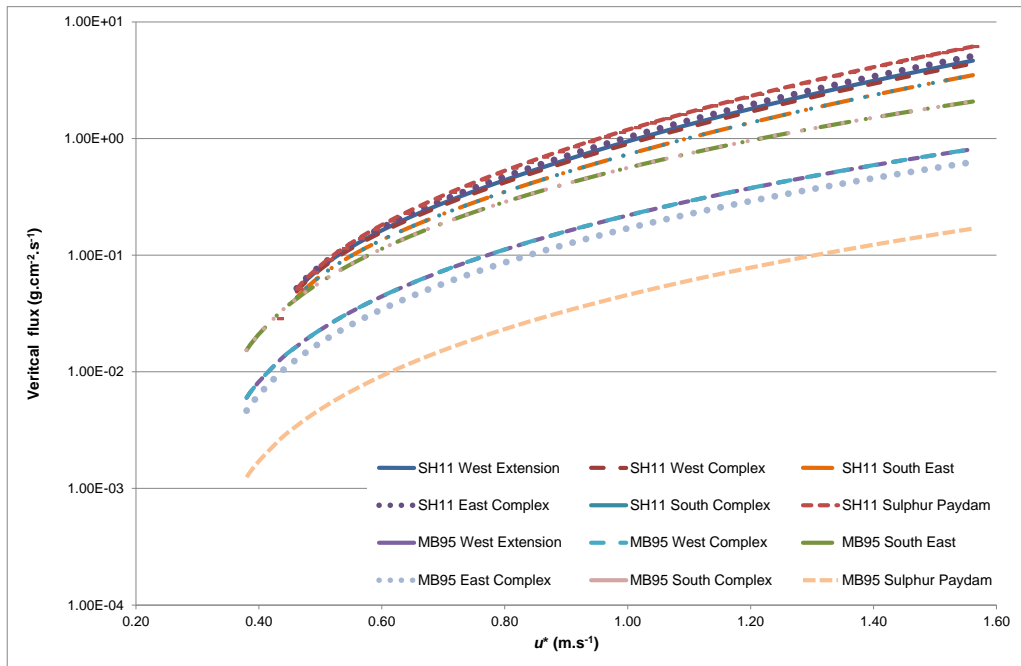
Figure 21: Comparison between the MB95 and SH11 PM$_{75}$ dust-flux emission rates for the six gold TSFs.
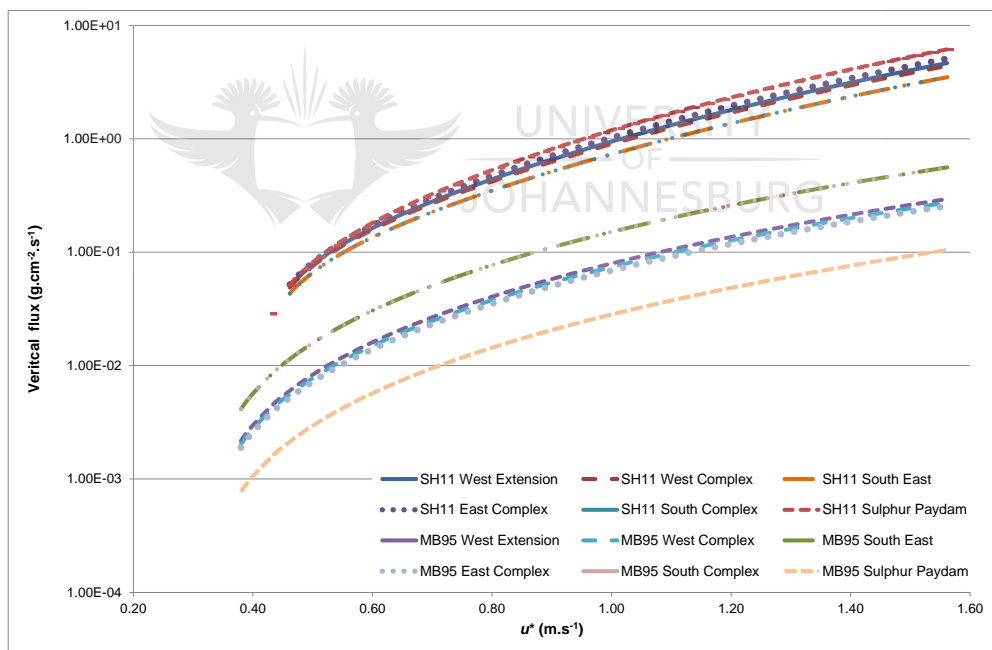
Figure 22: Comparison between the MB95 and SH11 PM$_{75}$ dust-flux emission rates for the six gold TSFs with the crusting corrections applied to MB95.
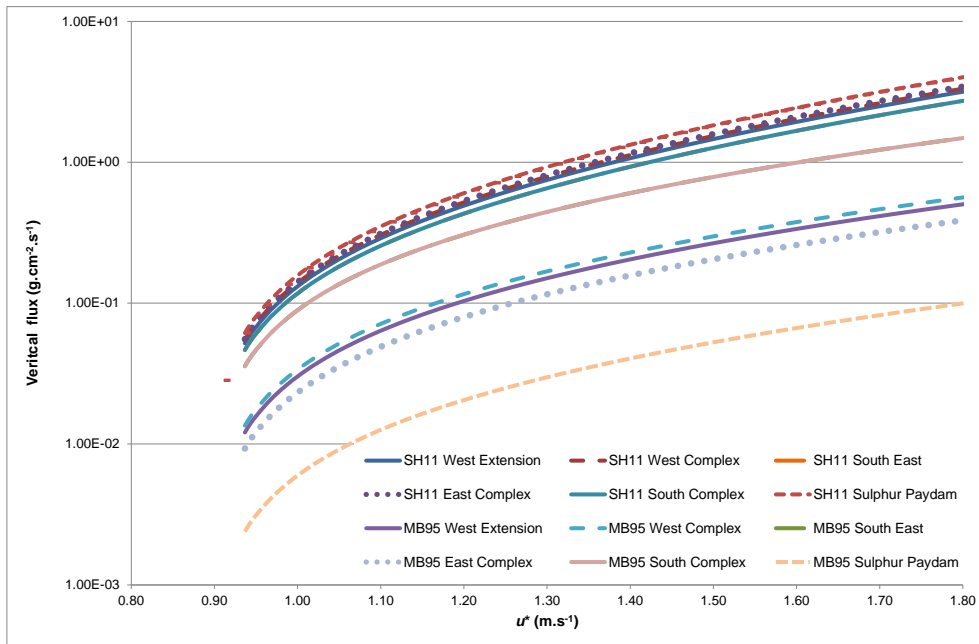
Figure 23: Comparison between the MB95 and SH11 PM$_{10}$ dust-flux emission rates for the six gold TSFs.
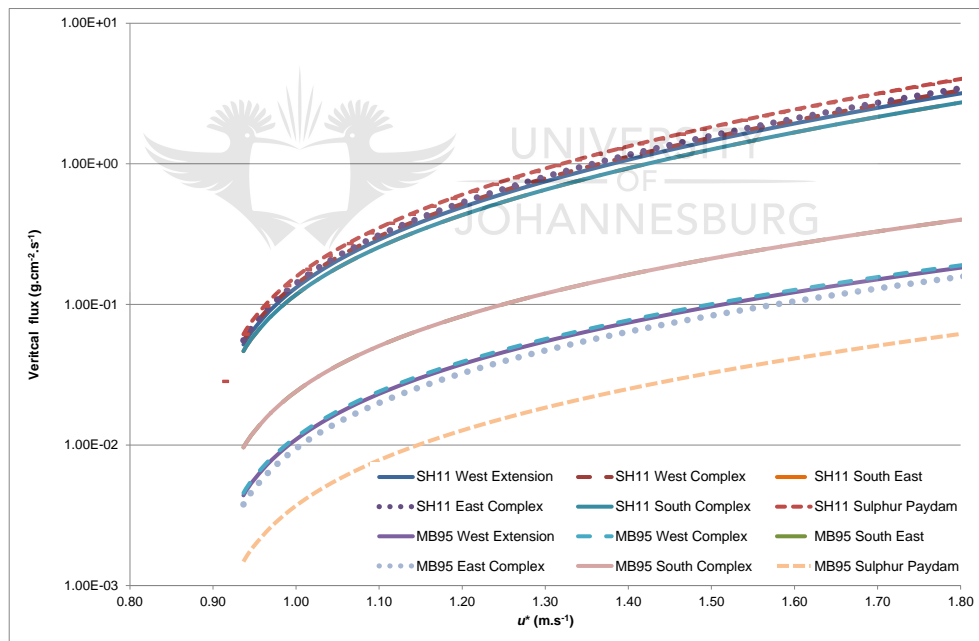
Figure 24: Comparison between the MB95 and SH11 PM$_{10}$ dust-flux emission rates for the six gold TSFs with the crusting corrections applied to MB95.
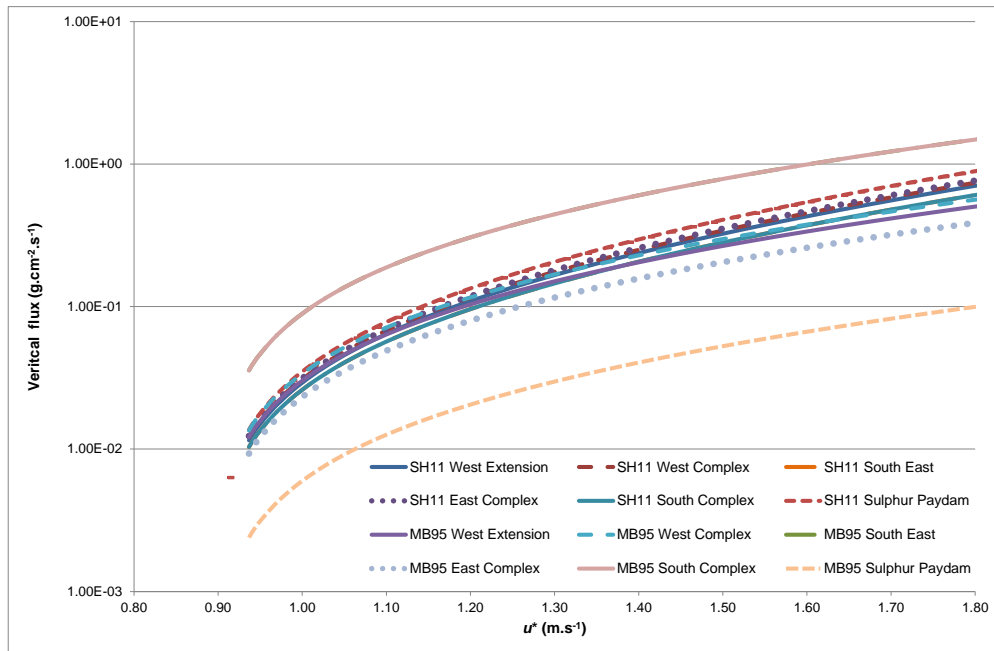
Figure 25: **Comparison between the MB95 and SH11 PM$_{10}$ dust-flux emission rates for the six gold TSFs with the η_{mi} correction factor for applied to SH11.**

4.4 Platinum Tailings Storage Facility Case Study

4.4.1 Data acquisition and analysis

The same methodologies as applied to the gold TSFs were used to determine the platinum TSF *psd*. A composite sample was taken from the Impala No. 2 tailings dam (referred to as TSF 7) and analysed for particle size distribution (*psd*) using the Malvern Particle Size Analyser. Particle sizes less than 477 µm were reported.

The TSF parameters used in the quantification of wind erosion emissions are provided in Table 13. The particle size distribution for the TSF surface, sidewall and sub-surface are presented in Figure 26.

The lognormal particle size distribution (Figure 26) had the mode at 121 µm indicating the largest portion of platinum tailings fell within the coarse fraction. The percentage of material with *d* < 10 µm was 15%, and the fraction where *d* < 75 µm was 58%.

The clay content of the platinum TSF (Table 13), was 4.2% with a silt content of 59% and 47% sand content. The sodium and calcium contents were obtained from similar platinum tailings material and applied to the TSF7 though Equation 13. This resulted in a lower horizontal pressure value than the interpolated value for *P*. As explained under Section 4.3.1, the uncertainties around the input parameters used in Equation 13 dictated the use of the interpolated value for *P*.

The modes were calculated with the nonlinear least-squares fitting techniques and are graphically presented in Figure 27. The minimally dispersed particle fractions (η_{mi}) for the platinum TSF for the three particle size bins of $PM_{2.5}$, PM_{10} and PM_{75} is given in Table 12.

Table 12: Minimally dispersed particle fraction $p_m(d)$ for the three particle size bins of $PM_{2.5}$, PM_{10} and PM_{75} for the platinum TSF.

Modes	Percentage of $p_m(d)$ fractions		
	$PM_{2.5}$	PM_{10}	PM_{75}
	(d < 2.5 µm)	(d < 10 µm)	(d < 75 µm)
TSF 7	0.04	0.15	0.58
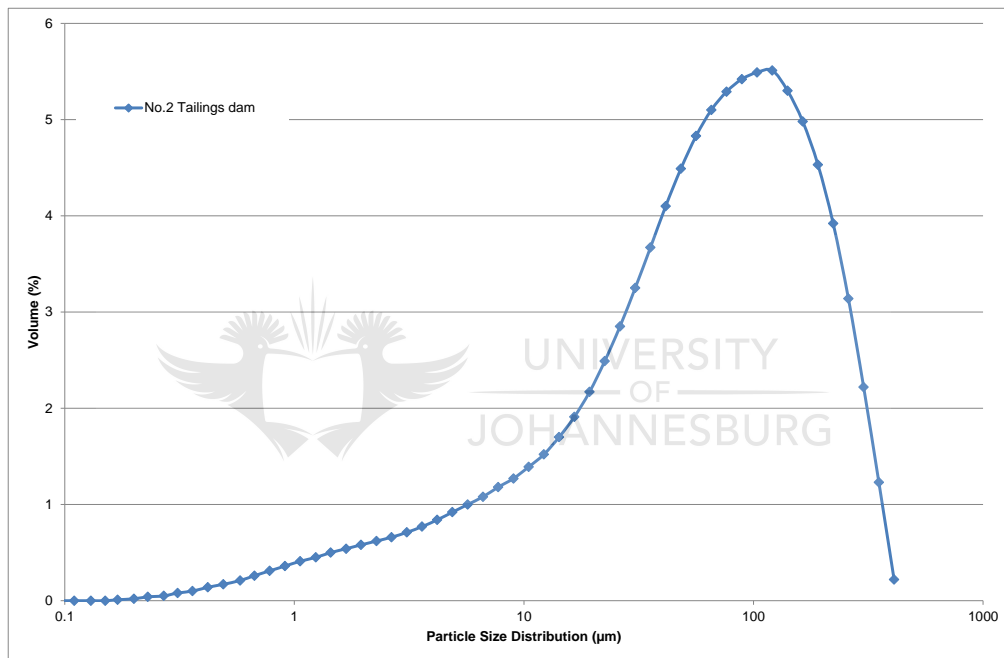
Figure 26: Particle size distribution for the Impala Platinum No. 2 Tailings (TSF7).

Table 13: Lognormal distribution parameters for the Impala Platinum No. 2 Tailings (TSF7) based on particles size analysis.

Source	Source Code	% Clay (< 2 μm)	% Silt	% Sand	Mode 1			Mode 2			Mode 3		
					w	ln(*D*)	σ	w	ln(*D*)	σ	w	ln(*D*)	σ
Active No. 2 TSF	TSF7	4.2	48.5	47.3	0.3	12.2	1.5	0.5	70.7	0.7	0.2	178.0	0.4

Table 14: Selected input parameters for the three areas of the Impala Platinum No. 2 Tailings (TSF7) for the various dust emission schemes.

Source	Source Code	% Clay (<4 μm)[a]	% Salt[b]	% CaCO$_3$[c]	% Moisture content	Particle density (kg m^{-3})[d]	*P* interpolated (Pa)	*P* calculated - non-mica (Pa)	K(Q) crusting ratio[e]	K(F) crusting ratio[e]	Cy
Active No.2 TSF	TSF7	7.0	0.7	2.8	0.2	2 145	12 106	7 899	128.9	2.11	6.2E-05

[a] Definition for clay content as used in Equation 8 (Gillette *et al.*, 1982).

[b] Based on the sodium content from Crocodile River Platinum Mine TSF.

[c] Based on calcium content from Crocodile River Platinum Mine TSF.

[d] From similar platinum tailing impoundments (Zumdahl *et al.*, 2002).

[e] Based on the interpolated horizontal pressure (*P*).
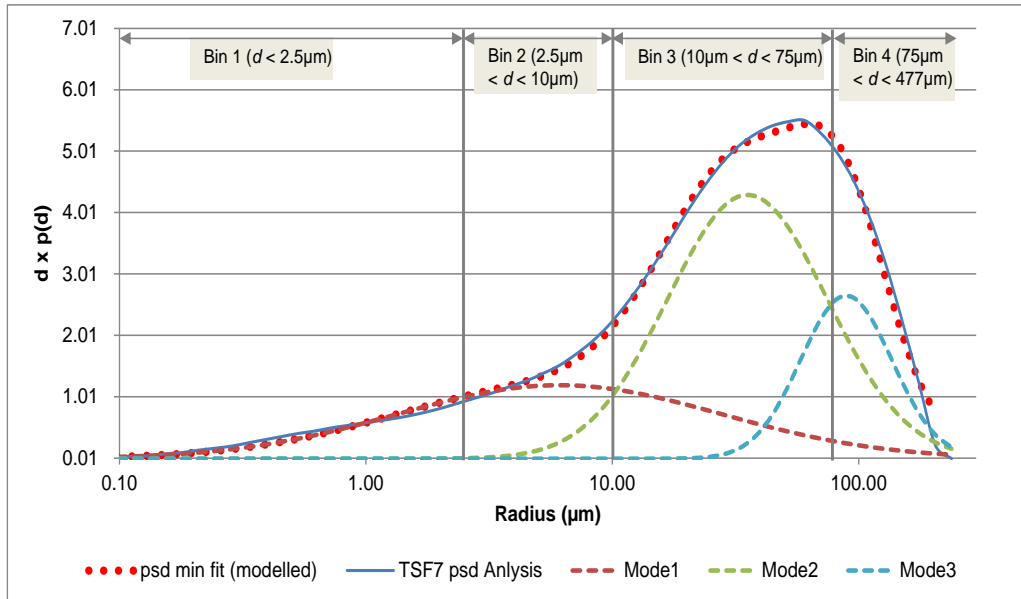
Figure 27: Least squares fit of a three-mode model applied to the measured particle size distribution of sample of tailings material from the Impala Platinum No. 2 Tailings (TSF7).

4.4.2 Emission quantification and results

The moisture content of 0.22% on the surface material increased the friction velocity (u^*) of the horizontal flux from 0.21 to 0.25 m s^{-1} for MB95 and to 0.29 m s^{-1} for SH11. The application of the drag partitioning increased it further to 0.33 m s^{-1} for MB95 and 0.38 m s^{-1} for SH11.

The disagreement between the dust-flux rates (g cm² s^{-1}) for the platinum TSF7 for the two schemes of MB95 and SH11 are shown in Figure 28. In general, the correlation between the two models at high wind speeds can be regarded as poor, with SH11 at 28 times; a difference of 14 times applied to the low wind speeds. Thus, in the case of the platinum tailings, the correlation between the two dust-flux schemes was, on average, worse than for the gold TSFs.

As with the gold tailings, introducing P to the MB95 dust-flux scheme caused a large reduction in MB95 emissions, increasing the disparity between the SH11 and MB95. By applying the crusting correction factor for the horizontal saltation flux (Q) a reduction in emissions from MB95 was 99%; the correction factor for the vertical dust-flux (F) resulted in a reduction of 53% (Figure 29).

The association between the two dust emission schemes remained the same for the finer fractions of PM$_{10}$ (Figure 30). The relation of SH11 versus MB95 was, on average, 29. When the outer threshold limits are compared, the comparison was good at lower wind speeds, with SH11 a factor of 3.6 higher than MB95. The correlation declined with an increase in wind speed.

The effect of P on the PM$_{10}$ emission rates was similar to the effect on PM$_{75}$. As indicated in Figure 31, the MB95 emission rates decreased significantly, resulting in a large disagreement with

the SH11 emission rates. With the crusting correction factor applied to the horizontal saltation flux (K_Q) a reduction in MB95 emission rates of 98% was achieved; only a 21% reduction resulted from the vertical dust-flux crusting factor (K_F).

The correction factor for η_{fi} to η_{mi} was 0.22 (Chandler *et al.*, 2002). Figure 32 provides the comparison between SH11 and MB95 PM_{10} emission rates, with the correction factor applied to the η_{mi} in the SH11 dust-flux scheme. In the case of the platinum tailings (TSF7), the correlation between the two dust-flux schemes improved significantly, with SH11 only 8 times higher than MB95.

The ratio between the PM_{75} and the PM_{10} emissions was a factor of four. This was true for both the SH11 and MB95 dust emission schemes.
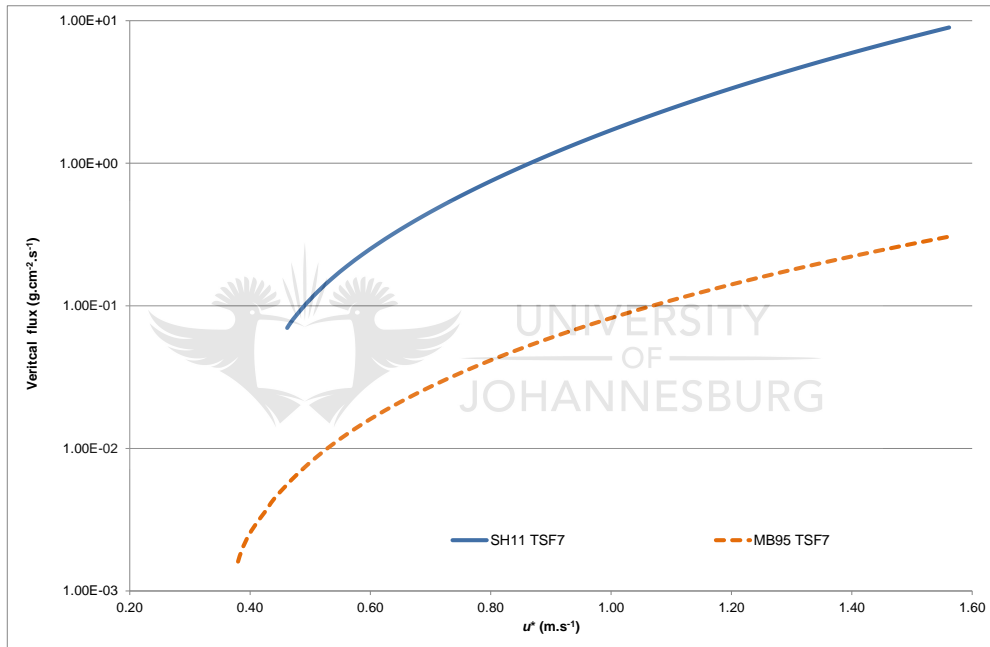
Figure 28: **Comparison between the MB95 and SH11 PM_{75} dust-flux emission rates for the platinum TSF.**
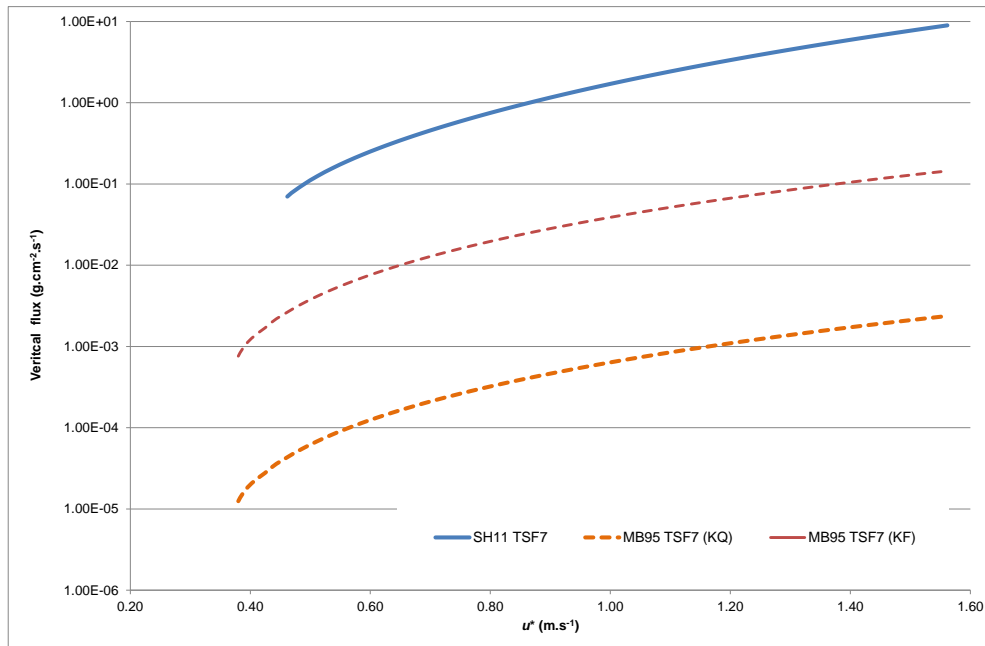
Figure 29: Comparison between the MB95 and SH11 PM$_{75}$ dust-flux emission rates for the platinum TSF with the crusting correction applied to MB95.
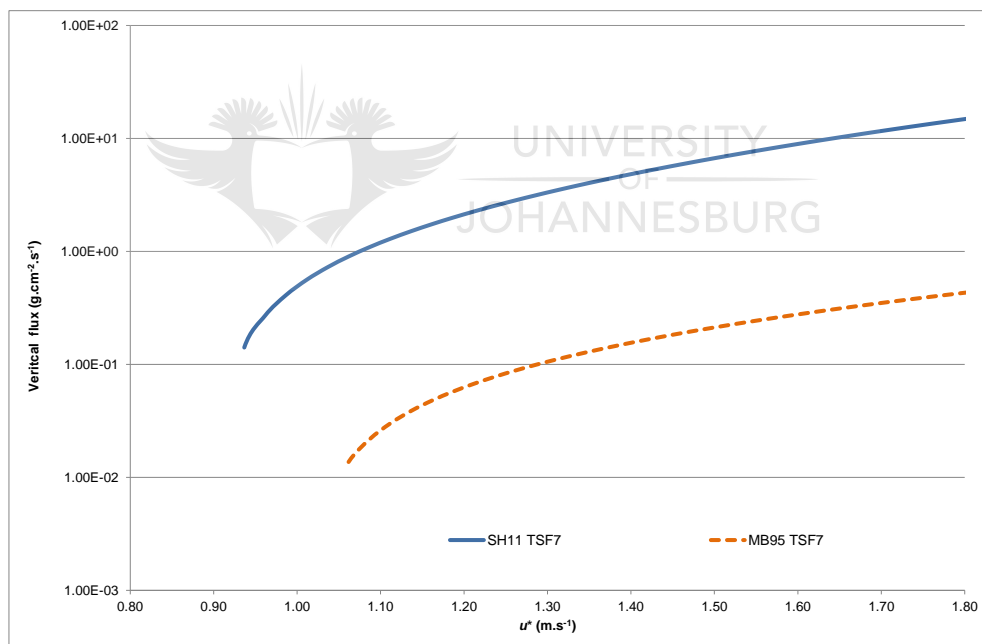
Figure 30: Comparison between the MB95 and SH11 PM$_{10}$ dust-flux emission rates for the platinum TSF.
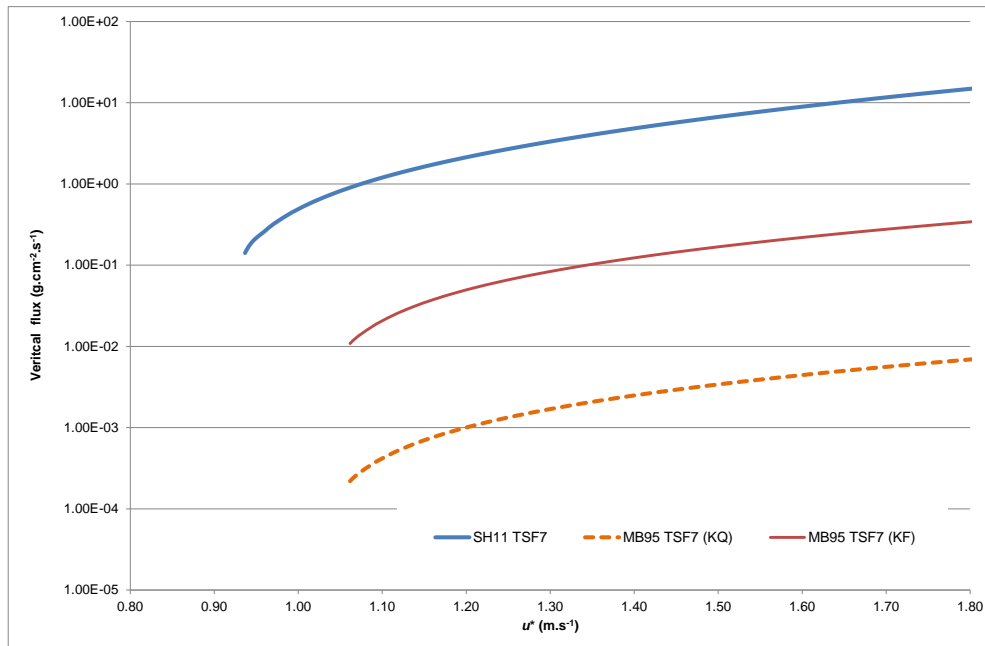
Figure 31: Comparison between the MB95 and SH11 PM_{10} dust-flux emission rates for the platinum TSF with the crusting corrections applied to MB95 for the platinum TSF.
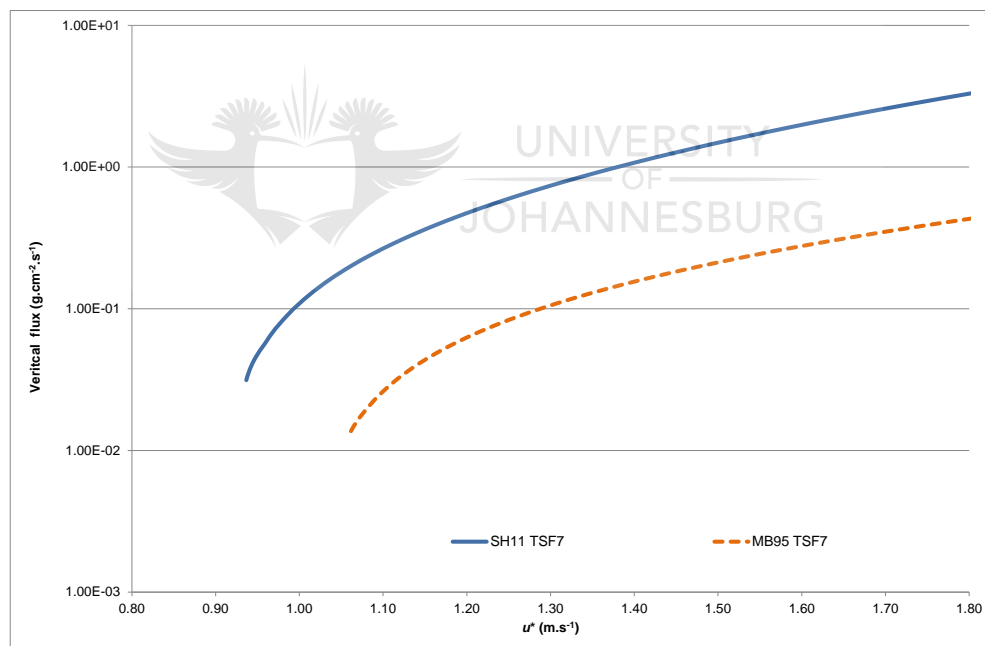
Figure 32: Comparison between the MB95 and SH11 PM_{10} dust-flux emission rates for the platinum TSF with a η_{mi} correction factor for applied to SH11.

4.5   Coal-fired Power Station Ash Storage Facility Case Study

4.5.1   Data acquisition and analysis

Whereas mine tailings material result from mechanical processes, coal ash, comprising both fly ash and bottom ash, is a result of combustion processes resulting in spherical fly ash particles (Boswell, 1986).

Figure 33 reflects the *psd* for Tutuka and Majuba ASFs, with the latter comprised of much coarser particulates. The lognormal size distribution showed the Tutuka ASF mode near 141 μm; Majuba was 36 μm. The fine fraction, however, was very similar between the two sites – with Tutuka at 19% and Majuba at 15% for the *d* < 10 μm fraction.

The clay content in the ash material was low (average 1.88%) when compared with the clay content in the gold tailings (average of 21%). For Tutuka the clay content was 3.3% but only 0.4% for Majuba. The largest fraction of material for both the ASFs fell within the silt category, with 56% of the Tutuka ASF at less than 65 μm and 71% of the Majuba ASF also less than 65 μm (Table 16).

The same methodology (as applied to the gold and platinum tailings to determine the minimally dispersed fraction $p_m(d)$ or free dust fraction) was applied to the ASFs (Table 15 and Figure 34).
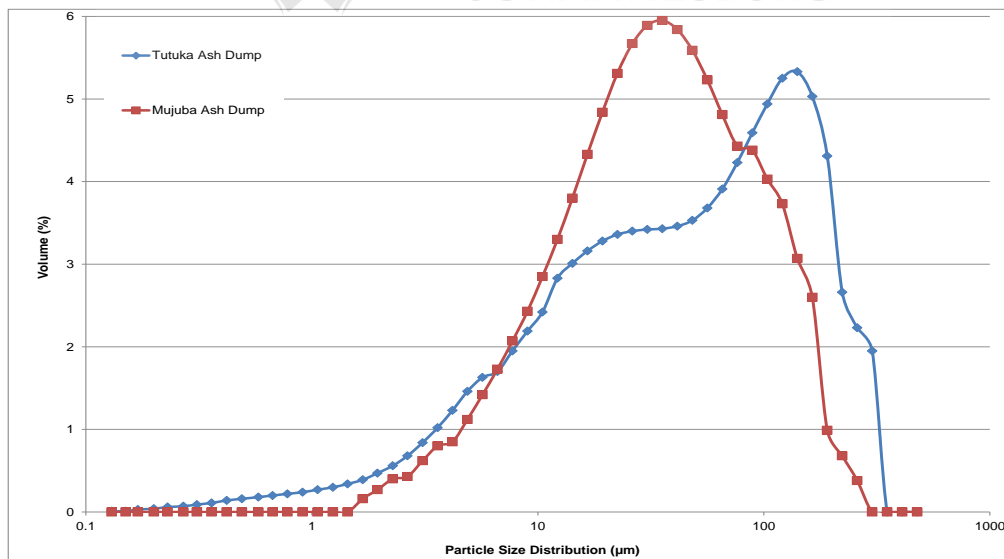
Figure 33:   Particle size distribution for the Tutuka and Majuba ASFs.

Table 15: Minimally dispersed particle fraction $p_m(d)$ for the three particle size bins of PM$_{2.5}$, PM$_{10}$ and PM$_{75}$ for the platinum TSF.

| Modes | Percentage of $p_m(d)$ fractions | | |
| | PM$_{2.5}$ | PM$_{10}$ | PM$_{75}$ |
	(d < 2.5 μm)	(d < 10 μm)	(d < 75 μm)
ASF 1	0.02	0.14	0.55
ASF 2	0.00	0.10	0.71

(a)

(b)
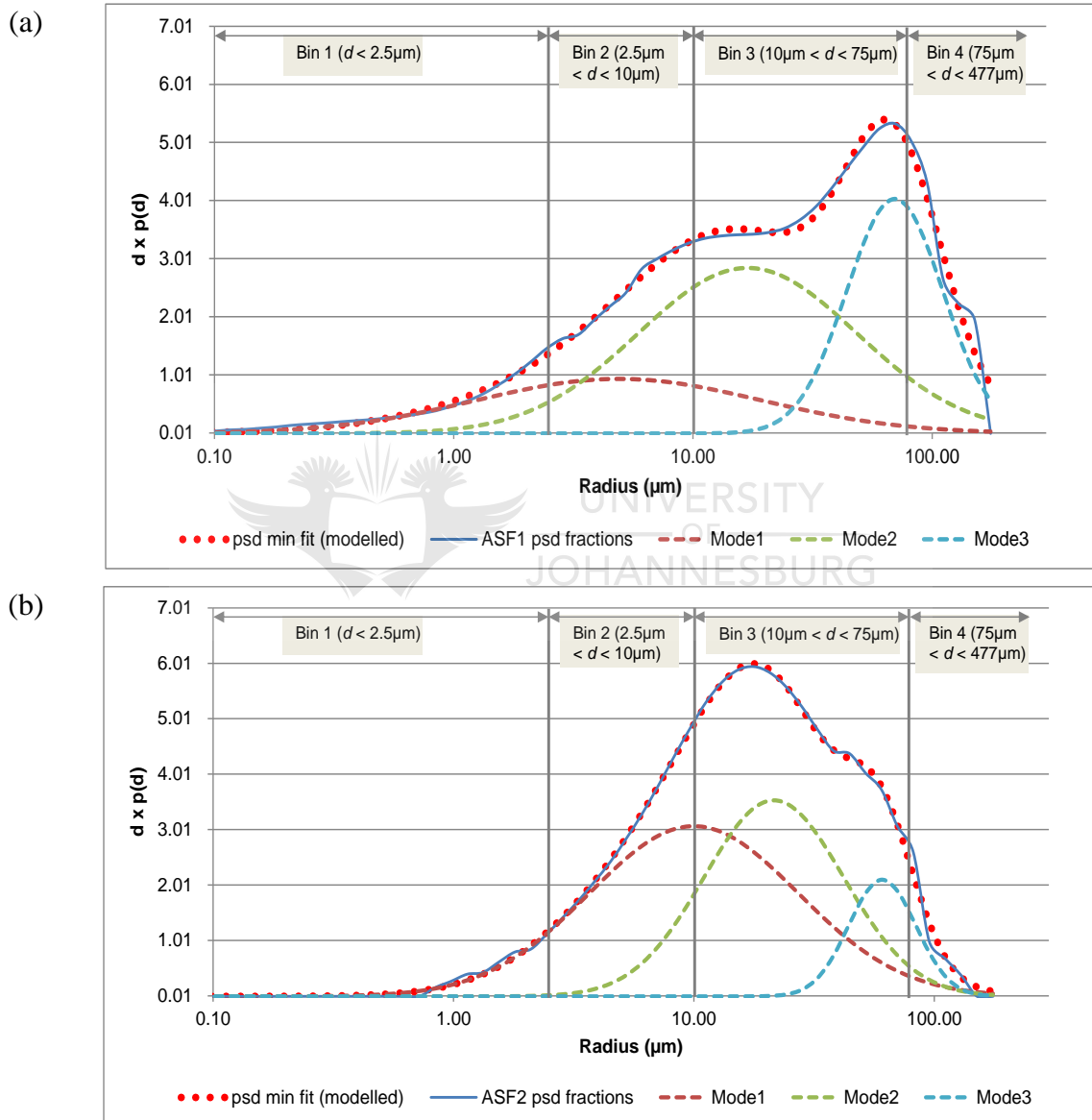
Figure 34: Least squares fit of a three-mode model applied to the measured particle size distribution of sample of ash material from the (a) Tutuka and (b) Majuba ASFs.

Table 16: Lognormal distribution parameters for coal ASFs based on particles size analysis.

Source	Source Code	% Clay (< 2 µm)	% Silt	% Sand	Mode 1			Mode 2			Mode 3		
					w	ln(D)	σ	w	ln(D)	σ	w	ln(D)	σ
Tutuka	ASH1	3.3	56.2	40.5	0.2	9.8	1.4	0.5	33.9	1.4	0.3	139.7	0.5
Majuba	ASH2	0.4	75.3	24.3	0.5	20.0	1.0	0.4	43.0	0. 7	0.1	121.6	0.3
Average		1.9	65.7	32.4									
Standard deviation		0.01	0.1	0.08									

Table 17: Selected input parameters for coal ASFs for the various dust emission schemes.

Source	Source Code	% Clay (<4 µm)[a]	% Salt[b]	% CaCO$_3$[c]	% Moisture content	Particle density (kg m^{-3})	P interpolated (Pa)	P calculated – non-mica (Pa)	K(Q) crusting ratio[d]	K(F) crusting ratio[d]	Cy
Tutuka	ASH1	6.4	0.5	3.1	0.9	1 515	12 837	5 216	144	2.33	5.77E-05
Majuba	ASH2	2.7	0.2	0.4	11.8	1 425	14 508	1 883	185	2.89	4.68E-05
Average		4.7	0.4	1.8	6.4	1 470	13 673	2 367	165	2.61	5.22E-05
Standard deviation		1.9	0.1	1.4	5.5	45	836	2 155	21	0.28	5.48E-06

[a] Definition for clay content as used in Equation 8 (Gillette *et al.*, 1982).

[b] Sum of sodium and potassium content.

[c] Based on calcium content.

[d] Based on the interpolated horizontal pressure (P).

4.5.2 Emission quantification and results

The MB95 and SH11 vertical flux rates (g cm² s^{-1}) (Figure 35) for the two Ash Storage Facilities indicated a large variation between the two dust emission schemes and between the two ASFs. The threshold friction velocity was quite different because of the difference in moisture content of the two ash samples. Tutuka ASF had a significantly lower moisture content – 0.9% in comparison to 11% from Majuba – which resulted in an increase in the threshold velocity of the MB95 approach to 0.24 m s^{-1}; for Majuba ash the u^*_t increased to 0.44 m s^{-1}. The moisture correction on u^*_t from the SH11 approach was 0.33 m s^{-1} for Tutuka and 0.60 m s^{-1} for Majuba. The effect from surface roughness through the drag partitioning increased u^*_t further to 0.24 m s^{-1} and 0.45 m s^{-1} for MB95 and 0.34 m s^{-1} and 0.62 m s^{-1} for SH, for Tutuka and Majuba, respectively. The calculated horizontal pressure (*P)* for Tutuka ASF was also 2.7 times higher than for Majuba ASF because of higher clay, salt and calcium content (Table 17).

Emission rates for Majuba ASF, as calculated with SH11, averaged 1.04 times higher than that for Tutuka ASF (Figure 35). The MB95 scheme had the opposite effect where Tutuka ASF results averaged 1.7 times higher emissions. This was because of the almost three times higher clay content in the Tutuka ASF compared with the clay content in the Majuba ASF. The SH11 versus MB95 relation differed by a factor of 13 for Tutuka and 14 for Majuba. On average, the difference between the two dust emission schemes was 14 times.

As with the other case studies, emissions from the MB95 scheme reduced significantly with the application of P to the Q_{MB95} or to the F_{MB95} (Figure 36). The crust correction to F (K_F) resulted in lower control efficiency than the crust correction applied to Q (K_Q).

Figure 37 shows the correlation between MB95 and SH11 dust emission rates for PM$_{10}$, with a similar correlation shown for PM$_{75}$. The influence of the moisture on differences between the two sites of u^*_t is clear in Figure 37, with an increase to 0.84 m s^{-1} (Tutuka) and 1.54 m s^{-1} (Majuba).

The relation between SH11 and MB95 for the Tutuka and Majuba ASFs (Figure 38) indicates, on average, SH11 to be orders of magnitude higher than MB95. The emission reduction caused by introducing P to MB95 was 99% for both Tutuka and Majuba by applying K_Q, and was 57% for both when applying K_F.

As with the tailings examples, the correlation between the SH11 and MB95 dust-flux schemes improved noticeably when the correction factor η_{mi}/η_{fi} was applied (Figure 39). On average, the Tutuka emissions from the SH11 scheme reduced from a 14 times higher emission than the MB95 scheme (without correction) to a 2.3 times difference. Similarly, the correlation for Majuba improved from an average 4.4 times difference to a 0.98 difference.

The difference in emissions for the PM_{75} fraction and the PM_{10} fraction is reflected in the percentage free dust for the two fractions (Table 16). The difference in PM_{75}/PM_{10} for Majuba was 7.2 and 4.0 for Tutuka.
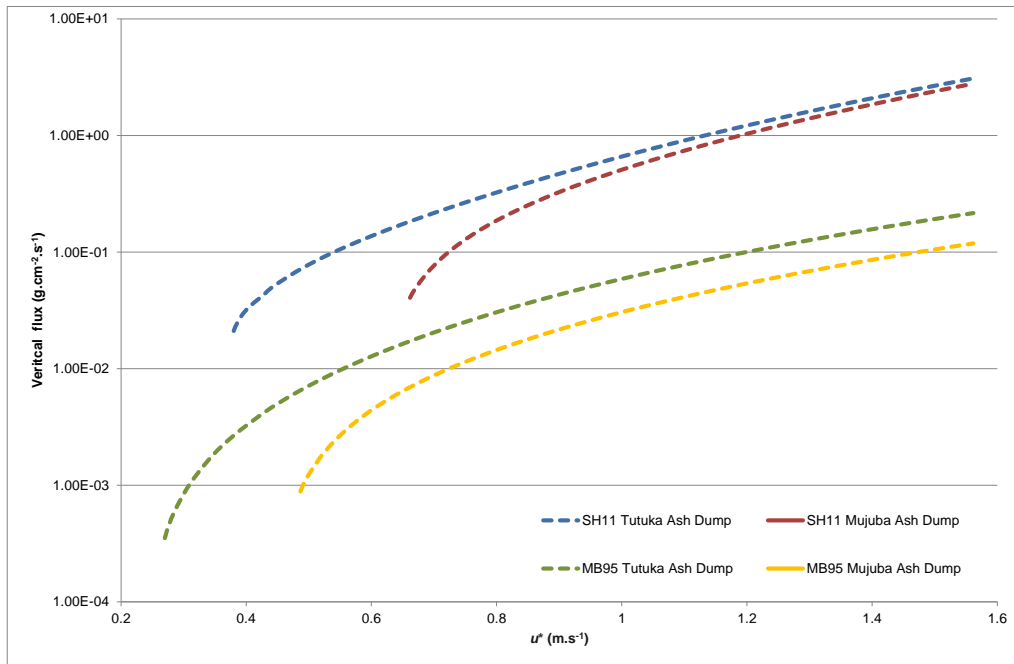
Figure 35: **Comparison between the MB95 and SH11 PM_{75} dust-flux emission rates for the ash storage facilities.**
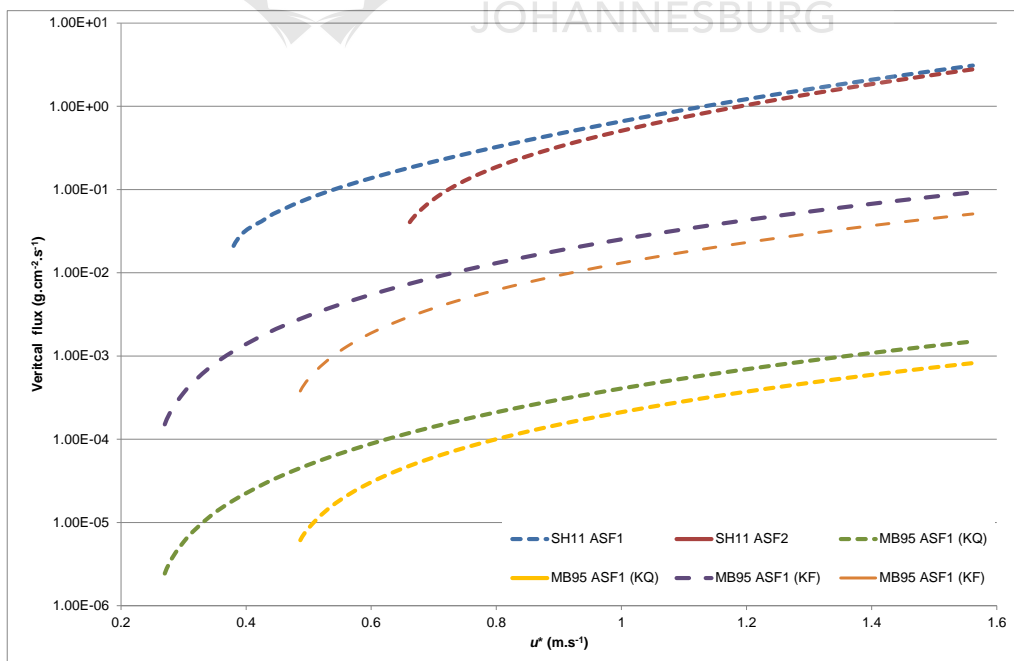
Figure 36: **Comparison between the MB95 and SH11 PM_{75} dust-flux emission rates for the ash storage facilities with the crusting correction applied to MB95.**
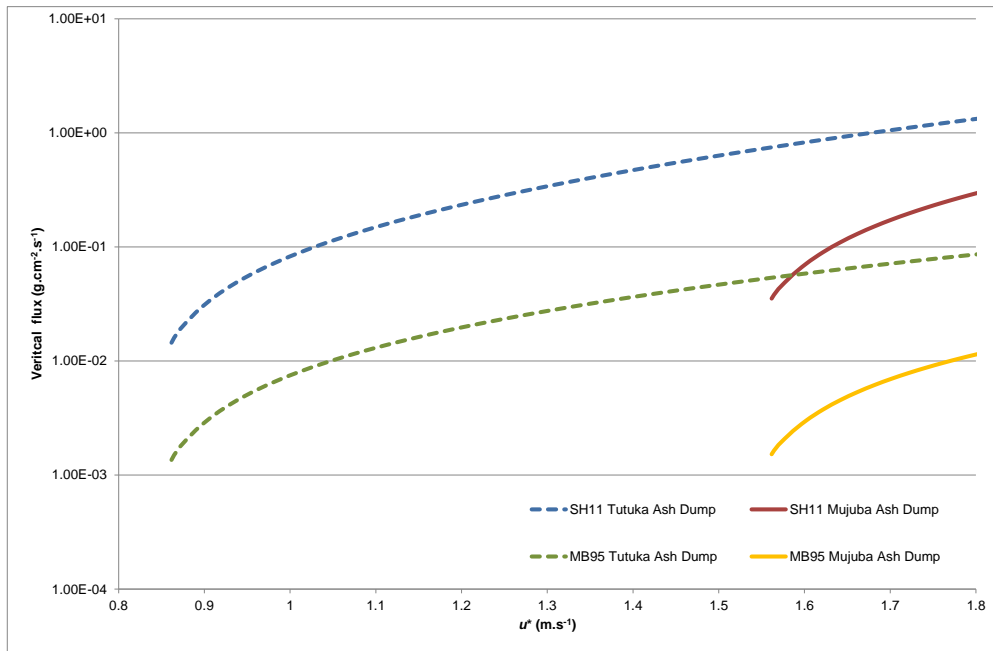
Figure 37: **Comparison between the MB95 and SH11 PM$_{10}$ dust-flux emission rates for the ash storage facilities.**
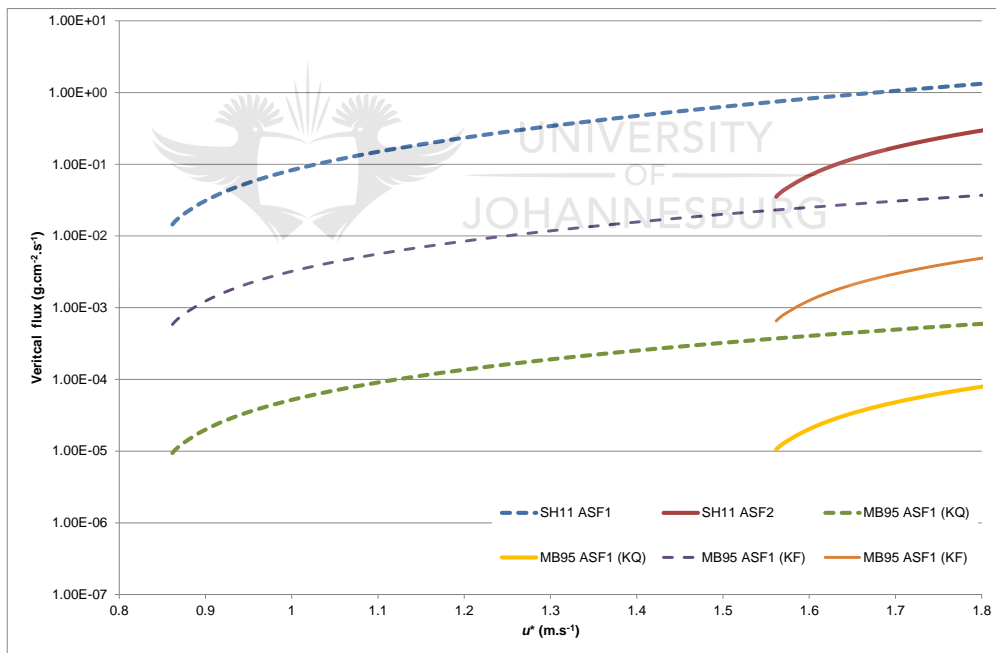
Figure 38: **Comparison between the MB95 and SH11 PM$_{10}$ dust-flux emission rates for the ash storage facilities with the crusting corrections applied to MB95 for the platinum TSF.**
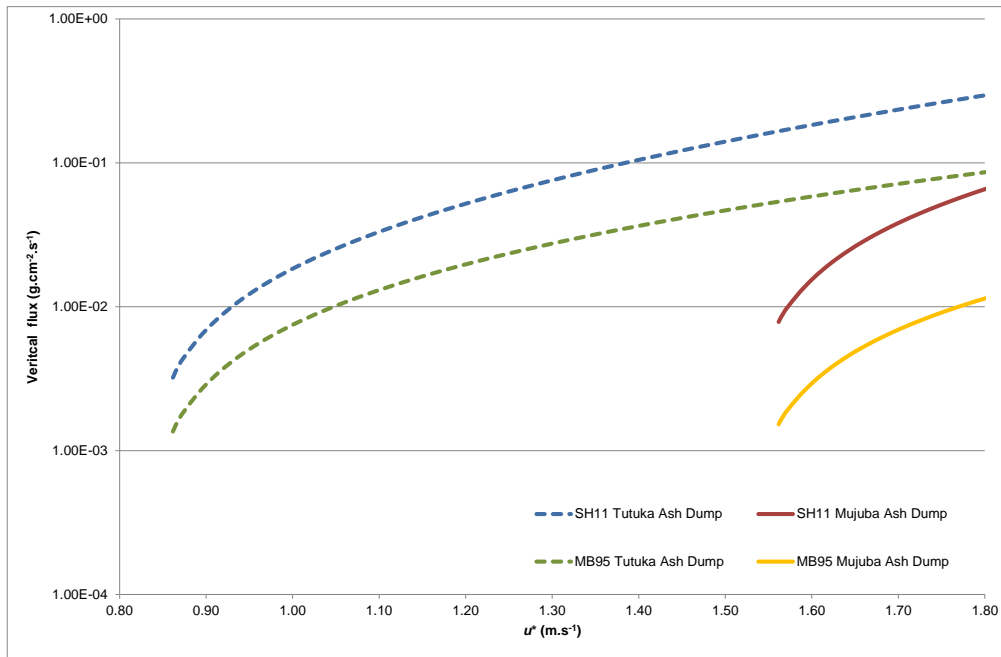
Figure 39: Comparison between the MB95 and SH11 PM_{10} dust-flux emission rates for the ash storage facilities with a η_{mi} correction factor for applied to SH11.

4.6 Sensitivity of the Dust Flux Schemes to Wind Speed Frequency

A field experiment conducted by Stout (1998) for averaging wind speeds over periods of 2, 5, 10, 20, 30, and 60 seconds showed that a time average over an hour could provide a threshold that is substantially lower – less than 50% – than the true threshold.

Testing the variability of dust-flux rates based on the wind speed frequency and averaging periods, two sets of data were used:

- Impala Platinum 10-minute meteorological data for the period 01 January to 31 December 2010;

- Klerksdorp 5-minute meteorological data for the period 01 January to 31 December 2012 as obtained from the South African Weather Services.

Emission rates were calculated with the SH11 and MB95 dust-flux schemes following the approaches set out in Figures 17 and 18, respectively. Two wind speed datasets were used – one based on 10-minute wind speed and wind direction data, and the other based on 5-minute data. For comparison two approaches were followed for each dataset:

- calculate the emission rates using the 10-minute and 5-minute wind velocities and then averaging the emissions to hourly rates;

- averaging 10-minute and 5-minute wind velocities to hourly averages and used these to calculate emission rates.

For the purposes of comparison, both the saltation flux rates (kg m^{-1} s^{-1}) and the dust-flux rates (g. m^{-2} s^{-1}) are shown for both the SH11 and MB95 approaches. Figure 17 and Figure 18 show that the two dust-flux schemes use different methods for the calculation of the threshold friction velocity, resulting in slightly different u^*_t values (Section 3.2.3). The use of different methods had a significant influence on the emissions calculated through their influence on both the threshold velocity and the saltation flux.

4.6.1   10-minute dataset

Figure 40(a) represents the saltation flux (Q) for the 10-minute wind dataset showing the number of hours where $\frac{Q_{10min} - Q_{hourly}}{Q_{10min}}$ provided values of between 0 and 1. A value of 0 indicates similar emission rates from both the 10-minute and the hourly averages. A value of 1 indicates a poor correlation, i.e. where Q_{10min} resulted in much higher emissions than Q_{hourly}. A good correlation – of 0 – was only found when both approaches resulted in zero emissions – these were omitted from the comparison – only the hours where there were emissions recorded were used for comparison. The Shao and Lu (SH&L) u^*_t resulted in 466 hours with emissions calculated, of which 358 hours showed a poor correlation of 1. Similarly, the MB95 u^*_t resulted in 1 049 hours with calculated emissions; of these hours 719 hours displayed a poor correlation between the two approaches. For many of the hours where the correlation was 1, the 10-minute data had calculated emissions; the hourly data had zero emissions. This resulted in large discrepancies between the averaged 10-minute emissions and the hourly emissions for the same hour.

The same approach was followed for the dust-flux (F) quantification (Figure 40(b)) with similar results as those for the saltation flux rates (Figure 40(a)). For MB95, as expected, the trend was the same as for Q, since F_{MB95} is a direct function of Q. The SH11 dust-flux rates (F_{SH11}) resulted in slightly different correlations because of the dependency of F_{SH11} on u^*. The number of hours with a correlation of 1 remained at 358, but the correlation between the 10-minute rates and the hourly rates decreased slightly, with fewer hours falling within the 0-0.2 bin (Figure 40(b)).

The difference between the 10-minute emission rates and the hourly emission rates differed as much as 50 times (SH11) and 41 times (MB95) – with MB95 having one extreme hourly difference of 61 160 for Q_{10min}/Q_{hourly}. The reason for this disparity was the difference in the 10-minute u^* values versus the hourly averaged u^*. For the six 10-minutes within that hour, u^* was respectively 0.11; 0.13; 0.19; 0.32; 0.32 and 0.28 m s^{-1}; however the hourly averaged u^* was 0.204 m s^{-1}. With u^*_t at 0.203 m s^{-1}, the hourly averaged u^* was just above u^*_t resulting in weaker wind erosion. Even though three of the 10-minute u^* values were below the threshold resulting in no emissions, the other three were well above the threshold and with the saltation flux dependency on u^{*3}, the resulting rates were significantly higher (Table 18). On average, the difference was 2.8

times higher emissions from 10-minute emissions than hourly emissions for both Q_{SH} and Q_{MB}, excluding the one extreme hourly value for Q_{MB}.

Figure 40: Correlation between 10-minute and hourly (a) saltation flux rates and (b) dust emission rates for the SH11 and MB95 approaches using 10-minute wind data.

Table 18: Disparity in the saltation flux rate (Q_{MB}) for the extreme hour in the 10-minute dataset because of the influence of u^*.

	10-minute data			Hourly data		
Time	Wind Speed (m s^{-1})	u^* (m s^{-1})	Q_{MB} (kg m^{-1} s^{-1})	Wind Speed (m s^{-1})	u^* (m s^{-1})	Q_{MB} (kg m^{-1} s^{-1})
17h00	2.05	0.11	0			
17h10	2.35	0.13	0			
17h20	3.5	0.19	0			
17h30	5.8	0.32	1.07E-02			
17h40	5.8	0.32	1.07E-02			
17h50	4.95	0.28	5.35E-03			
Average	4.1(a)	0.2	8.93E-03	3.66(b)	0.20	4.46E-03
Ratio between 10-minute average & hourly data (Q_{10min}/Q_{hourly})						30 531

Notes: (a) Scalar average

(b) Vector average

4.6.2   5-minute dataset

A similar correlation was found between the 5-minute and hourly data (Figure 41). Similar to the 10-minute data, good correlation of zero linked with zero emission rates in both approaches. The Shao and Lu (SH&L) u^*_t resulted in 0 for a total of 7 089 hours, with 7 679 hours for the MB u^*_t (Figure 41(a)). The Shao and Lu (SH&L) had 1 032 hours with a poor correlation of 1; the MB u^*_t had 721 hours. It should be noted that 2012 was a leap year with a total of 8 784 hours.

The dust-flux (F) emissions (Figure 41(b)) resulted in similar correlations as the saltation flux rates (Figure 41(a)). For MB95, as expected, the trend was the same as Q since F_{MB95} is a direct function of Q. The SH11 dust-flux rates (F_{SH11}) resulted in slightly different correlations because of the dependency of F_{SH11} on u^*. The number of hours with a correlation of 1 remained at 358, but the correlation between the 10-minute rates and the hourly rates decreased slightly with fewer hours falling within the 0-0.2 bin (Figure 40(b)).

The 5-minute data did not result in the same disparity between the 5-minute and hourly averages as occurred with the 10-minute data. The largest difference between the Q_{5min}/Q_{hourly} was 377 times for hour 16h00 on 20 May 2012. The variation between the twelve 5-minute threshold velocities and the resulting saltation flux in comparison with the hourly average is provided in Table 19. For almost half of time, the five-minute averages did not result in any emission rates where the u^* was below the u^*_t of 0.25 m s^{-1}. The hourly average u^* of 0.25 m s^{-1} was just above the threshold, resulting in much lower saltation rates than when the 5-minute rates were averaged.

Table 19: Disparity in the saltation flux rate (Q_{MB}) for the extreme hour in the 5-minute dataset because of the influence of $u*$.

	5-minute data			Hourly data		
Time	Wind Speed (m s^{-1})	$u*$ (m s^{-1})	Q_{MB} (kg m^{-1} s^{-1})	Wind Speed (m s^{-1})	$u*$ (m s^{-1})	Q_{MB} (kg m^{-1} s^{-1})
16h00	4.5	0.25	0.00E+00			
16h05	4.4	0.24	0.00E+00			
16h10	4.8	0.27	1.28E-03			
16h15	4.8	0.27	1.28E-03			
16h20	4.9	0.27	1.80E-03			
16h25	4.6	0.26	2.89E-04			
16h30	4.6	0.26	2.89E-04			
16h35	4.9	0.27	1.80E-03			
16h40	4.7	0.26	7.73E-04			
16h45	3.9	0.22	0.00E+00			
16h50	4.3	0.24	0.00E+00			
16h55	4.3	0.24	0.00E+00			
Average	4.6(a)	0.25	6.26E-04	4.54 (b)	0.25	1.03E-05
Ratio between 5-minute average & hourly data (Q_{5min}/Q_{hourly})					337	

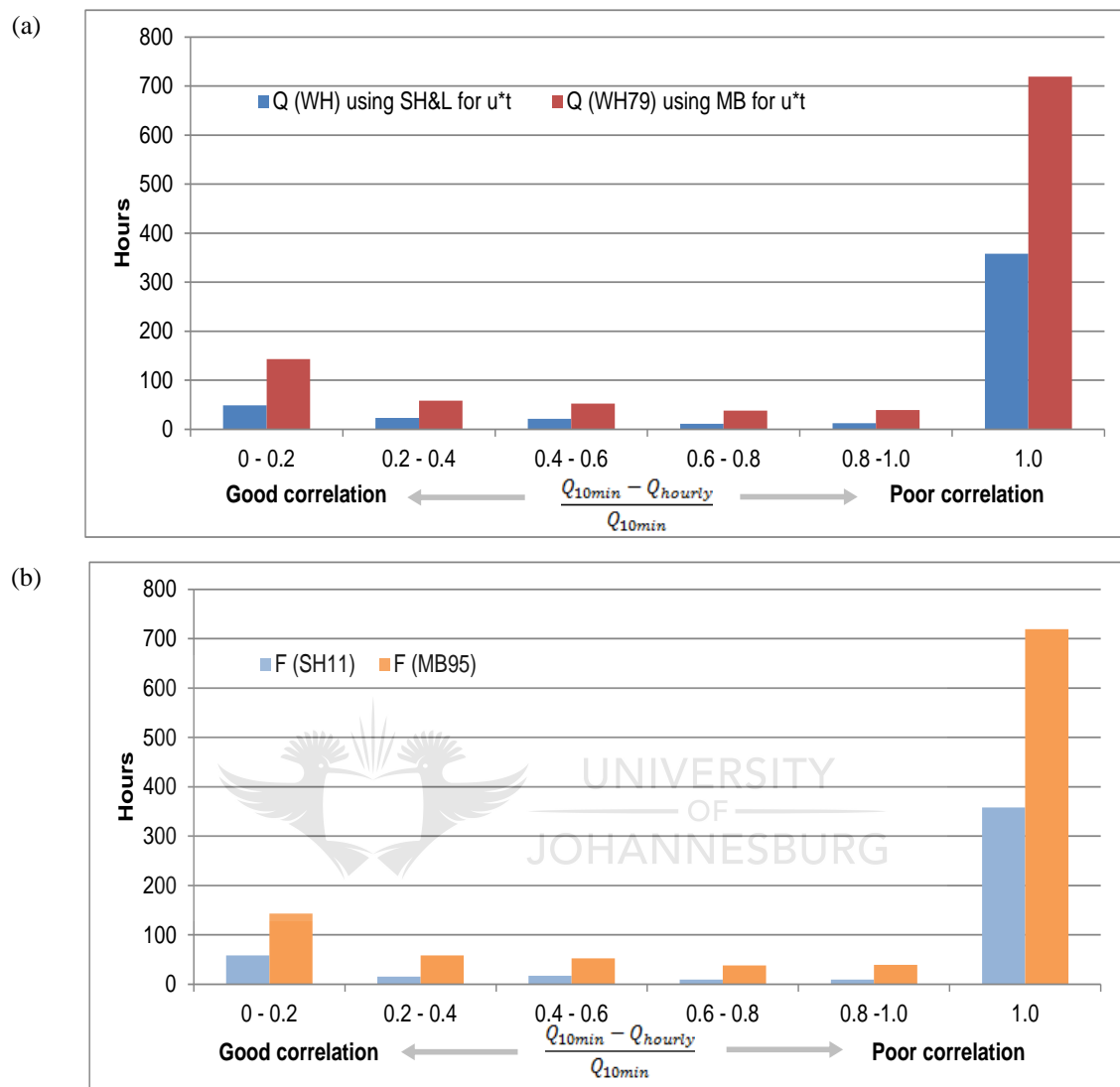**Notes:**   (a) Scalar average

(b) Vector average
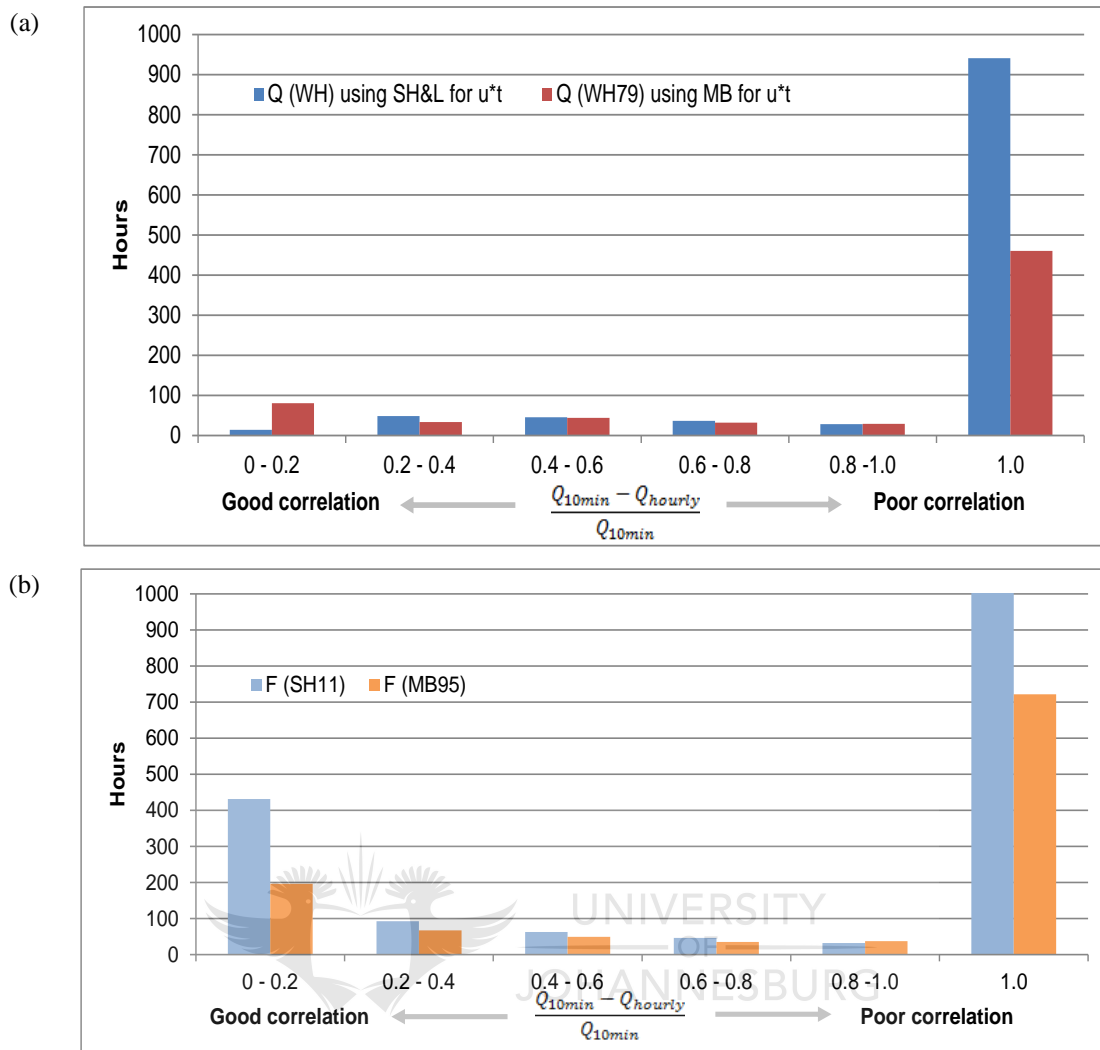
Figure 41: Correlation between 5-minute and hourly (a) saltation flux rates and (b) dust emission rates for the SH11 and MB95 approaches using 10-minute wind data.

4.7 Influence from Atmospheric Stability

Atmospheric stability is a direct function of processes at the Earth's surface, through a combination of heat and moisture exchanges and frictional drag causing retarded airflow. Thermal turbulence is typical of daytime atmospheric boundary conditions where heating of the Earth's surface causes the mixing layer to expand, resulting in unstable atmospheric conditions. During the night, the surface cools down, causing erosion of the mixing layer and the establishment of an inversion layer near the surface with limited vertical mixing. During windy and/or cloudy conditions, the atmosphere is normally neutral (Preston-Whyte & Tyson, 1988).

The wind speed profile followed a logarithmic distribution under neutral atmospheric conditions but would differ under either unstable or stable conditions (Section 3.1.2). For the comparison between the two dust-flux models, neutral atmospheric conditions were assumed. In reality, this would be different and the variation in emissions from neutral, stable and unstable conditions were tested.

The West Extension (TSF1) dataset was used, in combination with the Klerksdorp meteorological dataset for one calendar year (01 January to 31 December 2012). The dust-flux scheme of MB95 was applied due to its simplistic approach, with a roughness length (z_0) of 0.0012 m – based on typical roughness length for *short grass* (Burger, 1986) and a calculated threshold friction velocity of 0.24 m s^{-1}.

Atmospheric stability is frequently categorised into one of six stability classes. The categories and the percentage occurrences of the Klerksdorp data (01 January to 31 December 2012) are briefly described in Table 20. Hourly-average stability classes were determined though hourly wind direction, wind speed and calculated solar radiation. Very stable conditions occurred for 41%; neutral conditions occurred for only 5% of the time.

Table 20: Atmospheric stability classes and meteorological occurrences.

Designation	Stability Class	Atmospheric Condition	Occurrence at Klerksdorp (2012)
1	Very unstable	calm wind, clear skies, hot daytime conditions	11%
2	Moderately unstable	clear skies, daytime conditions	14%
3	Unstable	moderate wind, slightly overcast daytime conditions	20%
4	Neutral	high winds or cloudy days and nights	5%
5	Stable	moderate wind, slightly overcast night-time conditions	8%
6	Very stable	low winds, clear skies, cold night-time conditions	41%

The results (Figure 35) showed stability classes ranging between 1 and 6, with stability class 1 representing *very unstable* conditions and stability class 6 *very stable* conditions. The logarithmic wind field profile for neutral atmospheric conditions resulted in lower and less frequent emissions than the variable stability approach. Only the *unstable* (Stability class 3) and *neutral* (Stability class 4) stability classes resulted in emissions when the neutral atmospheric conditions wind field profile was applied to all the classes (Figure 35(b)).

On average, as shown in Figure 35(a), emissions were higher during *neutral* (Stability class 4) conditions for both approaches but more emissions (Figure 35(b)) were produced under *moderately unstable* (Stability class 2) and *unstable* (Stability class 3) conditions when the varying wind profile approach was applied. Both the neutral stability and the varying stability approach resulted in 349 hours of emissions. The variable stability wind profile approach showed emissions in all the classes except Stability classes 5 and 6 (Figure 35).
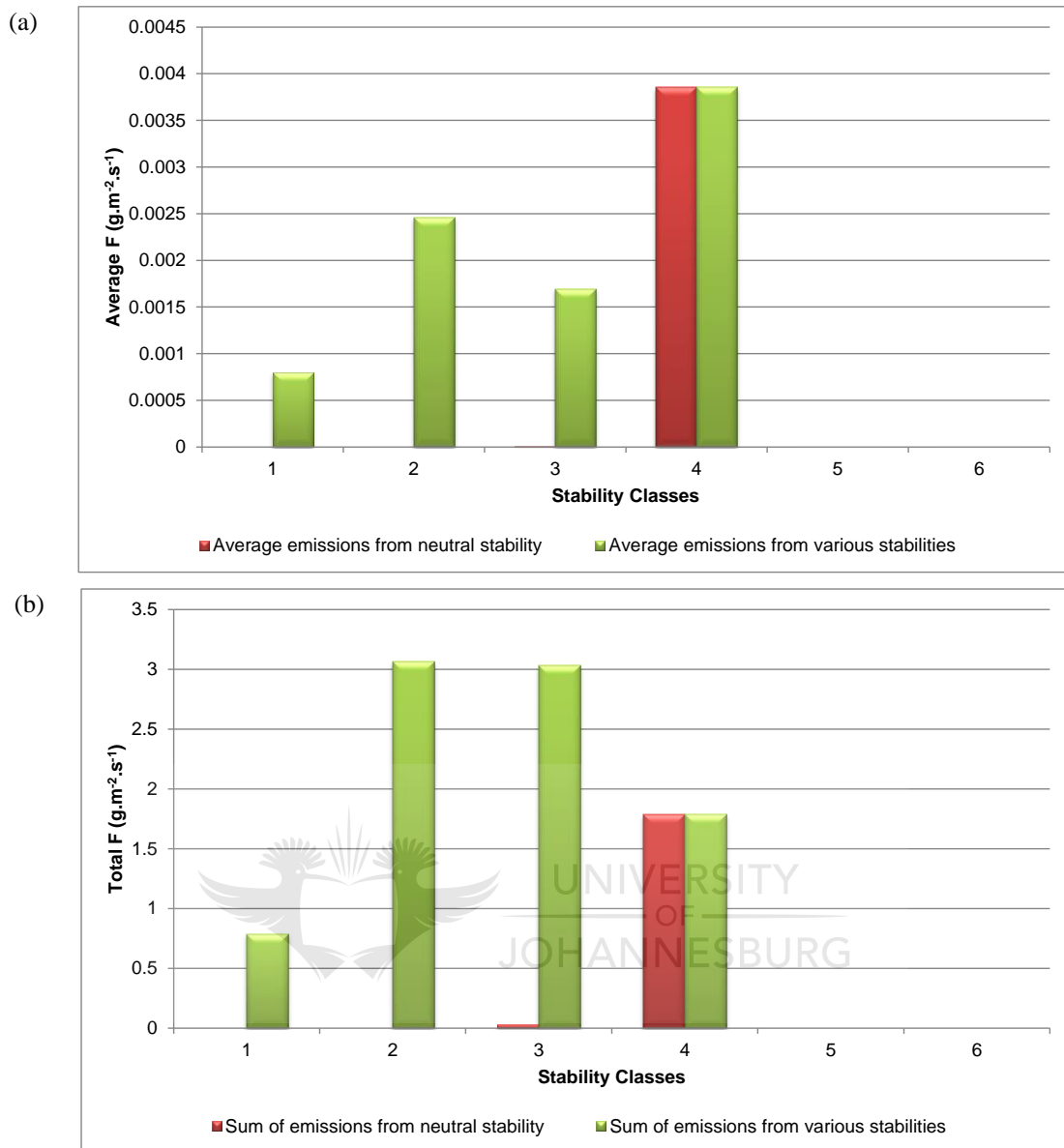
Figure 42: **Variance in the (a) average dust-flux *(F)* and (b) total dust-flux *(F)* between neutral- and varying-stability wind speed profiles.**

The varying stability approach resulted in emissions for 43% of the hours during *unstable* (Stability class 3); 28% of the hours during *moderately unstable* (Stability class 2) conditions; 17% during *neutral* (Stability class 4) conditions; 12% during *moderately unstable* (Stability class 2). By comparison, the neutral wind profile approach resulted in 96% of the hours resulting in emissions under *neutral* (Stability class 4) conditions, with 4% during *unstable* (Stability class 3) conditions.

Emissions from the variable stability wind profile approach, in comparison with the neutral stability wind profile, were significantly higher with a difference in total emissions of 4.8 times (Figure 35b) and on average, a factor of 2.3 (Figure 35a).

4.8 Discussion

The sensitivity of the two dust emission schemes to the various input parameters was confirmed through the application to tailings and coal ash bed material. The most profound parameter, P, was highly sensitive to the salt content in the tailings and ash material. Because of the limited information on the salt and $CaCO_3$ content in the tailings and ash, the uncertainty around the calculated value for P increased. For this reason, the interpolated value – even though based on natural soil – was regarded to be more representative and was used in all the applications.

In general, the correlation between MB95 and SH11 was fair, with better correlation found with the finer material (the younger gold TSFs) and poorer correlation between the coarser material. The correlation ranged between 1.5 and 7 times for the finer bed material and between 28 and 31 times for the coarser bed material. The ASFs resulted in a difference of 13 and 14 times higher emission rates from the SH11 approach than the MB95 approach. The correlation between the two dust schemes improved with an increase in wind speed.

By accounting for the effect of crusting (through the application of P to MB95), the emissions decreased significantly, resulting in a much larger discrepancy between the two dust schemes. The calculated crusting ratio – as applied to the saltation flux (Q) – resulted in control efficiencies of around 99%; where the crusting effect was applied to the dust-flux, (F) resulted in much lower control efficiencies, ranging between 21% and 69%.

The correlation between the two dust-flux schemes for the PM_{10} fraction was similar to the PM_{75} fraction. For the gold TSFs, a much better correlation was found for PM_{10}, with the average emissions from SH11 between 1.7 and 8.2 times higher than those from MB95.

With the application of a correction factor ($CF\eta_{mi}$) of 0.22 to the aggregated dust (η_{fi}) fraction in Equation 15, to make it representative of the free dust (η_{mi}) fraction, the correlation between the two dust-flux schemes improved significantly for all source material. For the gold tailings, the difference between the SH11 and MB95 PM_{10} emission rates decreased to fall between 0.4 and 1.8. This implies that the *psd* (as derived from the Malvern analysis) was more representative of the η_{fi} than the η_{mi}.

The sensitivity to the wind speed frequency indicated higher average emission rates when using the 10-minute or 5-minute wind speed intervals to quantify emission rates before averaging both these short period rates to hourly emission rates. By first averaging the wind speeds to hourly averages, the emissions were lower. On average, the significance was not great; ranging between 2.8 times for the 10-minute data and 1.3 times for the 5-minute data. However for the extreme values the discrepancies seem very high. This volatility was the result of the relationship between

u^* and u^*_t. as showed by the field experiment conducted by Stout (1998). Hourly averages tended to result in u^* closer to u^*_t, thereby resulting in lower saltation flux rates (Q), with Q influenced by u^*_3.

Applying the neutral logarithmic wind speed profile as a simplistic approximation would result in a significant under-estimation of the dust-flux emissions than what reality dictated, particularly where the wind erosion potential was influenced by a combination of stability classes.

5   Dispersion Modelling of Wind-Blown Dust: Case Studies

Dispersion models are useful tools in air quality management. Whereas ambient monitoring provides actual ambient concentrations for specific pollutants at set locations, atmospheric dispersion models can be used to simulate any number of pollutants and determine the impacts at any location within the modelling domain. In this section the two dust-flux schemes of Shao et al. (2011) and Marticorena and Bergametti (1995) are coupled with a regulatory Gaussian plume model to test the applicability of this method in the context of the established air quality impact assessment approach. This is done for two case studies, one includes two gold tailings storage facilities and the other a platinum tailings storage facility.

5.1   Methodology

Two case studies are included based on the information used in the previous section.

The first case study is for the West Extension and West Complex Gold TSFs at the AngloGold Ashanti Vaal River North operations. These two TSFs are located 1.5 km upwind (west-northwest) from the AngloGold Ashanti ambient monitoring station (Figure 43). Ambient PM_{10} monitored data are available for 15-minute intervals for the period 09 January 2012 to 16 August 2012. Even though the station does not record weather data, this was obtained from the South African Weather Services meteorological station in Klerksdorp, located 8 km northwest of the ambient station and 3 km north-northwest of the West Complex TSF.

The second case study is for the Impala Platinum Mine No. 2 Tailings Dam, where the Impala Platinum Luka ambient monitoring station is located 3.3 km west-northwest of the TSF. PM_{10} data were recorded at 10-minute intervals, with available data provided for the period 01 January 2009 to 31 December 2010. The ambient monitoring station is fitted with a weather station, recording wind direction, wind speed and temperature. Wind data for the same period as the ambient data were used for the dispersion modelling.

For each case study, emission rates were determined through the application of the dust-flux schemes of MB95 and SH11 (Figures 17 and 18 respectively) using real-time, near-site meteorological data.

The US EPA regulatory AERMOD model was used to simulate ground level PM_{10} (thoracic dust) concentrations from the calculated wind-blown dust-flux emissions. Firstly, the dust-flux emission rates were calculated for the same period and time interval as the available PM_{10} ambient

data. This was used to appraise the model results with, and to determine a representative roughness length (z_0) for, the dust-flux schemes. Once a representative z_0 has been determined, PM_{10} emission rates can be calculated for a full year of meteorological data and ground level concentrations can be simulated.

5.1.1 *Meteorological data*

Analysis of meteorological data is necessary to facilitate a comprehensive understanding of the wind field, largely influencing the dispersion of pollutants. The wind speed determines both the distance of downward transport and the dilution rate of pollutants. The generation of mechanical turbulence is similarly a function of the wind speed, in combination with the surface roughness.

Meteorological data – specifically wind speed; wind direction; temperature; relative humidity; atmospheric pressure; and rainfall – are required for input to the dispersion model. Wind speed, in turn, is used to calculate the friction velocity required by both the saltation flux and dust-flux schemes.

For Case Study 1, meteorological data from the South African Weather Services surface meteorological station in Klerksdorp for the calendar year 2012, provided as 5-minute recordings, were used. For Case Study 2, the 10-minute data from the Impala Platinum Luka station for the two years (2009 and 2010) were used.

AERMOD requires two specific input files generated by the AERMET pre-processor. AERMET is designed to run as a three-stage processor and operates on three types of data (upper air data, on-site measurements, and the national meteorological database). AERMOD is only capable of running on hourly averaged meteorological data. The meteorological data, in either 5-minute or 10-minute intervals, depending on the case study, were therefore first averaged to hourly data for use in the model.

5.1.2 *Source data requirements*

Wind-blown dust from the two gold TSFs, West Extension (TSF1) and Western Complex (TSF2), and the platinum TSF (TSF7) were modelled as area sources. AERMOD requires the location, dimensions and height of the area source and associated emission rate in g m^{-2} s^{-1}. The model can accommodate temporal varying emissions in the form of an hourly emissions file. This file provides an emission rate for every hour of meteorological data.

Because of the sensitivity of the dust-flux rates to the time intervals (Section 4.6) two modelling approaches were tested:

(i) Quantify hourly dust-flux rates (using sub-hourly wind speed data before averaging the emission rates) and run the model on hourly averaged meteorological data;

(ii) Quantify hourly dust-flux rates (using hourly averaged wind speeds derived from the 5-minute or 10-minute meteorological data) and run the model on hourly averaged meteorological data.

5.2 Case Study 1: Gold Tailings Storage Facilities

5.2.1 Modelling domain

A modelling domain covering 8 km (north-south) by 12 km (east-west) was used with the two TSFs located in the western part of the modelling domain (Figure 43). The modelling domain was divided into a Uniform Cartesian grid resolution of 500 m, with the AngloGold Ashanti monitoring station included as a discrete receptor. To ensure the "recording" of wind-blown dust from the prevailing wind field, the north-western sector, twenty discrete receptors were included at set intervals of approximately 250 m. All receptor heights are automatically set to 1.5 m above ground level (unless specified differently). The AERMOD model simulates ground-level concentrations for each of the receptor grid points.

The topography is characterised by undulating hills ranging from 1 290 to 1320 metres above mean sea level (m amsl). The model was set up to account for the source and receptor elevations and relief of the modelling domain.

5.2.2 Ambient monitoring data

The personnel at AngloGold Ashanti operate a continuous on-line monitoring station, located 1.5 km east-southeast of the West Extension TSF, shown as the EBAM point in Figure 43. The station monitors PM_{10} concentrations in 15-minute intervals and data were available for the period 09 January 2012 12h15 up to 16 August 2012 15h30. The ambient station is located downwind (prevailing wind field is north-northwest and north-west) of the two selected TSFs and deemed suitable for comparing modelled PM_{10} concentrations against the monitored PM_{10} concentrations.

The EBAM is a real-time device using beta rays to determine particle mass concentrations on filter tape according to US EPA requirements. It is used for automated PM_{10}, $PM_{2.5}$ and even TSP measurements. The EBAM can operate at 15-minute intervals and can interface with anemometers and temperature gauges (Ecotech, 2013).

Figure 43: Modelling domain for Case Study 1 Gold Tailings Storage Facilities.

5.2.3 *Meteorological data*

Meteorological data for the period 01 January 2012 to 31 December 2012 were reported on.

Wind roses have been provided for annual – daytime and night-time – averages (Figure 44), together with the wind speed and wind direction frequency (Figure 45).

For the year 2012, the dominant wind field was from the north-northwest, prevalent for 23% of the time. Frequent northerly (9% of the time) and north-westerly (10% of the time) winds were recorded, with infrequent south-westerly and north-easterly winds occurring for less than 5% of the time. Winds from the south-easterly sector occurred for less than 1% of the time. Northerly winds increased during daytime; north-north-westerly winds were more prominent during the night.
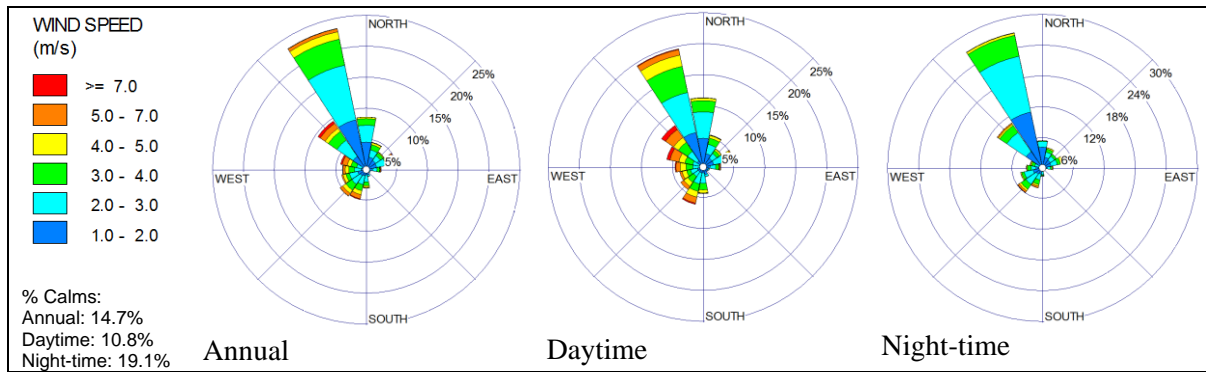
Figure 44:   Annual, daytime and night-time wind roses for 2012.

Dust mobilisation occurs only at wind velocities higher than a threshold value (u^*_t), and is a non-linear function of wind speed (u^*). The wind speed frequency plot provided in Figure 45 shows the percentage of time when the wind speed exceeded certain thresholds.

Wind speeds for the region vary, ranging primarily (58% of the time) between 1 - 3 m s^{-1}. Stronger winds (> 5 m s^{-1}), also associated with dust mobilisation, were recorded for 6% of the time. The maximum hourly average wind speed of 10.8 m s^{-1} was significantly lower than the maximum 5-minute wind speed of 22.9 m s^{-1}. These high wind speeds are mostly associated with winds from the northwest (NW), west-northwest (WNW), west (W) and south-southwest (SSW) (Figure 45).
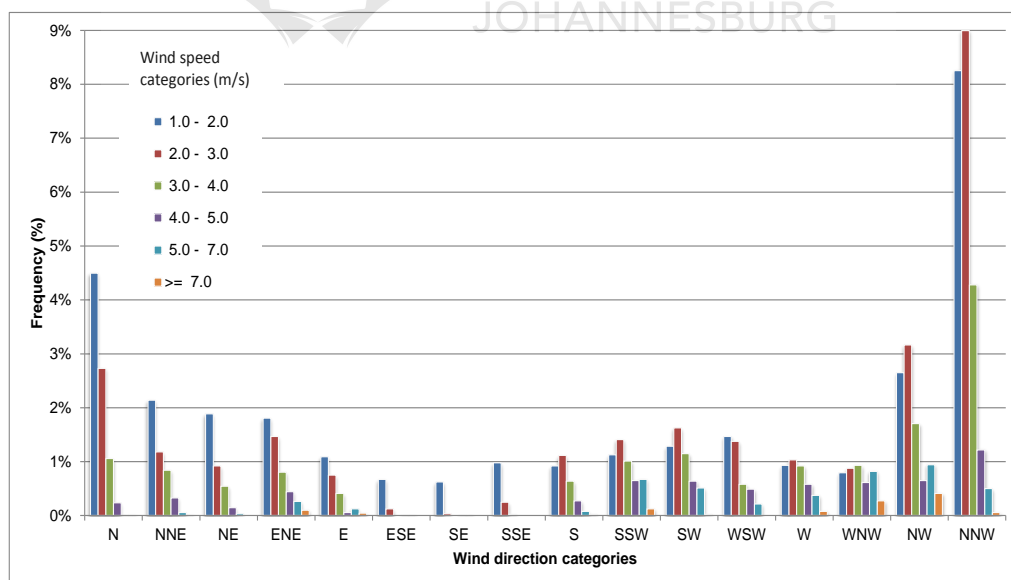
Figure 45:   Wind speed frequencies in relation to wind direction.

Figure 46 shows the relation between wind direction and stability classes for the Klerksdorp meteorological data for the year 2012. Atmospheric stability is dependent on the boundary layer, where unstable daytime conditions normally occur because of turbulence caused by the sun's heating effect on the earth's surface. Night-time conditions are characterised by weak vertical mixing and the predominance of a stable layer.

The highest concentrations from wind dependent ground level, or near-ground level sources, will occur during strong wind speeds and neutral atmospheric conditions (Stability class 4). Neutral conditions are associated with the northerly (N) winds and, to a lesser degree, the east-south-easterly (ESE) winds. Neutral conditions are almost non-existent for the prevailing north-north-westerly (NNW) and north-westerly winds (NW). The stability classes in relation to the wind frequencies are depicted in Figure 46.
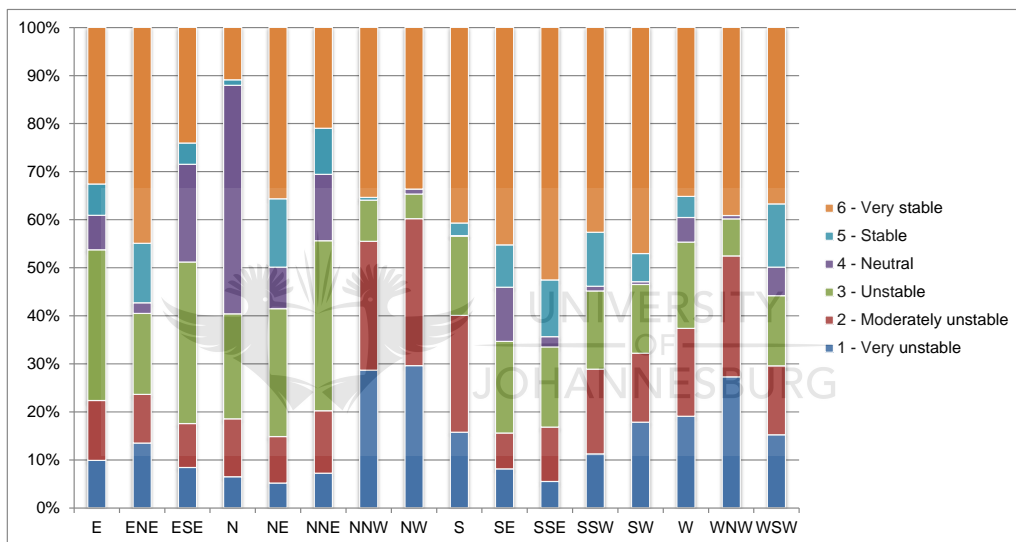
Figure 46:   Stability class and wind direction for the period 2012.

5.2.4   *Emission quantification*

Emission rates from TSF1 (West Extension) and TSF2 (West Complex) were quantified for only the PM_{10} fraction to compare the simulated ground level concentrations with the ambient measured PM_{10} data, and finally to determine the potential for health impacts. Thoracic dust (PM_{10}) is associated with health impacts because it represents particles of a size that can be deposited in, and cause damage to, the lower airways and gas-exchanging portions of the lung. Both the particle size and density determine the residence time in the atmosphere, with coarser and denser particles deposited faster because of gravitation and finer particles remaining suspended for longer (Shao, 2008).

The calculation of emission rates from TSF1 and TSF2, for various wind speeds and stability classes per the 2012 meteorological dataset, was carried out using both the MB95 and SH11

dust-flux schemes according to the approaches set out in Figures 18 and 19, respectively. Emission rates were calculated in two ways:

- Emission rates were calculated using the 5-minute wind velocity data (m s^{-1}) and thereafter averaged to hourly emission rates;

- Hourly emission rates were calculated with hourly averaged wind velocities (m s^{-1}).

5.2.5 *Model validation*

Because of the potential for large dust-flux variation, (Section 4.3.2) it was necessary to validate the modelled results with ambient monitoring data. The approach followed in the model appraisal included the following steps:

(i) PM$_{10}$ concentrations, as recorded at the ambient monitoring station, reflective of wind-blown dust from the two TSFs, would only occur during: (i) periods of high wind speeds exceeding at least 3 m s^{-1}; and (ii) when the wind was blowing from the direction of the two TSFs. Based on this, a wind field of between 240° and 315° was selected as representative of the dust contribution from the two TSFs to the concentrations recorded at the ambient station (Figure 43). Ambient data, recorded when the wind blew from the selected sector at speeds exceeding 3 m s^{-1}, were used for the model validation;

(ii) The 5-minute meteorological dataset for Klerksdorp was averaged to 15-minute intervals to concur with the ambient data for the selected period, and used to calculate representative friction velocities (u^*) using an estimated z_0 as a first approximation;

(iii) The saltation flux (Q) and dust-flux (F) rates were quantified at 15-minute intervals using the MB95 (Figure 17) and SH11 (Figure 18) approaches;

(iv) AERMOD was run with the 15-minute meteorological data and representative emission rates for each time interval. Only the two TSFs were included as sources of emission;

(v) The resultant simulated concentrations at the monitoring station receptor, and the 20 discrete receptors, were compared to the recorded data for the same period. Refine z_0 was refined and steps 2 to 5 were repeated until a good fit with ambient measured PM$_{10}$ data is achieved.

Ambient air quality data

Ambient monitored data from the AngloGold Ashanti EBAM station were used to appraise the dispersion modelling results. Data at 15-minute intervals were only available for seven months of the assessment year, covering the period 09 January 2012 at 12h15 to 16 August 2012 at 15h30.

Figure 47 shows polar plots – produced using the R package for air quality data analysis (Carslaw & Ropkins, 2012) and the Openair version 0.8-0 (Carslaw, 2013) – for the PM_{10} 15-minute concentrations for the period. Figure 47(a) reflects the PM_{10} concentrations from all wind directions, and Figure 47(b) the concentrations from only the selected wind direction sector (240° to 315°) and only when the wind exceeded 3 m s^{-1}. The polar plots imitate recorded PM_{10} concentrations, in relation to the wind direction and wind speed, allowing for easy identification of where main contributing sources may be located and at what wind speeds these source contributions occurred. Figure 47(a) shows the high PM_{10} concentrations (>250 μg m^{-3}) to be emanating from the north-northwest at wind speeds around 10 m s^{-1}, and from another isolated source to the south-southwest, with concentrations of between 200 and 250 μg m^{-3} from the west-northwest. All three source locations indicated PM_{10} contributions under high wind speeds at between 5 and 15 m s^{-1}, indicative of wind dependent sources. The contribution from the west-northwest (Figure 47(b)) was likely to be from the West Extension TSF where the PM_{10} concentrations only occurred under conditions of high wind speeds (10-12 m s^{-1}).

Hourly averaged PM_{10} concentrations from the monitoring station were plotted against hourly averaged wind speeds from the selected wind direction sector (Figure 48). In general, there was no clear correlation between the monitored PM_{10} concentrations and the associated wind speeds, except under conditions of high wind speeds. The wind speed signature was evident in the high PM_{10} concentrations recorded on the 11 August 2012 between 12h00 and 18h00. PM_{10} concentrations ranged between 126 μg m^{-3} and 256 μg m^{-3}, with an average wind speed of 9.8 m s^{-1} over the six hour period. These high velocity winds were predominantly from the northwest, linking the most likely origin of the dust to be the West Extension TSF.
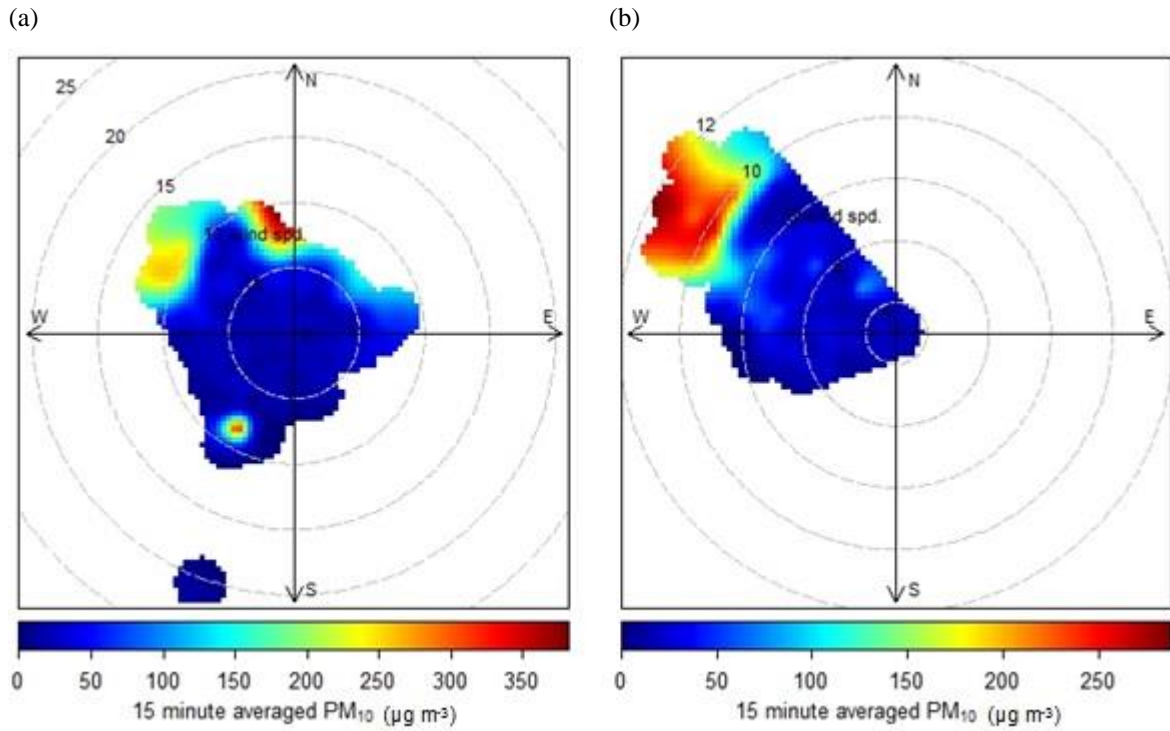
Figure 47: Polar plots reflecting ambient monitored 15-minute PM_{10} concentrations in relation to wind direction and wind speed for the period 09 January 2012 12h15 to 16 August 2012 15h30 from (a) all wind directions and (b) wind direction sector 240° to 315° where wind speeds exceed 3 m s^{-1}.
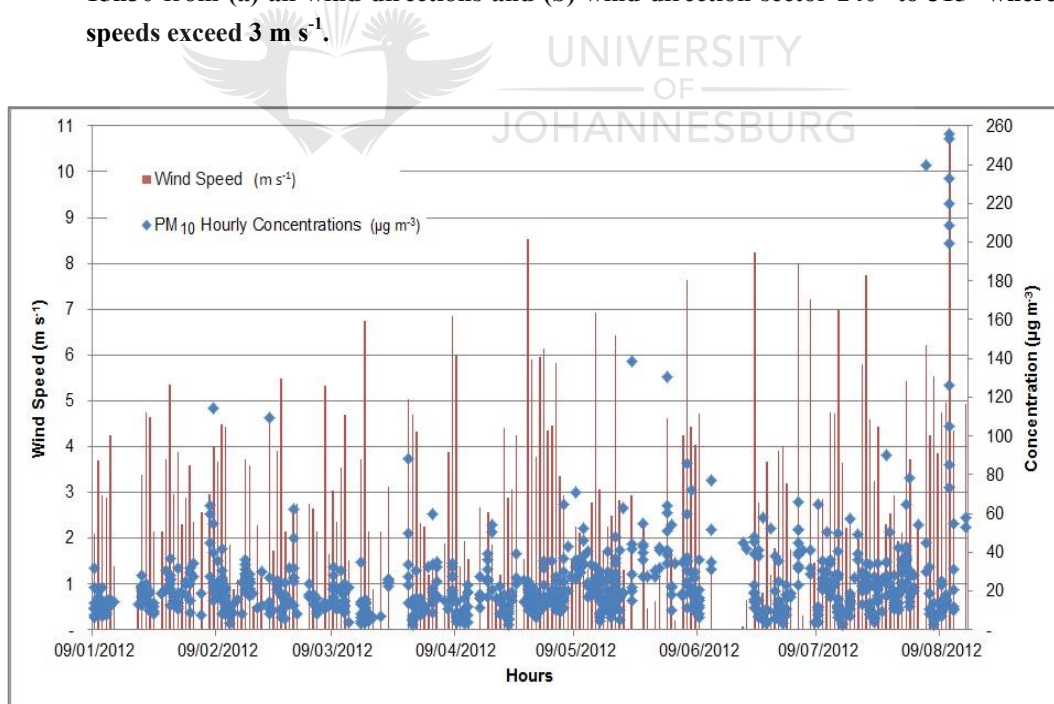
Figure 48: Hourly average PM_{10} concentrations potted against hourly average wind speeds from the west-south-westerly to the north-westerly sector.

Over 24-hour averages, the measured PM_{10} concentrations reflected the same peak concentrations on the 11 August 2012 as the hourly averages. Data for the entire monitoring period, from all the wind directions, are presented in Figure 49. In general, the concentrations were low when compared to the 24-hour South African National Ambient Air Quality Standard (NAAQS) for PM_{10} of 120 µg m^{-3} – this limit is allowed to be exceeded for four days within any one calendar year (i.e. 1% of the time). The red line in Figure 49 represents the more stringent NAAQ limit, which becomes applicable from 01 January 2015. Over the seven-month monitoring period, the 2015 NAAQ limit of 75 µg m^{-3} was exceeded for two days – equating to 1% of the time. Wind-blown dust from the two upwind TSFs, the West Extension and West Complex, were most likely responsible for these exceedances during periods of high wind speeds (both Figure 47 and Figure 48).

The ambient data confirmed the likelihood of wind-blown dust contribution to the recorded PM_{10} concentrations, specifically during periods of high wind speeds, exceeding 3 m s^{-1}, and when the wind was blowing from the west and west-northwest (between 270° and 315°).
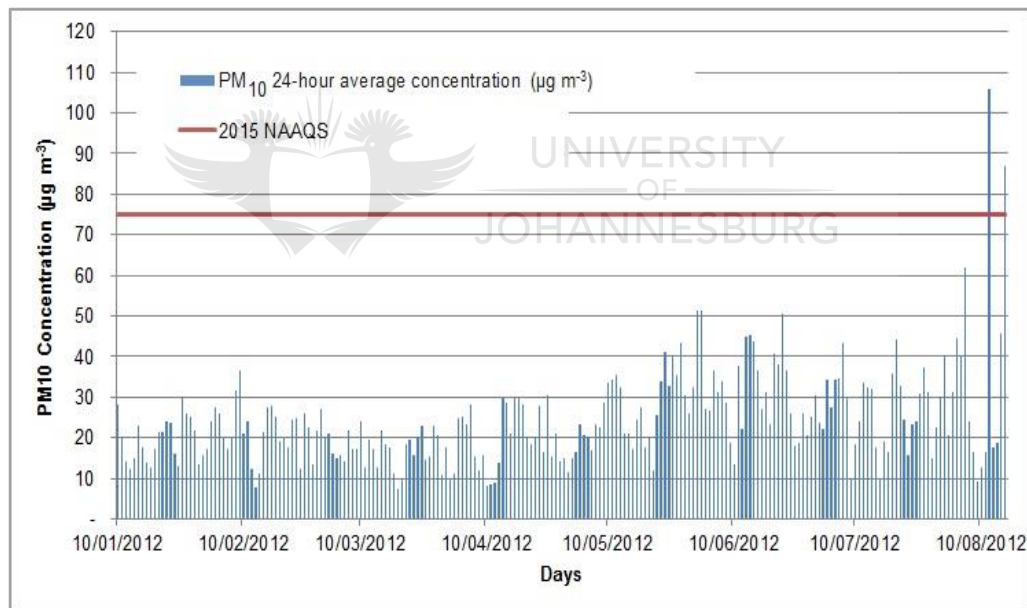
Figure 49: Daily average PM_{10} concentrations shown against the 2015 South African National Ambient Air Quality Limit.

Emission quantification

Friction velocities were estimated using the logarithmic wind speed profile from the 2012 meteorological data, recorded at a reference anemometer height of 10 m. The US EPA assumes a typical roughness height (z_0) of 0.005 m for open terrain, and is restricted to large relatively flat piles or exposed areas with little penetration into the surface layer (US EPA, 2006). In this study, a z_0 of 0.0032 m was found to provide a good fit with measured data as demonstrated in Section 5.2.6. This roughness length is representative of *"thin short grass"* according to the

summary of different surface configuration categories reported by Burger (1986). Tailings storage facilities typically have areas, specifically on the side walls, where vegetation is partially or fully established – either through natural vegetation encroachment or as part of the mine's mitigation programme. From the image provided in Figure 12, it is evident that both TSF1 (West Complex) and TSF2 (West Extension) have areas of vegetation on the surface and side walls. A z_0 of 0.0032 m was therefore regarded representative of the TSFs under investigation.

As mentioned before, the wind friction velocity (u^*) needed to exceed the threshold friction velocity (u^*_t) to initiate particle motion. The threshold friction velocity was calculated using Equation 2, which accounts for neutral, stable and unstable logarithmic wind speed profiles. The threshold friction velocity (u^*_t) was calculated for the PM_{10} size fraction using the source parameters (Table 11), resulting in a u^*_t of 0.58 m s^{-1}. When accounting for the effect from moisture content in the source material – in this case 0.20% – through the application of Equation 6, the u^*_t increased to 0.67 m s^{-1} thus reducing the saltation flux by 4.6 times. The moisture content represented the average for samples taken from various portions of the TSF: beach area, crest and slope, and those areas not regarded as representative of evaporation losses from the exposed surface layer susceptible to wind erosion. When accounting for drag partitioning (R), u^*_t increased to 1.66 m s^{-1}, demanding a z_0 of at least 0.24 m to result in positive saltation flux rates. These saltation flux rates were 100 times higher when compared with the saltation flux calculated without R and using a z_0 of 0.0032 m. A z_0 of 0.24 m was representative of *"...fully grown root crops or scrubs..."* (Burger, 1986) and not regarded as characteristic of the TSFs' surface conditions.

For the model appraisal, saltation flux rates based on a 15-minute interval were calculated with z_0 set at 0.0032 m and only the effect from moisture was taken into account. These saltation flux rates were then applied to the dust-flux scheme of MB95 and SH11, following the approaches outlined in Figure 17 and Figure 18, respectively.

The same parameters as reported in Table 11 were used. The SH11 resulted, as did the evaluation under Section 4.3, averages five times higher for dust-flux rates than the MB95 approach. The 15-minute interval emission rates were exported into the format required by AERMOD. Since the model cannot accommodate meteorological data intervals of less than 1-hour, the 15-minute intervals were presented as hourly averages.

Dispersion modelling results validation

Concentrations from the AngloGold ambient station, included as a sensitive receptor in the model, and the 20 discrete receptors, were extracted for the highest "hourly" concentrations (which were in fact averaged 15-minute concentrations). The modelled versus measured results were then compared for the 100th, 99th, 97th, 95th and 90th percentiles.

The results in Table 21 show a good correlation between modelled and measured data on the 99th percentile, with a z_0 of 0.0032 m. The modelled 99th percentile PM_{10} concentration at the monitoring station was 17% lower than the measured concentration; however the 99th percentile concentration from the 20 discrete receptors provided a perfect fit at 100%. The ambient monitoring station reported only a single modelled concentration of 119 µg m^{-3} for one 15-minute time interval, resulting in the same concentration for all five percentiles. This exception may be attributed to the inability of Gaussian plume models to be spatially representative for a single point. The predicted concentrations at the discrete receptors placed around the ambient station, have been regarded as more representative. The disparity between measured and modelled concentrations increased at lower percentiles.

The model validation was done with the emissions from the MB95 dust-flux scheme where the SH11 dust-flux scheme resulted in an over-prediction when compared with the measured data. With the minimally disturbed dust correction factor ($CF\eta_{mi}$) applied to the SH11 scheme (Section 4), similar averaged emission rates resulted, providing a correlation of 0.97 (West Complex TSF) and 0.92 (West Extension TSF) with the MB95 dust-flux rates.

Table 21: **Comparison of 15-minute recorded and predicted PM_{10} concentrations for the period 09 January 2012 12h15 up to 16 August 2012 15h30 for winds from the 240° to 315° sector with z_0 set at 0.0032 m.**

Percentile	Recorded PM_{10} Concentrations	Predicted at Ambient Station	Predicted at 20 receptors	Predicted at Ambient Station / Recorded	Predicted at 20 receptors / Recorded
	(µg m^{-3})	(µg m^{-3})	(µg m^{-3})	(%)	(%)
100	452	119	146	26%	32%
99	146	119	145	82%	100%
97	71	119	144	167%	201%
95	56	119	143	211%	253%
90	42	119	134	286%	322%

5.2.6 Dispersion model and results

Emission rates, using both MB95 and the SH11 dust-flux schemes, were quantified with the 5-minute meteorological data for 2012, before being averaged to hourly emission rates. Similarly, emissions were calculated based on hourly averaged wind field data. Both approaches use a z_0 of 0.0032 m as determined through the model appraisal.

The hourly averaged emissions rates, based on 5-minute meteorological data, ranged between 5.69E-06 and 6.58E-06 g m^{-2} s^{-1} (Table 22). This was with the correction factor, $CF\eta_{mi}$, applied to the SH11 dust-flux scheme. The total annual emissions calculated for the two TSFs (Table 22) were 150 tpa and 821 tpa based on the MB95 scheme, and 145 tpa and 753 tpa based on the SH11 scheme.

For the hourly averaged meteorological data, the maximum threshold velocities (u^*) were below the threshold friction velocity (u^*_t) of 0.68 m s^{-1}, resulting in no saltation flux rates (Q) or dust-flux rates (F). Only by increasing z_0 to 0.0071 m, was it possible for any saltation flux and resulting dust-flux rates to be obtained. The average emission rates and total tons per annum based on the increased z_0 are provided in Table 22.

Dust flux rates in relation to the influencing wind speed are shown in Figure 50. With no hourly emissions resulting from the hourly averaged data, using the selected z_0 of 0.0032 m, the hourly averaged 5-minute emission rates are shown. Dust flux rates (F) occurred for wind speeds in excess of 3 m s^{-1}. When the 5-minute data was evaluated, it showed that the u^*_t of 0.67 m s^{-1} equated to a wind speed of 8.8 m s^{-1}, thus indicating wind erosion only occurred under conditions of high wind speeds. Only 12 hours of the year had sufficiently high wind speeds to generate emissions.

The variations between the MB95 and SH11 dust-flux rates are also clearly demonstrated in the Figure 50. Because of the correction factor applied to the SH11 scheme, the difference was negligible. Dust mobilisation occurred for wind speeds above 3 m s^{-1}, with most dust emissions when winds were above 6.7 m s^{-1}.

Modelled results are provided in Figure 51 for second highest hourly; second highest daily and period averaged PM$_{10}$ ground level concentrations based on 5-minute hourly averaged emissions, as calculated by the two dust-flux schemes. Even with a different z_0 applied to the hourly data, no concentrations for the second highest hourly and daily averages have been produced.

Table 22: Average and total emission rates for the MB95 and SH dust-flux schemes derived from different temporal varying wind speed data.

Source	Source Code	Area (m²)	Hourly average emission rate (g m⁻² s⁻¹) [a]		5-minute emission rates averaged to hourly (g m⁻² s⁻¹)	
			MB95	SH11	MB95	SH11
West Extension	TSF1	805 182	1.44E-07	1.37E-07	5.87E-06	5.69E-06
West Complex	TSF2	3 948 493	1.61E-07	1.47E-07	6.58E-06	6.03E-06
			Total hourly average emissions (tpa) [a]		Total 5-minute emissions (tpa)	
West Extension	TSF1		3.5	3.7	150	145
West Complex	TSF2		18.4	20.1	821	753

Notes: [a] based on a z_0 of 0.0071 m.
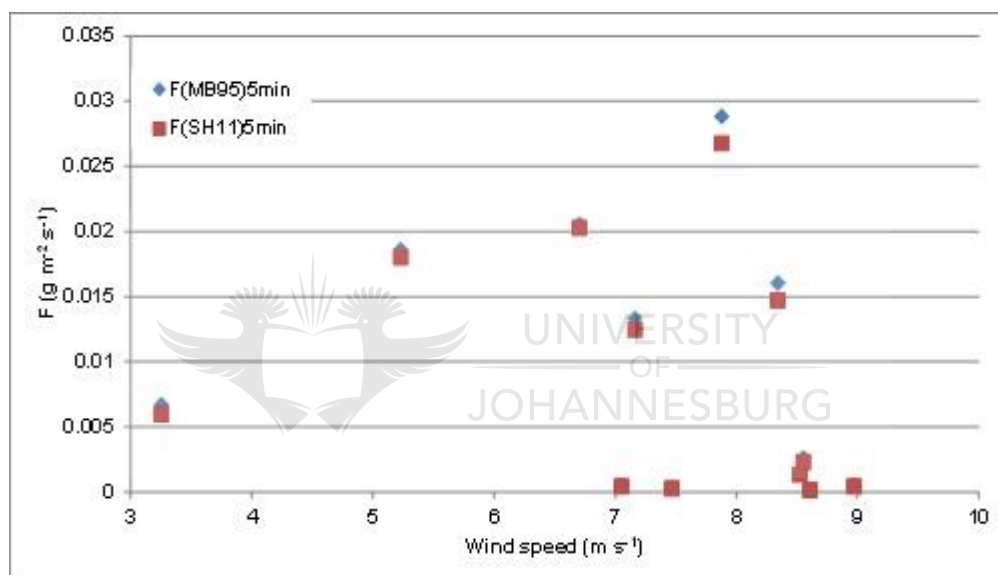
Figure 50: Scatter plot of hourly dust-flux rates (F) versus hourly wind speed (m s⁻¹).

The predicted ground level concentrations were very similar between the two dust-flux schemes of MB95 and SH11, showing only small spatial variation over the three averaging periods. Hourly and daily average concentrations displayed higher variability in the spatial extent with the MB95 concentrations stretching further east. On average, the magnitude of the MB95 simulated concentrations was slightly higher than the SH11 concentrations, for all three averaging periods (hourly, daily and annual). The relation between source strengths and the impacting concentrations was not linear, showing a less significant difference in concentrations than for the emissions.

Highest hourly average PM$_{10}$ concentrations

Contours represent:

500 µg m^{-3}

▢ MB95 5-min hourly emissions
▢ SH11 5-min hourly emissions

Highest 24-hour average PM$_{10}$ concentrations

Contours represent:

75 µg m^{-3}

▢ MB95 5-min hourly emissions
▢ SH11 5-min hourly emissions

Period average PM$_{10}$ concentrations

Contours represent:

40 µg m^{-3}

▢ MB95 5-min hourly emissions
▢ SH11 5-min hourly emissions

Figure 51: Second highest- hourly, 24-hourly and period averaged PM$_{10}$ ground level concentrations from 5-minute hourly emissions for the MB95 and SH11 dust-flux schemes.

5.3   Case Study 2 Platinum Tailings Storage Facility

5.3.1   Modelling domain

The Impala Platinum TSF Case Study 2 was modelled for an area of 13 km (north-south) by 17 km (east-west) with the active tailings storage facility – called No. 2 Tailings – in the centre of the modelling domain (Figure 52). As with Case Study 1, a 500 m uniform Cartesian grid was applied to the modelling domain, with the Impala Platinum Luka monitoring station included as a discrete receptor. In addition to the monitoring station, 10 discrete receptor points were included in a north-south direction alongside the monitoring station location. These receptors were used for the model appraisal and to determine a suitable roughness length (z_0) for the wind erosion schemes.

The topography surrounding the Impala Platinum Mine is complex, with the Magaliesberg mountains 9 km to the west and southwest and 16 km to the south. The relief of this mountain range varies between 1 257 meters above mean sea level (m amsl) in the west to 1 500 m amsl in the south. The topography in the immediate vicinity of the No. 2 TSF is, however, fairly flat with undulating hills, ranging from approximately 1 100 m amsl in the north-east to 1 500 m amsl in the south.
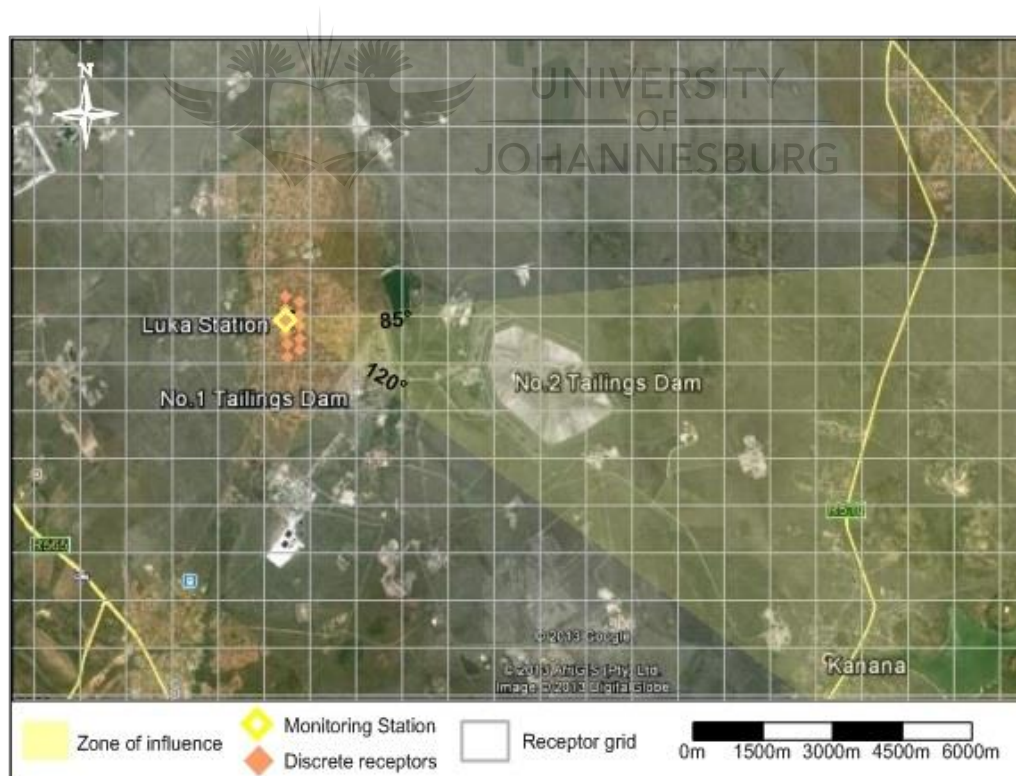
Figure 52:   Modelling domain for Case Study 2 Platinum Tailings Storage Facility.

5.3.2 Ambient monitoring data

Impala Platinum operates a continuous ambient monitoring station at the Ga-Luka Village, located 4 km to the west-northwest of the TSF (Figure 52). PM_{10} concentrations are recorded at 10-minute intervals, together with meteorological parameters (wind speed, wind direction, temperature and relative humidity. Data for the calendar years 2009 and 2010 were made available by Impala Platinum for use in this study.

5.3.3 Meteorological data

Meteorological data recorded at the Impala Luka station for the period 01 January 2009 to 31 December 2010 are reported on.

Period-, daytime and night-time wind roses are provided in Figure 53, indicating prevailing winds are from the east-northeast to south-southwest, with 20% calm conditions, on average. During the day, winds more frequently occur from the east-northeast and east with infrequent high velocity winds from the west-northwest. Night-time conditions are characterised by low velocity winds from the southern sector and an increase in the percentage calm conditions (22.6%). The wind field at the Luka monitoring station reflects almost no winds from the north-northeast to north-northwest.
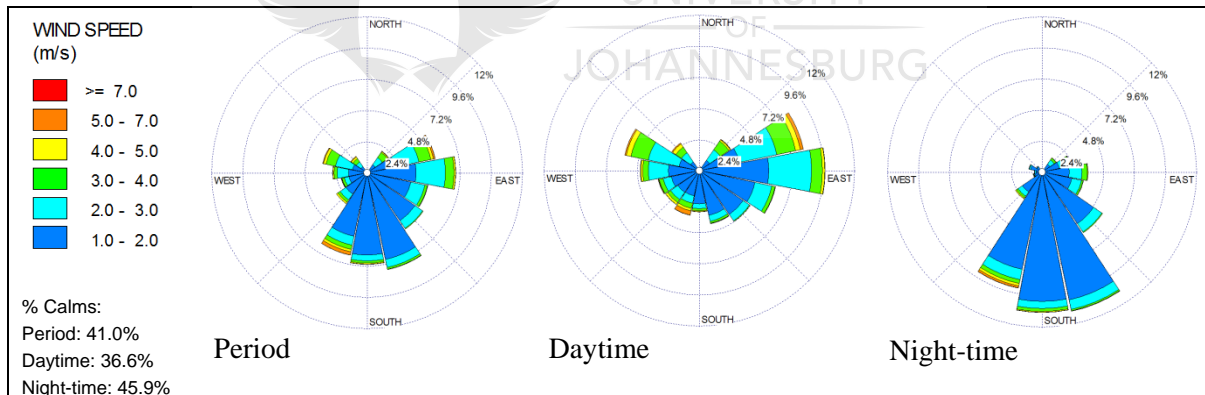
Figure 53: Period, daytime and night-time wind roses for the period 2009 to 2010.

The frequency plot, showing the number of time wind speeds exceed a certain threshold, is provided in Figure 54. Low velocity winds – of less than the range of 1 - 3 m s^{-1} – occurred for 66% of the time and were mostly from the southern wind field sector. Stronger winds, between 4 - 5 m s^{-1}, occurred for only 1% of the time; winds in excess of 5 m s^{-1} for less than 1%. This is reflective of the hourly averaged wind speeds at the station, with a maximum of 7.8 m s^{-1} having been reported. This is in comparison with the 10-minute wind speeds, which showed a maximum of 10.25 m s^{-1}. The higher wind speeds are primarily from the north-northeast (NNE), east-northeast (ENE), with less frequent occurrences from the east (E).
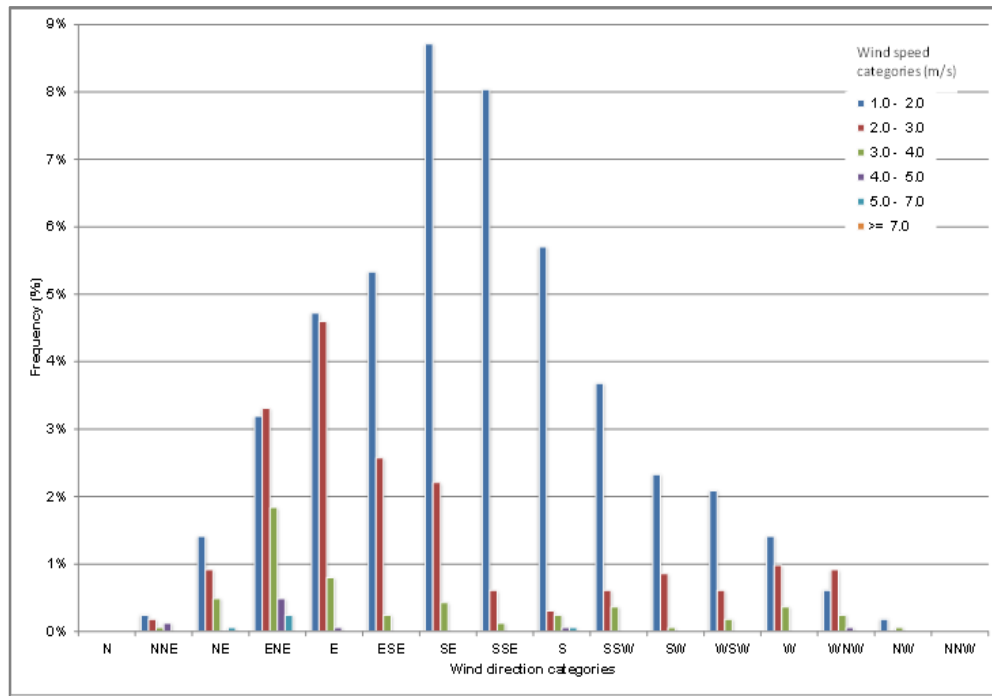
Figure 54: Wind speed frequencies in relation to wind direction for the Luka Station (2009 – 2010).

The relation between wind direction and stability classes for the Luka meteorological data for the year 2009 to 2010 is provided in Figure 55. Neutral atmospheric conditions, favourable for wind dependent emissions, occurred for only a few hours during the two-year period (less than 1%). When neutral conditions occurred it was mainly from the south-southwest (SSW), the east-northeast (ENE) and, to a lesser extent, the northeast (NE) and the west-northwest (WNW).

Stable conditions occurred more frequently, for 12% of the time, and were mainly associated with the easterly flow and the south-westerly flow. Very unstable conditions dominate, occurring for 20% of the time, and are mostly associated with southerly airflow.

The probability for wind erosion in this area is slight because of the general low velocity winds and few neutral conditions.
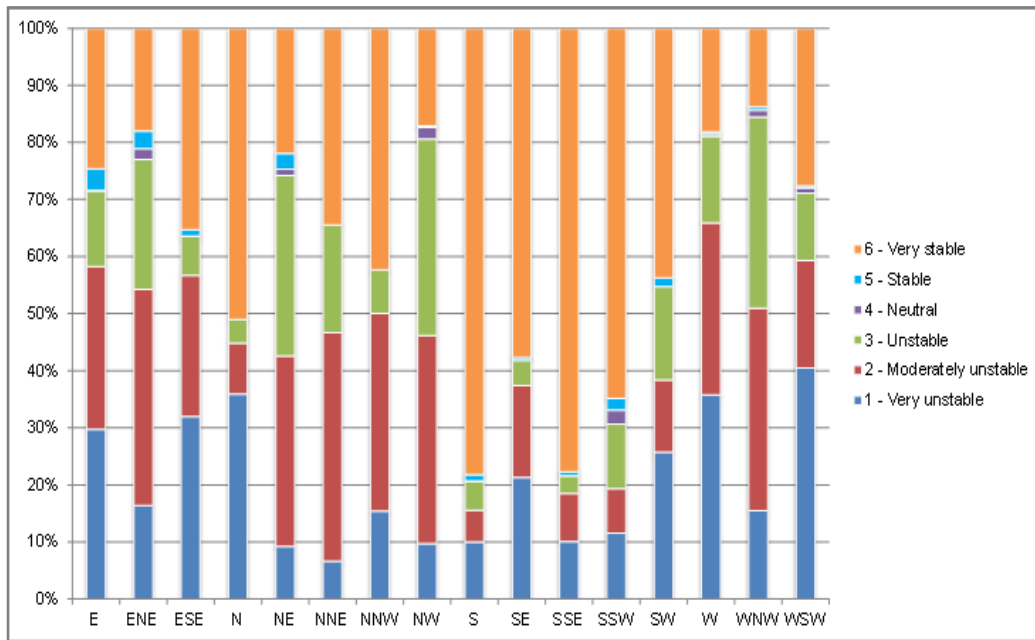
Figure 55: Stability class and wind direction for the Luka Station (2009 – 2010).

5.3.4 Emission quantification

The same methodology as applied in Case Study 1, was used for Case Study 2 where only the PM_{10} fraction was quantified, using both the MB95 and the SH11 dust-flux schemes. Emission rates were quantified only for the No. 2 TSF, because the dormant No. 1 TSF is fully vegetated (Figure 14) and unlikely to contribute to the ambient dust concentrations at the monitoring station.

The calculation of emission rates from the No. 2 TSF for various wind speeds and stability classes, per the 2009 to 2010 meteorological dataset, was carried out, using both the MB95 and SH11 dust-flux schemes according to the approaches set out in Figures 17 and 18, respectively. The emission rates were calculated in two ways:

- Emission rates were calculated using the 10-minute wind velocity data (m s^{-1}) and thereafter averaged to hourly emission rates;

- Hourly emission rates were calculated with hourly averaged wind velocities (m s^{-1}).

5.3.5 Model validation

The same approach as outlined under Section 5.2.5 was followed with the only differences being the averaging period of the meteorological data and the influencing wind directions:

- The influencing wind field sector from the No. 2 TSF on the ambient station at Luka was between 85° and 120° (Figure 52). Ambient and wind field data at 10-minute intervals, recorded when the wind blew from this sector at speeds exceeding 3 m s^{-1}, were used for the model validation.

Ambient monitored data from the Luka station for the two-year period (01 January 2009 – 31 December 2010) were used for the model appraisal.

Polar plots (Carslaw & Ropkins, 2012; Carslaw, 2013) for the 10-minute PM_{10} concentrations are provided in Figure 56(a) for all wind directions and in Figure 56(b) for the selected wind field – i.e. between 85° and 120°, and where the wind speeds exceeded 3 m s^{-1}. From Figure 56(a), it can be argued that there numerous sources surrounding the Luka station were contributing to the measured PM_{10} concentrations. Most of these sources seemed to be wind dependent, at wind speeds of between 5 and 10 m s^{-1}. However, there were also signs of wind independent sources contributing at lower wind speeds. The higher concentrations – above 200 µg m^{-3} – shown to the east-southeast of the station may have been because of wind erosion from the No. 2 TSF. This is confirmed in Figure 56(b), where the higher PM_{10} concentrations (>600 µg m^{-3}) are shown to come from the east-southeast, at wind speeds between 5.5 and 6 m s^{-1}.

(a)   (b)
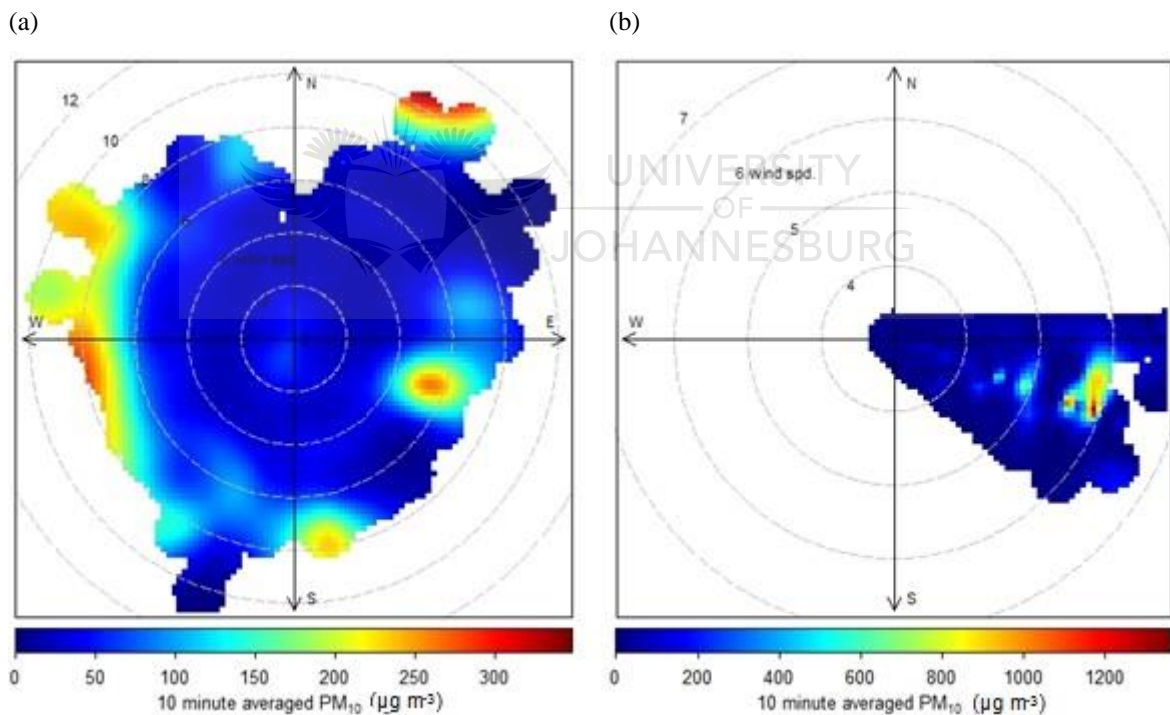
Figure 56: **Polar plots reflecting ambient monitored 10-minute PM_{10} concentrations in relation to wind direction and wind speed for the period of 01 January 2009 00h00 to 31 December 2010 23h50 from (a) all wind directions and (b) only wind direction sector 85° to 120° with wind speeds exceeding 3 m s^{-1}.**

Hourly averaged PM_{10} concentrations from the monitoring station were plotted against hourly averaged wind speeds for winds from the selected sector in Figure 57. The correlation between wind speed and PM_{10} concentrations was not clear, with a few high concentrations reflected at high wind speeds of more than 5 m s^{-1}. The highest measured PM_{10} concentrations

occurred under conditions of both low (below 2 m s^{-1}) and high wind speeds (above 5 m s^{-1}), indicating a combination of source types contributing to the ambient measured data. The concentrations under high wind speeds are likely to be from wind dependent sources – such as wind-blown dust from TSFs – whereas the high concentrations under low winds speeds could be a result of localised, wind independent dust generating sources. The two highest concentrations of 814 µg m^{-3} (on 23 February 2009 at 16h00) and 1 031 µg m^{-3} (on 08 June 2009 at 21h00), both occurred under conditions where the wind speed exceeded 5 m s^{-1} and can be linked to wind dependent emission sources (as indicated by the polar plots).
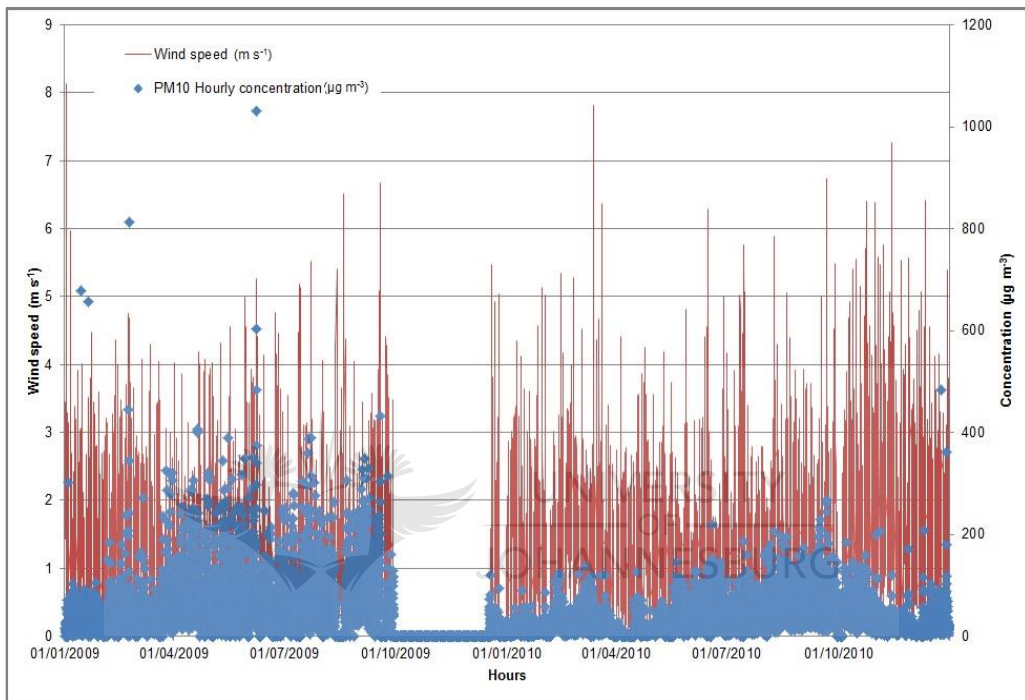
Figure 57: **Hourly average PM$_{10}$ concentrations potted against hourly average wind speeds from the east-north-easterly to the south-easterly sector.**

On a daily average, the PM$_{10}$ concentrations provided in Figure 58, showed higher levels during 2009 than in 2010. During 2009, the current NAAQ limit of 120 µg m^{-3} was exceeded for 7 days; the 2015 NAAQ limit of 75 µg m^{-3} was exceeded for 81 days. The highest daily concentration recorded in 2009 was 215 µg m^{-3}. A distinct decrease in PM$_{10}$ concentrations was observed at the Luka station from 2009 to 2010 (Figure 58). During 2010, the 2015 NAAQ limit of 75 µg m^{-3} was exceeded for a total of 5 days, with no exceedances of the current NAAQ limit recorded. The highest daily average PM$_{10}$ concentration for 2010 was 97 µg m^{-3}.
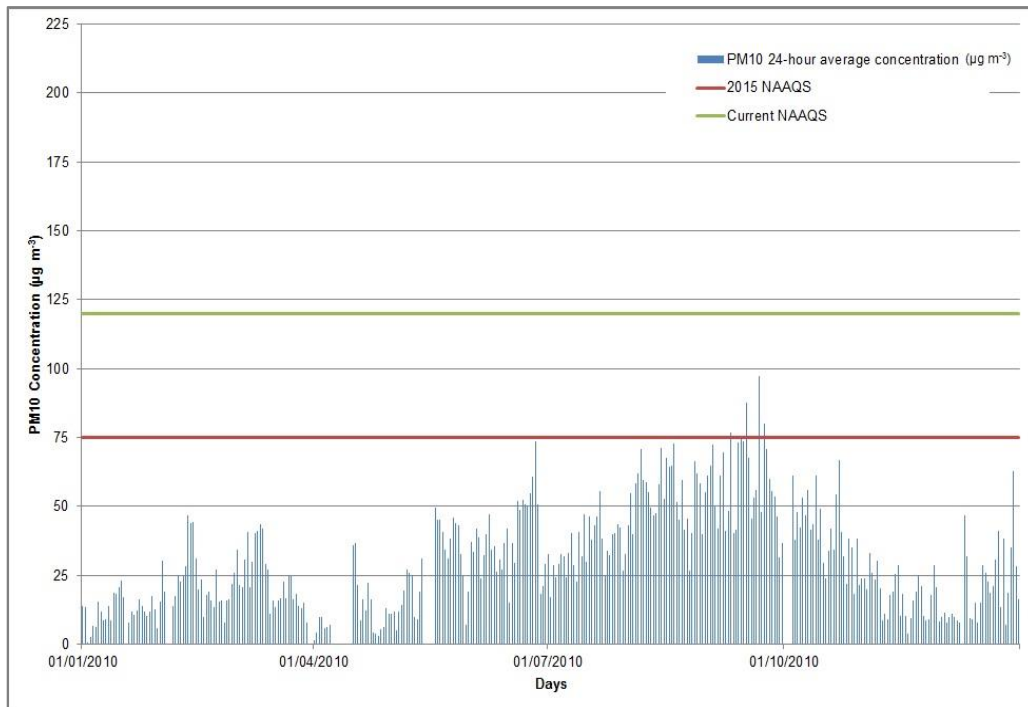
Figure 58: Daily average PM$_{10}$ concentrations shown against the 2015 South African National Ambient Air Quality Limit.

Emission quantification

For the platinum tailings, a z_0 of 0.0061 m provided a good fit with measured data. This roughness length falls within the category*: "...thin cut grass..."* (Burger, 1986) and is regarded representative of the surface and side wall conditions at the Impala No. 2 TSF.

The PM$_{10}$ size fraction threshold friction velocity (u^*_t) was based on the source parameters listed in Table 11:   Selected input parameters from the gold TSFs for the various dust emission schemes. Table 14, shows the results of u^*_t of 0.58 m s^{-1}. By accounting for the moisture content of 0.22% in the tailings material, the u^*_t increased to 0.76 m s^{-1} – which is much higher than the u^*_t of 0.67 m s^{-1} for the gold tailings as reported for Case Study 1. This moisture content resulted in no saltation flux rates, with all the friction velocities (u^*) falling below the u^*_t. Similar to Case Study 1, when accounting for the effect of drag partitioning (R), u^*_t increased even further to 2.48 m s^{-1} – again resulting in no saltation flux rates. For the purpose of the No. 2 TSF, no moisture nor roughness length corrections were made to u^*_t.

The 10-minute data from the wind direction sector of between 85° and 120° were used to calculate the saltation flux rates and the dust-flux rates from both MB95 and SH11 schemes, using the parameters as reported in Table 14.

As expected, the dust-flux rates from the SH11 scheme produced much higher emissions; i.e. 17 times higher, than the MB95 rates. For the purpose of model appraisal, only emissions from the MB95 dust-flux scheme were used. The averaged 10-minute interval emission rates were exported into the format required by AERMOD and modelled as hourly averages.

Dispersion modelling results validation

The Luka monitoring station was included as a separate receptor point in the model. Data from this station, together with the 10 discrete receptors points around the station, were used to validate the model results. The modelled results were compared for the 100th, 99th, 97th, 95th and 90th percentiles and are reported in Table 23. The first approximation z_0 was changed until a good fit with measured data was found.

In the case of the No. 2 TSF, a good correlation between modelled and measured data was found at the 100th percentile – i.e. with the highest 10-minute concentration. A z_0 of 0.0061 m provided the best fit, where comparison between modelled PM_{10} concentrations and measured data at the Luka station resulted in a 99% correlation. For the 10 discrete receptors, the modelled data over-predicted by 36%. This fell within the uncertainty range of the model at between -50% and 200% and was deemed acceptable.

With the SH11 dust-flux scheme resulting in even larger over-predictions, falling outside the model uncertainty range, the correction factor ($CF\eta_{mi}$) was applied. This resulted in significantly lower emissions, which, on average, were only 3.8 times higher than the emissions from the MB95 dust-flux scheme.

Table 23: **Comparison of 10-minute measured and modelled PM_{10} concentrations for the period 01 January 2009 to 31 December 2010 for winds from the 85° to 120° sector with z_0 set at 0.0061 m.**

Percentile	Recorded PM_{10} Concentrations	Predicted at Ambient Station	Predicted at 20 receptors	Predicted at Ambient Station / Recorded	Predicted at 20 receptors / Recorded
	(µg m⁻³)	(µg m⁻³)	(µg m⁻³)	(%)	(%)
100	**2 078**	**2 058**	**2 817**	**99%**	**136%**
99	217	2 055	2 799	949%	1292%
97	145	2 049	2 755	1415%	1902%
95	118	2 044	2 599	1733%	2204%
90	87	2 030	2 346	2338%	2703%

5.3.6   Dispersion model and results

For the purpose of dispersion modelling exercise, only the 2010 meteorological data were used. Emission rates were quantified for both the MB95 and the SH11 dust-flux schemes, based on both 10-minute wind field data and hourly averaged wind field data. Both approaches used a z_0 of 0.0061 m as determined through the model appraisal.

The 10-minute emission rates, converted to hourly averages, were 4.80E-07 g m^{-2} s^{-1} and 1.87E-06 g m^{-2} s^{-1} (from the MB95 and SH11 (as corrected), respectively) (Table 24). The total annual emissions were 101 tpa from the MB95 scheme, and 394 tpa from the SH11 scheme. These rates were slightly higher when compared with the hourly average emission rates and tonnages (Table 24). Calculating the emissions from hourly averaged wind speed data resulted in an underestimation of 3% for both the MB95 and SH11 approaches.

The dust-flux rates in relation to the influencing wind speeds are shown in Figure 59. In the case of the No. 2 TSF, the 10-minute averaged to hourly emission rates are shown for much lower wind speeds; i.e. at 1.9 m s^{-1}, whereas the hourly-derived emission rates only started at 2.6 m s^{-1}. Interestingly, the hourly emission rates from the SH11 dust-flux scheme, F (SH11) hour, reflected much higher single emission rates than the 10-minute derived emission rates. The 10-minute emissions rates were, however, for 29 hours of the year whereas the hourly emission rates were for only 5 hours. The hours resulting in emissions were also different between the two approaches, with only one hour shared.

The variation between the MB95 and SH11 dust-flux rates are clearly demonstrated in the Figure 59. Because of the correction factor applied to the SH11 scheme, the difference was only high for the hourly-derived emission rates.

The modelled results, as provided in Figure 60, show the second highest hourly, daily and annual average PM$_{10}$ concentrations from both modelling approaches.

The predicted ground level concentrations were spatially significantly different between the MB95 and SH11 approaches, with the impact zone from the MB95 approach much smaller than the SH11 approach. This was true for all three averaging periods and is a direct result of the variation in the hourly emission rates (Figure 59), where the SH11 emissions were, on average, higher. Hourly and daily average concentrations displayed higher variability in the spatial extent, with a decrease in the variation over the long-term averages. Dust mobilisation occurred at wind speeds of 1.9 m s^{-1} but, with most emission rates, at wind speeds above 2.5 m s^{-1}.

The difference between the 10-minute averaged and the hourly-derived emissions was specifically evident in the SH11 approach, where the 10-minute concentrations resulted in a much larger spatial extent than the hourly concentrations (Figure 60). Thus, even though the hourly-derived emissions resulted in higher maximum emission rates (Figure 59), the 10-minute averaged emission rates were for more hours and, on average, higher, resulting in higher ground level concentrations (Figure 60).

The 10-minute emissions, in comparison with the hourly-derived emissions, resulted, on average, in 40% higher modelled hourly concentrations, and up to double the percentage of the annual averaged concentrations.
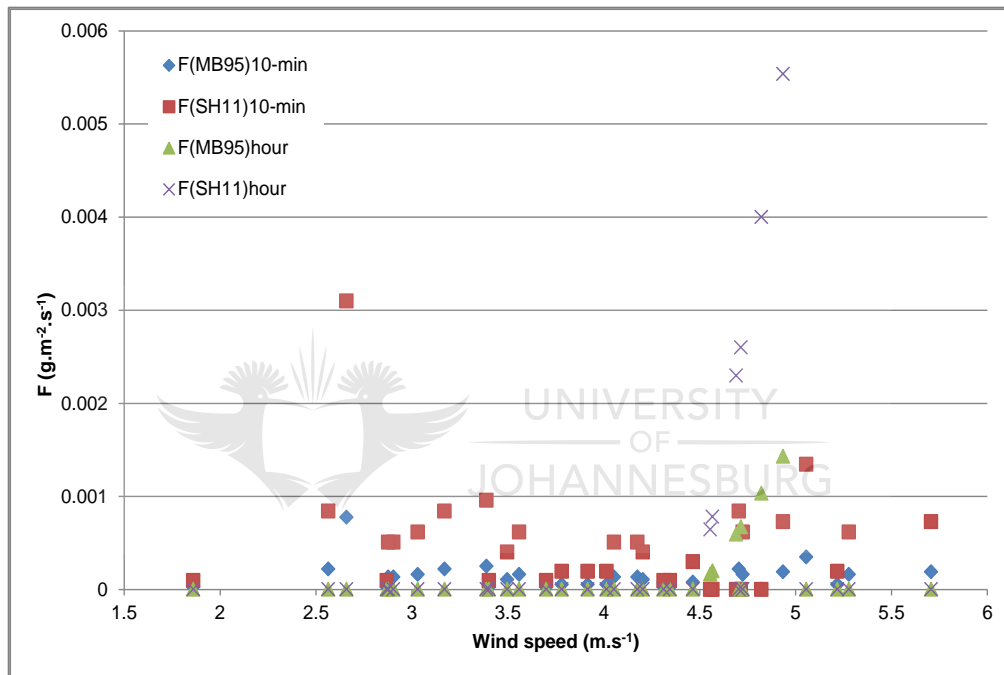
Figure 59: Scatter plot of hourly dust-flux rates (F) versus hourly wind speed (m s^{-1}) from 10-minute and hourly averaged data.

Table 24: Averaged and total emission rates for the MB95 and SH dust-flux schemes derived from different temporal varying wind speed data.

Source	Source Code	Area (m²)	Hourly average emission rate (g m⁻² s⁻¹)		10-minute emission rates averaged to hourly (g m⁻² s⁻¹)	
			MB95	SH11	MB95	SH11
No. 2 TSF	TSF7	6 688 084	4.67E-07	1.81E-06	4.80E-07	1.87E-06
			Total hourly average emissions (tpa)		Total 10-minute emissions (tpa)	
			MB95	SH11	MB95	SH11
			98.5	381.7	101.2	394.1
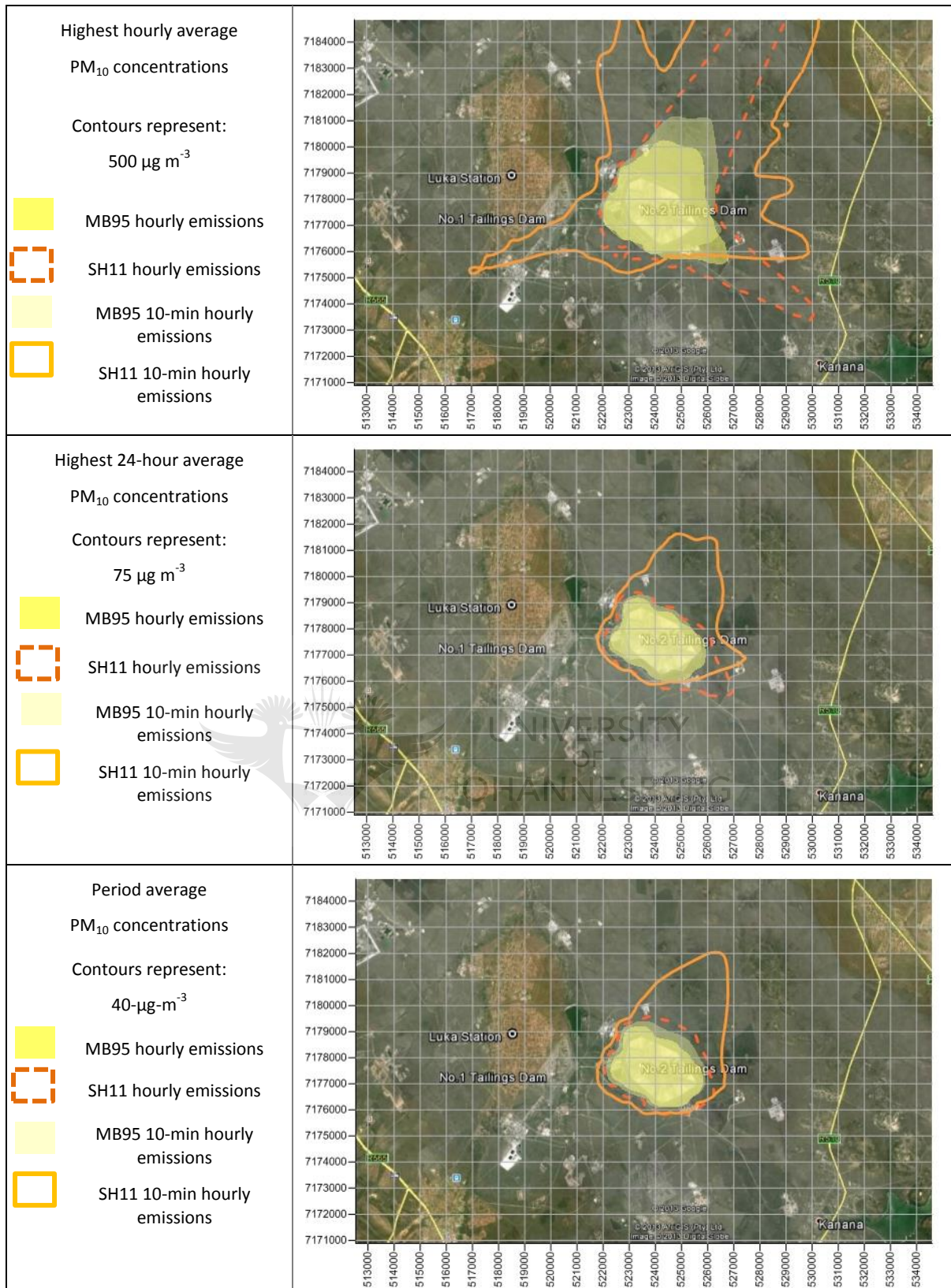
Figure 60: Hourly, 24-hourly and period averaged PM$_{10}$ ground level concentrations from hourly emissions and 10-minute hourly emissions for the MB95 and SH11 dust-flux schemes.

5.4   Discussion

Case Study 1 showed a better correlation between modelled and measured data. Firstly, the ambient monitoring station in Case Study 1 is located only 1.5 km downwind from the two TSFs assessed, and the highest wind speeds were recorded from this direction. In Case Study 2, the ambient monitoring station is located 4 km away and not in the direction of the dominant high velocity winds.

Case Study 1 showed a larger variation between 5-minute wind speeds and hourly averaged wind speeds. The highest hourly wind speed of 22.9 m s^{-1} would result in significantly different emission strengths than the hourly averaged wind speed of 10.8 m s^{-1}. The meteorological data in Case Study 2, on the other hand, had very little variation between the maximum 10-minute wind speed of 10.3 m s^{-1}, and the maximum hourly averaged wind speed of 7.8 m s^{-1}. Emissions derived from the 5-minute data, before being averaged to hourly emissions, proved to be vastly different from the hourly emission rates, where no emissions resulted from the hourly averaged meteorological data. In Case Study 2, the difference between the 10-minute emission rates and the hourly emission rates were not as great mainly because of the slighter variations in maximum hourly wind speeds and 10-minute wind speeds.

Polar plots, as derived from the Openair Freeware, proved to be a useful tool for identifying the main contributing sources with the measured ambient concentrations. From Case Study 1, the contribution from the Western Extension TSF was clearly signalled and confirmed when data from only the influencing wind direction were extracted. The high wind speeds at which the contributions occurred is characteristic of wind dependent sources of emissions. For Case Study 2, the wind dependent emission sources were not clear, with the ambient data showing influences from non-wind dependent emission sources. This has made the model appraisal more difficult since the contribution from the wind dependent emission sources was masked by contributions from other sources.

In the assessment of the two Case Studies, the MB95 dust-flux scheme provided a very good fit with measured data for both cases. The roughness length (z_0) was the only parameter to be scaled, and for both cases it remained within the range of 0.003 m and 0.007 m. This range falls within the surface configuration of the *"thin short cut grass"* regarded as representative of both the gold and platinum TSFs surface conditions. The SH11 dust-flux scheme provided significant higher emissions, resulting in over-predictions with measured data for both Case Study 1 and 2. However, by applying the correction factor (CFη_{mi}) of 0.22 (specific to the PM$_{10}$ fraction), a very good agreement was found with measured data for Case Study 1 and a significantly improved agreement was found for Case Study 2.

The spatial variations in modelled ground level concentrations were revealed in both Case Studies where the MB95 and SH11 dust-flux rates resulted in slightly different spatial impact zones for Case Study 1 and vastly different impact zones for Case Study 2. The disparity in Case Study 2 was a direct function of the factor 4 difference in quantified emission rates between the two dust-flux schemes. The spatial variation between the 10-minute and hourly-derived emission rates were also demonstrated in Case Study 2, again because of the difference in the emission rates from the two approaches.

6 Summary and Conclusion

The research outcome is recapitulated, linking the findings to the thesis objectives and confirming the hypothesis. An argument is set forward for the significance of this thesis in the context of wind erosion impact assessments and the application of the developed methodology for air quality impact assessments. Recommendations for further research and analysis are suggested.

This thesis successfully demonstrated that it is possible, with appropriate parameterisation and modern dispersion models, to simulate wind-blown dust emissions from mine tailings and ash storage facilities with sufficient accuracy to aid environmental impact assessment and management of mine residue tailings. This answers the primary hypothesis of the thesis. The main findings from this study to support this assertion are summarised below.

Comparisons were made by testing the functional dependence of selected dust emission schemes on influencing variables, using a generic dataset, from which the most appropriate schemes for different source types – gold tailings material, platinum tailings material and coal ash – were selected. The two selected schemes – i.e. the widely applied dust-flux scheme developed by Marticorena and Bergametti (1995) and the most recently simplified version of the Shao 2004 dust-flux scheme (Shao *et al.* 2011) – demonstrated that simulated wind-blown dust from mine tailings storage facilities, on a local scale, using a Gaussian plume model, can both provide results within the accuracy range of the model.

6.1 Research Findings

The main influencing parameter on saltation flux rates, and subsequently dust-flux rates, is the threshold friction velocity (u^*_t). All the saltation flux models evaluated showed sensitivity to the friction velocity (u^*), with the model of White (1979) the least sensitive to u^*. The Iversen & White (1982) equation for quantifying u^*_t is the most sensitive to particle sizes where $d < 75$ μm, resulting in an exponential increase in u^*_t for $d < 10$ μm. Lu & Shao (1999) provides a more simplified method but with a similar sensitivity to the smaller particle sizes. Both approaches can be regarded as representative, resulting in similar values for u^*_t in this study.

The friction velocity (u^*), although independent from u^*_t, would only result in saltation flux rates where $u^* > u^*_t$. The friction velocity (u^*) is highly sensitive to the roughness length (z_0) with corrections for moisture and drag partitioning significantly influencing u^*_t. The smooth roughness length (z_{0s}), as determined through $D/30$ where D is the height of the roughness elements, can be

used as a first approximation. Accounting for the Owen resulted in extremely high threshold friction velocities yielding no saltation flux rates.

The dust-flux schemes of Shao (1996), Marticorena and Bergametti (1995), Lu and Shao (1999) and Shao (2004) were found to be in good agreement with each other, with the application of generic data. The dust-flux scheme of Marticorena and Bergametti (1995) is based on an empirical approach, with the sensitivity to the soil clay content seen as a limitation since it can only be applied to materials where the clay content is less than 20%. The binding-energy based scheme of Shao (2004), an improvement on both the Shao (1996), and the Lu and Shao (1999) dust emission schemes, is highly sensitive to plastic pressure (P) and the related coefficient c_y, both of which are difficult to determine. Shao (2004) further requires: both the minimally disturbed dust fraction (η_{mi}); the percentage free dust without aggregate breakup; and the fully disturbed dust fraction (η_{mi}); the percentage free dust from aggregate breakup. Shao *et al.* (2011) provided a basic form of the 2004 scheme, where the fully dispersed dust fraction (η_{fi}) is not required. Although the selection of an appropriate horizontal dust-flux model was not that obvious, the dust-flux scheme of Marticorena and Bergametti (1995) was selected, based on its simplicity and extensive application in Aeolian studies, with the basic form of the Shao 2004 scheme (Shao *et al.*, 2011) being selected based on its physical properties and simplified input parameters. In this study, the saltation flux formulation, as proposed by White (1979), was used for both dust-flux schemes.

In the quantification of the threshold friction velocity (u^{*}_{t}), corrections were made for the effect from moisture content and drag partitioning (R). The empirical relationship between adsorbed moisture (w') and soil clay content (η_{c}), as proposed by Fécan *et al.* (1999), was used for the moisture correction. Correcting for the effect from drag partitioning (R) was found to negate saltation flux rates in both Case Studies. Similarly, accounting for the effect of crusting will result in significant reductions in the dust-flux rates and should be carefully applied where crusting is a consideration. The method proposed by Goossens (2004) was used to account for the crusting effect, with the uncertainty linked to the quantification of the crust strength (τ). In this study, crust strength was assumed to be similar to plastic pressure (P), where both relate to the resistance of the surface material measured in Pascal.

Plastic pressure (P) was estimated through the interpolation of P values, as provided by Shao (2004) for natural soils, where P ranges between 5 000 Pa for sandy soils, 17 500 Pa for silt soils and 30 000 Pa for clay soils. In addition, P was calculated following the methodology proposed by Gillette *et al.* (1980) for quantifying the modulus of rupture based on the exchangeable sodium, calcium carbonate and clay content. This yielded similar results when using the interpolated values for P, for both the gold and platinum tailings and the ash material tested. The coefficient c_y was approximated using the same interpolation approach applied to P, where c_y is given by Shao (2004) to vary between 1×10^{-5} for clay soils, 3×10^{-5} for silt soils and 5×10^{-5} for sandy soils. The

applicability of using interpolated soil values for P and c_y to tailings and ash material could not be established because of the lack of field measurements. The mineralogy of mine tailings and ash storage facilities is also very different from natural soils, on which the interpolated P was based. However, the good agreement found between modelled- and measured-ambient PM_{10} concentrations implies that this approach is suitable.

The variability in dust emissions between the two dust-flux schemes of Marticorena and Bergametti (1995) and that of Shao *et al.* (2011) was confirmed through the application to gold and platinum tailings- and coal ash-material. The uncertainty in both dust-flux schemes is greatest at low wind speeds and reduces with increased wind speeds. The correlation between the two dust-flux schemes were found to improve at higher wind speeds and, for materials containing large percentage of fine material, at sizes less than 75 μm.

For all three material types tested, the Shao *et al.* (2011) dust-flux scheme resulted in higher emissions when compared with the results from the Marticorena and Bergametti (1995) scheme. This can be explained by the assumption that the particle size distribution (*psd*) data are representative of the minimally disturbed dust fraction (η_{mi}) – whereas, in fact, it is more representative of the fully disturbed dust fraction (η_{fi}). The Malvern Mastersizer® 2000 analysis methodology causes the partial mechanical breakup of agglomerates and does not present the undisturbed particle size distribution data. By applying a correction factor ($CF\eta_{mi}$) of 0.22 to the η_{mi} fraction for PM_{10} specifically, as derived from the Chandler *et al.* (2002) field measurements, the correlation between the two dust-flux schemes improved significantly for all source material tested. This was confirmed by the results in the two Case Studies, where the correction to the gold TSFs data, resulted in a very good fit between modelled- and measured-PM_{10} concentrations for the Shao *et al.* (2011) approach. This also confirmed that the *psd*, as derived from the Malvern Mastersizer® 2000 analysis methodology, is more representative of the η_{fi} than of the η_{mi}.

The sensitivity of both dust-flux schemes to the wind speed frequency was confirmed where, on average, the use of sub-hourly wind velocities, at either 10-minute or 5-minute intervals, resulted in higher emissions than when the emissions were derived from hourly average wind data. This volatility is a result of the relation between u^* and u^*_t, whereby gusty turbulent winds over short time intervals – 5-minute data in Case Study 1, resulted in higher friction velocities, u^*, above the threshold friction velocity, u^*_t. When averaged over an hour, the resulting friction velocities, u^*, fell below the threshold friction velocity, u^*_t, resulting in zero calculated emissions for Case Study 1. For Case Study 2, where the variations in wind speed between the 10-minute data and the hourly averaged data were small, the disparity between the two sets of dust emission rates was also less, ~3%. On average it was found that the hourly averages tended to result in friction velocities, u^*, closer to the threshold friction velocity, u^*_t, causing lower saltation flux rates (Q) and subsequently

lower dust flux rates (F). This parameterisation analysis confirmed the sensitivity of dust-flux schemes to intervals of wind speed averaging.

The influence of the logarithmic wind speed profiles were also tested, showing the application of the neutral logarithmic wind speed profile as a simplistic approximation to result in a large under estimation of dust-flux emissions, irrespective of the dust-flux scheme used. The modified version of the logarithmic wind speed profile, when atmospheric conditions are not neutral, was used for emission quantification in both case studies, resulting in a good agreement between the modelled and measured concentrations.

For the model appraisal, measured PM_{10} concentrations from two separate ambient monitoring stations in close proximity to tailings storage facilities (TSFs) were used. The dust contribution from the tailings storage facilities to the measured PM_{10} concentrations was determined by extracting only the periods when the wind blew from the TSFs and exceeded a friction velocity of $3\ m\ s^{-1}$. Wind-blown emissions were quantified for the same period and simulated to provide a comparison to the measured data. The roughness length (z_0), being the only irresolute input parameter, was scaled until the dust-flux schemes provided modelled concentrations in good agreement with measured data. For both case studies – i.e. the gold TSFs and the platinum TSF – the roughness length (z_0) remained within the range of 0.003 m and 0.007 m, falling within the surface configuration of *"thin short cut grass"* which is regarded as representative of both the gold and platinum TSFs surface conditions.

Modelling wind erosion, as an hourly variable input file to AERMOD with the TSFs included as area sources, provided ground level PM_{10} concentrations in good agreement with measured data and demonstrated the regulatory plume model to be a useful tool for wind-blown dust assessments. The spatial variation in modelled ground level PM_{10} concentrations from the two dust-flux schemes were confirmed, with a direct relation to the deviation in average dust emission rates between the two schemes.

Both dust-flux schemes, that of Marticorena and Bergametti (1995), and of Shao *et al.* (2011) when corrected with the $CF\eta_{mi}$, resulted in modelled ground level PM_{10} concentrations in good agreement with measured PM_{10} concentrations. The Marticorena and Bergametti (1995) dust-flux scheme is preferred for use in wind erosion assessments for tailings and ash storage facilities because of its simplicity. The most important input parameters to consider in the quantification of wind-blown dust are the material particle size distribution (*psd*), clay content and moisture content. The Marticorena and Bergametti (1995) dust-flux scheme is not spectral and should be linked to the particle size groups under investigation through treatment similar to the least square fitting technique, as applied in the Shao *et al.* (2011) scheme.

6.2 Significance

This study provides a significant contribution to the current knowledge on air quality impact assessment methodology for wind-blown dust from mine tailings and ash storage facilities. This thesis demonstrates that simulated impacts from complex source groups can be performed, within an acceptable range of certainty, using widely applied dust-flux schemes. These dust-flux schemes, developed primarily for large-scale desert and arid areas, have been demonstrated to be applicable also to small-scale sources, of the order of $1\,km^2$, and can be coupled to regularly available dispersion models for impact evaluations of wind-blown dust. The value of this improved approach to the mining and mineral processing industries are substantial, allowing for a more accurate assessment of dust dispersion from large material storage piles, a source category that has hitherto been difficult to quantify. Previous work on wind erosion have validated these emission equations in wind tunnel studies – this is the first study to validate Marticorena and Bergametti (1995) and Shao *et al.* (2011) flux schemes in field measurements on operational mine and ash tailings facilities. Consequently, potential health risks and adverse environmental influences from wind-blown dust can be simulated – including instances for which no ambient data exist or where new storage facilities are proposed for development. In the South African context, where many mine tailings storage facilities are located near residential areas, this will become a useful tool for assessing not only the health risks associated with dust but also the risk associated with hazardous elements in the source material.

6.3 Recommendations

The Shao *et al.* (2011) dust-flux scheme, because of its sound consideration of dust emission physics, should be further investigated with field tests conducted to determine suitable values for P relating specifically to gold and platinum tailings and ash material. The correction factor ($CF\eta_{mi}$), which relates to the PM_{10} size fraction in this study, should also be investigated further and tested for a range of particle size categories (such as $PM_{2.5}$ and PM_{75}).

The difference in the mineralogy and mineral textural characteristics of mine tailings and ash deposits compared to that of soils in natural or agricultural environments should be further investigated to provide an integrated understanding of the chemical processes, weathering and decomposition.

Emission rates should preferably be calculated using sub-hourly (10-minute or 5-minute) rather than hourly average wind velocities. This will require a change in standard procedures for programming data loggers and storing surface meteorological data. The sensitivity of the dust emission rates to the potential variability between sub-hourly wind velocities and hourly averaged velocities is greatest where intermittent sub-hourly wind speeds are high, for instance during convective thunderstorms common on the South African Highveld .

The importance of long-term ambient measured data, collected downwind from mine tailings storage and ash storage facilities, was highlighted and it is recommended, in the light of the increasing health concerns related to Aeolian dust from these storage facilities, that more ambient dust monitoring stations should be installed. These stations should include, at a minimum, wind gauges measuring either five or ten-minute wind speed and wind direction data, together with ambient PM_{10} and $PM_{2.5}$ concentrations at the same time intervals.

The significance of the findings from Case Study 1 dictates the use of sub-hourly wind speed data for dust emission calculation. Where such data are not available, the uncertainty around the dust emissions increases and should be reported.

It will be useful to compile a database of typical roughness lengths (z_0) associated with different mine tailings and ash storage surface conditions, to be used where no ambient dust concentrations are available to validate the emission model.

The effects of crusting on mine tailings and ash storage facilities should be tested. This should include testing of the crust strength, and how this affects mine tailings resilience to wind erosion.

Careful consideration should be given to the correction of u^*_t by accounting for drag partitioning (R) and moisture content because these corrections can yield no emissions, a situation which may not reflect reality. Further investigations are also required to understand the behaviour of mine tailings and ash material under conditions of high velocity winds.

References

Agreenco, 2010. Dust Management Best Practice Guidelines for Tailings Storage Facilities. Report to AngloGold Ashanti, December 2010, Potchefstroom: Agreenco Environmental Projects.

Alfaro, S. C. & Gomes, L., 2001. Modeling mineral aerosol production by wind erosion: Emission intensities and aerosol size distributions in source areas. *Journal of Geophysical Research*, 106, 18075–18084.

Alfaro, S. C. & Rajot, J. L., 2002. Estimation of PM20 emissions by wind erosion: Main sources of uncertainties. Proceedings of ICAR5/GCTE-SEN Joint Conference, 2002, Lubbock. Lubbock: Texas Technical University, Publication 02-2.

Alfaro, S. C., Gaudichet, A., Gomes, L. & Maille, M., 1997. Modeling the size distribution of a soil aerosol produced by sandblasting. *Journal of Geophysical Research*, 11, 239-249.

Annegarn, H. J., n.d. Control of dust emission and impacts from surface mines and works. Proceedings from the SAIMM Colloquium, n.d., Johannesburg.

Annegarn, H. J., 2006. Implications of the new Air Quality Act for the residential built environment. *Environmental Management*, 1, 18-21.

Annegarn, H. J., Sithole, J., Lethlage, D., Mphati, D., Jood, V., Malahlela, J., & Mthethwa, D., 2000. A case study in environmental conflict resolution between the community and the Rand Leases Mine Tailings Dump. *Clean Air Journal*, 10, 3-6.

Annegarn, H. J., Ojelede, M. E., Kneen, M. A., & Umba-Ndolo, G., 2010. Dust Monitoring Project: Assessment of Gold Mine Tailings and Related Impacts on Neighbouring Communities in the Vicinity of AngloGold Ashanti Operations in the Vaal River and West Wits Areas, DMP/2010/UJ-01, 105, University of Johannesburg, Johannesburg.

ASTM Standard D1739-98, 2004. Standard test Method for Collections and Measurement of Dustfall (Settleable Particulate Matter). ASTM International: West Conshohocken, PA.

Bagnold, R. A., 1941. The Physics of Blown Sand and Desert Dunes. London: Methuen.

Belly, P.Y., 1964. Sand movement by wind. Technical report no. 1 to US Army Coastal Engineering Research Center.

Beniston, M., Ruffieux, D. and Hertig, J-A., 1989. A combined numerical and wind-tunnel study of ventilation and air pollution episodes in a rural valley of Switzerland. *Boundary-Layer Meteorology*, 48, 129-156.

Blight, G. E., 1989. Erosion losses from the surfaces of gold-tailings dams. *Journal of South African Institute of Mining Metallurgy*, 89, 23-29.

Blight, G. E., 1991. Erosion and Anti-erosion measures for abandoned Gold Tailings Dams. Proceedings from the National Meeting of the American Society for Surface Mining and Reclamation. 1991, Durango: Colorado.

Blight, G. E., 2003. An examination of the erosive effect of wind on the slopes and interior surfaces of tailings impoundments. *Tailings and Mine Waste*, 2003 Swets & Zeitlinger, Lisse, 193-199.

Blight, G. E., 2008. Wind erosion of waste impoundments in arid climates and mitigation of dust pollution. *Waste Management and Research*, 23, 523-533.

Blight, G. E. & Amponsa Da Costa, F., 1999. Improving the erosion stability of tailings dam slopes. *Tailings and Mine Waste*, 1999 Rotterdam, Balkema, 197-206.

Blight, G. E. & Amponsah Da Costa, F., 2001. On the mechanics of wind erosion from tailings dams. *Tailings and Mine Waste,* 2001 Balkema, Rotterdam, 189-196.

Boswell, J., 1986. The disposal of power station ash by Eskom in South Africa., Report to Eskom, 1986, Eskom Civil.

Brigden, K. & Santillo , D., 2002. Heavy metal and metalloid content of fly ash collected from the Sual, Mauban and Masinloc coal-fired power plants in the Philippines, 2002. University of Exeter: Exeter.

Bullard, J. E., 2006. Arid geomorphology. *Progress in Physical Geography*, 30, 542-552.

Burger, L.W., 1986. A high resolution model for multiple source dispersion of air pollutants under complex atmospheric structure. Doctoral dissertation. Durban: University of Natal.

Burger, L. W., 2010. Complexities in the estimation of emissions and impacts of wind generated fugitive dust. Proceedings of the National Association for Clean Air Annual Conference, 14 & 15 October 2010, Polokwane.

Burger, L.W., Held, G. & Snow, N. H., 1997. Revised User's Manual for the Airborne Dust Dispersion Model from Area Sources (ADDAS), Eskom Report No. TRR/T97/066, December 1997, Johannesburg: Eskom TSI.

Businger, J. A., Wyngaard, J. C., Izumi, Y. & Bradley, E. F., 1971. Flux-profile relationships in the atmospheric surface layer. *Journal of Atmosperic Science*, 28, 191-198.

Callot, Y., Marticorena, B. & Bergametti, G., 2000. Geomorphologic approach for modelling the surface features of arid environments in a model of dust emissions: application to the Sahara desert. *Geodinamica Acta*, 13, 245–270.

Carslaw, D. C. & Ropkins, K., 2012. openair — an R package for air quality data analysis. *Environmental Modelling & Software*, 27-28, 52-61.

Carslaw, D. C., 2013. The openair manual — open-source tools for analysing air pollution data. Manual for version 0.8-0, 14 February 2013, London: King's College.

CERC., 2004. Boundary layer. http://www.cerc.co.uk/environmental-research/boundary-layer.html (Accessed 12 January 2013).

Chandler, D., Saxton, K., Kjelgaard, J. & Busacca, J., 2002. A technique to measure fine-dust emission potentials during wind erosion. *Soil Science Society of America Journal*, 66, 1127-1133.

Chepil, W.S., & Woodruff, N.P., 1963. The physics of wind erosion and its control. *Advances in Agronomy*, 15, 211-302.

Clements, T., Stone, R., Mann, J. & Eymann, J. L., 1963. A study of Windborne Sand and Dust in Desert Areas. Natick, Massachusetts: U.S. Army Research Institute of Environmental Medicine, Earth Sciences Laboratory.

Colls, J., 2002. *Air Pollution*. 2nd edition. London: Taylor & Francis Group.

Cowherd, C., Muleski, G. E. & Kinsey, J. S., 1988. Control of open fugitive dust sources. Report to the U. S. Environmental Protection Agency, September 1988, Research Triangle Park, NC.

Darmenova, K., Sokolik, I.N., Shao, Y., Marticorena, B., Bergametti, G., 2009. Development of a physically based dust emission module within the Weather Research and Forecasting (WRF) model: Assessment of dust emission parameterizations and input parameters or source regions in Central and East Asia. *Journal of Geophysical Research*, 114, 000-000.

De Kok, P., King, H., & Snow, N.H., 1993. Majuba ash operations EIA, Eskom Report, Cleveland.

De Longueville, F., Ozer, P., Doumbia, S. & Henry, S., 2013. Desert dust impacts on human health: an alarming worldwide reality and a need for studies in West Africa.. *International Journal of Biometeorology,* 57, 1-19.

Diego, I., Pelegry, A., Torno, S., Toraño, J., Menendez, M., 2009. Simultaneous CFD evaluation of wind flow and dust mission in open storage piles. *Applied Mathematical Modelling,* 33, 3197-3207.

Dong, Z., Liu, X., Wang, X., Li, F., & Zhao, A., 2004 Experimental investigation of the velocity of a sand cloud blowing over a sandy surface. *Earth Surface Processes and Landforms*, 29, 343-358.

Ecotech, 2013. E-BAM PM monitors. http://www.ecotech.com.au/particulates/e-bam (Accessed 14 May 2013).

Eswaran, H. R. L. & Reich, P. F., 2001. Land degradation: an overview. Proceedings 2nd International Conference on Land Degradation and Desertification, 2001, Khon Kaen. Thailand: Oxford Press.

Fécan, F., Marticorena, B. & Bergametti, G., 1999. Parameterisation of the increase of the aeolian erosion threshold wind friction velocity due to soil moisture for arid and semi-arid areas. *Annales Geophysicae*, 17, 149-157.

Formenti, P., Annegarn, H. J. & Piketh, S. J., 1998. Time resolved aerosol monitoring in the urban centre of Soweto. *Nuclear Instruments and Methods in Physics Research*, B 136-138, 948-954.

Friedman, G. & Sanders, J., 1978. *Principles of Sedimentology*. New York: Wiley.

Friedrich, R., 2009. Natural and biogenic emissions of environmentally relevant atmospheric trace constituents in Europe. *Atmospheric Environment,* 43, 1377-1379.

Friederichs, F., Weniger, M., Bentzien, S., & Hense, A., 2009. Stochastic versus Uncertainty Modeling. Proceedings of the Conference on Dynamics and Statistic in Weather and Climate, Dresden, July 29-31 2009.

Fryrear, D.W., 1996. Mechanics, Measurement and Modeling of Wind Erosion. Proceedings of the International Soil Conservation Organization Conference, 16 September 1996.

Fryrear, D.W., Saleh, A., Bilbro, J.D., Schomberg, H.M., J.E., & Zobeck, T.M., 1998. Revised Wind Erosion Equation (RWEQ). Technical Bulletin No. 1. Report to the Wind Erosion and Water Conservation Research Unit, USDA-ARS, Southern Plains Area Cropping Systems Research Laboratory.

Garstang , M., Kelbe , B., Emmitt , G. & London, W., 1987. Generation of Convective Storms over the Escarpment of Northeastern South Africa.. *American Meteorological Society*., 115, 429-443.

Giannadaki, D., Pozzer , A. & Lelieveld , J., 2014. Modeled global effects of airborne desert dust on air quality and premature mortality. *Atmospheric Chemistry and Physics,* 14, 957-968.

Gillette, D. A., 1977. Fine particulate emissions due to wind erosion. *Trans American Society of Agricultural Engineers*, 20, 890-987.

Gillette, D. A., 1978. Tests with a portable wind tunnel for determining wind erosion threshold velocities. *Atmospheric Environment*, 12, 2309-2313.

Gillette, D. A., Adams, J., Endo, A., Smith, D., & Kihl, R., 1980. Threshold friction velocities for input of soil particles into the air by desert soils. *Journal of Geophysical Research*, 85, 5621-5630.

Gillette, D. A., Adams, J., Muhs, D. & Kihl, R., 1982. Threshold friction velocities and rupture moduli for crusted desert soils for the input of soil particles into the air. *Journal of Geophysical Research*, 87, 9003-9015.

Gillette, D. A. & Chen, W., 1999. Size distribution of saltating grains: an important variable in the production of suspended particles. *Earth Surface Processes and Landforms*, 24, 449-462.

Gillette, D. A. & Passi, R., 1988. Modeling dust emission caused by wind erosion. *Journal of Geophysical Research*, 93, 14 233-14 242.

Ginoux, P., Prospero, J. M., Torres, O. & Chin, M., 2004. Long-term simulation of global dust distribution with the GOCART model: correlation with North Atlantic Oscillation. *Environmental Modelling and Software*, 19, 113-128.

Glaccum, R. A. & Prospero, J. M., 1980. Saharan aerosols over the tropical North Atlantic – Mineralogy. *Marine Geology*, 37, 295-321.

Goldreich, Y. & Tyson, P. D., 1988. Diurnal and inter-diurnal variations in large-scale atmospheric turbulence over southern Africa. *South African Geographical Journal*, 70, 48-56.

Goliger, A., Retief, J. & Dunaiski, P., 2009. Review of codification of wind-loading for structural design. Edited by J. Retief & P. Dunaiski. Chapter 3-1 in *Background to SANS 10160*. Stellenbosch: SunMedia.

Goossens, D., 2004. Effect of soil crusting on the emission and transport of wind-eroded sediment: field measurements on loamy sandy soil. *Geomorphology*, 58, 145-160.

Goudie, A. S., 2009. Dust storms: Recent developments. *Journal of Environmental Management*, 90, 89–94.

Greeley, R. & Iversen, J. D., 1985. *Wind as a Geological Process on Earth, Mars, Venus and Titan*. New York: Cambridge University Press.

Griffin, R.A., Schuller, R.M., Suloway, J.J., Russell, S.A.M., Childers, W.F., & Shrimp, N.F., 1977. Solubility and toxicity if potential pollutants in solid coal wastes. Symposium proceedings on the Environmental Aspects of Fuel Conversion Technology, III, September 1977, Holywood, Florida.

Han, Z. W., Ueda, H., Matsuda, K., Zhang, R. J., Arao, K., Kanai, Y., & Hasome, H., 2004. Model study on particle size segregation and deposition during Asian dust events in March 2002. *Journal of Geophysical Research*, 109.

Hanna, S., Briggs, G., Deardorff, J. & Egan, B., 1977. AMS workshop on stability classification schemes and sigma curves-summary of recommendations. *Bulletin of American Meteorological Society*, 58, 1305-1309.

Hanna, S. R., Egan, B. A., Purdum, J. & Wagler, J., 1999. Evaluation of the ADMS, AERMOD, and ISC3 dispersion models with the Optex, Duke Forest, Kincaid, Indianapolis, and Lovett field data sets. *International Journal of Environment and Pollution*, 16, 1-6.

Hillel, D., 1980. *Applications of Soil Physics*. New York: Academic Press.

Holmes, N. S. & Morawska, L., 2006. A review of dispersion modelling and its application to the dispersion of particles: An overview of different dispersion models available. *Atmospheric Environment*, 40, 5902–5928.

IFC, 2007. Environmental, Health and Safety Guidelines, General EHS Guidelines. 30 April 2007, International Finance Corporation, World Bank Group.

IFC, 2008. Environmental, Health, and Safety Guidelines; Thermal Power Plants 19 December 2008, International Finance Corporation, World Bank Group.

IRIS, 2014. Integrated Risk Information System (IRIS). http://www.epa.gov/iris (Accessed 2 May 2014).

Iversen, J. D. & White, B. R., 1982. Saltation threshold on Earth, Mars and Venus. *Sedimentology*, 29, 111-119.

Iversen, J. D., Greeley, R., & Pollack, J. B., 1976: Windblown dust on Earth, Mars and Venus. *Journal of Atmospheric Sciences*, 33, 2425–2429.

Iversen, J.D. Greeley, R., Marshall, J.R., & Pollack, P.B., 1987 Aeolian saltation threshold: The effect of density ratio. *Sedimentology*, 34, 699-706.

Jackson, P. & Hunt, J. C. R., 1975. Turbulent wind flow over a low hill. *Quarterly Journal of the Royal Meteorological Society*, 101, 929-955.

Jayaratne, E .R., Johnson, G. R., McGarry, P., Cheung, H. C., & Morawska, L., 2011. Characteristics of airborne ultrafine and coarse particles during the Australian dust storm of 23 September 2009. *Atmospheric Environment*, 45, 3996–4001.

Kalthoff, N., Horlacher, V., Corsmeier, U., Volz-Thomas, A., Kolhagar, B., Geiss, H., Mollmann-Coers, M., & Knaps, A., 2000. Influence of valley winds on transport and dispersion of airborne pollutants in the Freiburg-Schauinsland area. *Journal of Geophysical Research-Atmospheres*, 105, 1585-1597.

Kang, J-Y., 2011. Implementation of dust emission schemes into WRF/Chem: An evaluation of dust emission parameterizations. Doctoral dissertation. Seoul: Seoul National University.

Karanasiou, A., Moreno , N ., Moreno, T., Viana , M., de Leeuw , F., Querol, X., 2012. Health effects from Sahara dust episodes in Europe: literature review and research gaps.. *Environment International,* 15, 107-114.

Kawamura, R., 1964. *Study of sand movement by wind*. Berkeley: University of California.

Kok, J. F., 2011. Does the size distribution of mineral dust aerosols depend on the wind speed at emission? *Atmospheric Chemistry and Physics Discussions*, 11, 19995–20012.

Kok, J. F., Parteli, E., Michaels, T. & Bou Karam, D., 2012. The physics of wind-blown sand and dust. *Reports on Progress in Physics,* 75, 000-000.

Kon, L. C., Durucan, S. & Korre, A., 2007. The development and application of a wind erosion model for the assessment of fugitive dust emissions from mine tailings dumps. *International Journal of Mining, Reclamation and Environment*, 21, 198-218.

Kruger, A., Goliger, A. M., Retief, J. V. & Sekele, S., 2010. Strong wind climatic zones in South Africa. *Wind and Structures*, 13, 000-000.

Kruger, A., Retief, J. & Goliger, A., 2013. Strong winds in South Africa: Part 2 Mapping updated statistics. *Journal of the South African Institution of Civil Engineering*, 55, 000-000.

Laurent, B., Marticorena, B., Bergametti, G. & Mei, F., 2006. Modeling mineral dust emissions from Chinese and Mongolian deserts. *Global and Planetary Change*, 52, 121-141.

Lettau, K., & Lettau, H.H., 1978. Experimental and micrometeorological field studies of dune migration. *Exploring the Worlds Driest Climate*. Madison, WI: University of Wisconsin.

Liebenberg-Enslin H., Thomas R., van Nierop M. & Walton N, 2009. Vaal Triangle Airshed Priority Area Air Quality Management Plan. Report to the Department of Environmental Affairs and Tourism, March 2009, Pretoria: Department of Environmental Affairs and Tourism.

Liebenberg-Enslin, H., Krause, N. & Breitenbach, N., 2010. Strategic Environmental Assessment for the Central Namib 'Uranium Rush- Air Quality Specialist Report. Report APP/09/MME-02-Rev0 to the Ministry of Mines and Energy, Namibia.

Loosmore, G.A., & Hunt, J.R., 2000. Dust resuspension without saltation. *Journal of Geophysical Research*, 105, 20663-20672.

Lu, H., 1999. An Integrated Wind Erosion Modelling System with Emphasis on Dust Emission and Transport. Doctoral dissertation. Sydney: The University of New South Wales.

Lu, H. & Shao, Y., 1999. A new model for dust emission by saltation bombardment. *Journal of Geophysical Research*, 104, 16,827-16,842.

Lu, H. & Shao, Y., 2001. Toward quantitative prediction of dust storms: an integrated wind erosion modelling system and its applications. *Environmental Modelling & Software*, 16, 233–249.

Lui, X.P., & Dong, Z.B., 2004. Experimental investigation of the concentration profile of a blowing sand cloud. *Geomorphology*, 60, 371-31.

MacKinnon, D.J., Clow, G.D., Tigges, R.K., Reynolds, R.L., & Chaves , P.S. Jr., 2004. Comparison of aerodynamically and model-derived roughness lengths (z0) over diverse surfaces, central Mojave Desert, California, USA. *Geomorphology*, 63, 103-113.

Mahowald, N.M., Kloster, S., Engelstaedter, S., Moore, J. K., Mukhopadhyay, S., McConnell, J. R., Albani, S., Doney, S. C., Bhattacharya, A., Curran, M. A. J., Flanner, M. G., Hoffman F. M., Lawrence, D. M., Lindsay, K., Mayewski, P. A., Neff, J., Rothenberg, D., Thomas, E., Thornton, P. E., & Zender, C. S., 2010. Observed 20th century desert dust variability: Impact on climate and biogeochemistry. *Atmospheric Chemistry and Physics,* 10, 875-893.

Maier, R. M., 2009. Phytostabilization of Mine Tailings in Arid and Semi-Arid Environments: Plant-Soil-Microbe Interactions and Metal Speciation Dynamics. http://ag.arizona.edu/swes/maier_lab/mine_tailings.html (Accessed 23 January 2013).

Marshall, J., 1971. Drag measurements in roughness arrays of varying density and distribution. *Journal of Agricultural Meteorology*, 8, 269-292.

Marticorena, B. & Bergametti, G., 1995. Modeling the atmospheric dust cycle. Design of a soil-derived dust emission scheme. *Journal of Geophysical Research*, 16, 415 – 16430.

Marticorena, B., Bergametti, G., Aumont, B., Callot, Y., N'Doume, C., & Legrand, M., 1997. Modeling the atmospheric dust cycle. Simulation of Saharan dust sources. *Journal of Geophysical Research*, 102, 4387-4404.

Maseki, J., 2013. Risk Assessment of Inhaled and Ingested Airborne Particles in the vicinity of Gold Mine Tailings: Case Study of the Witwatersrand Basin. Masters dissertation. Johannesburg: University of Johannesburg.

McKenna Neuman, C., 2004. Effects of temperature and humidity upon the transport of sedimentary particles by wind. *Sedimentology*, 51, 1-18.

McKenna Neuman, C. & Nickling, W. G., 1989. A theoretical and wind tunnel investigation of the effect of capillary water on the entrainment of sediment by wind. *Canadian Journal of Soil Science*, 69, 79-96.

McKenna Neuman, C., Boulton, J. W. & Sanderson, S., 2009. Wind tunnel simulation of environmental controls on fugitive dust emissions from mine tailings. *Atmospheric Environment*, 43, 520-529.

MFE, 2001. Good Practice Guide for Preparing Emissions Inventories. Wellington, New Zeeland: Ministry for the Environment.

MFE, 2004. Good Practice Guide for Atmospheric Dispersion Modelling, Wellington, New Zeeland: Ministry for the Environment.

Mian, M. & Yanful, E., 2003. Tailings erosion and resuspension in two mine tailings ponds due to wind waves. *Advances in Environmental Research*, 7, 745-765.

Miller, R.L., Tegen, I., & Perlwitz, J.P., 2004. Surface radiative forcing by soil dust aerosols and the hydrologic cycle. *Journal of Geophysical Research*, 109, D04203, doi:10.1029/2003JD004085.

Mining Intelligence Database., 2013. http://www.projectsiq.co.za/gold-mining-in-south-africa.htm (Accessed 13 July 2013).

MME, 2011. Strategic Environmental Assessment for the central Namib Uranium Rush, Report to the Ministry of Mines and Energy, Namibia, January 2011, Windhoek: Ministry of Mines and Energy.

Myhre, G. & Stordal, F., 1997. Role of spatial and temporal variations in the computation of radiative forcing and GWP. *Journal of Geophysical Research*, 102, 181-200.

National Research Council, 2001. Air quality management in the United States. Washington D.C.: The National Academies Press.

Ojelede, M. E., Annegarn, H. J. & Kneen, M. A., 2012. Evaluation of aeolian emissions from gold mine tailings on the Witwatersrand. *Aeolian Research*, 3, 477–486.

Owen, P. R., 1964. Saltation of uniform grains in air. *Journal of Fluid Mechanics*, 20, 225-242.

Phakedi, S., 2011. Population exposure to cyanide vapour from gold mine tailings dams. Masters dissertation. Johannesburg: University of Johannesburg.

Piketh, S., Annegarn , H. & Tyson, P., 1999. Lower tropospheric aerosol loadings over South Africa: The relative contribution of aeolian dust, industrial emissions, and biomass burning. *Journal of Geophysical Research,* 104, 1597-1607.

Preston-Whyte, R. & Tyson, P., 1988. *The Atmosphere and Weather of Southern Africa*. Cape Town: Oxford University Press.

Prinsloo, J. J., 2007. A comparative analysis of economic value created by South African Mining Companies in a growing Platinum Industry. Masters dissertation. Pretoria: University of Pretoria.

Prospero, J. M., 1981. Eolian transport to the World Ocean, in The Oceanic Lithosphere. *The Sea*, 7, 801-874.

Pulles, P. & Heslinga, D., n.d. The Art of Emission Inventorying: A pragmatic approach to Emission Inventories for various applications., n.d., TNO-Environment and Geosciences.

Pye, K. & Tsoar, H., 2009. *Aeolian Sand and Sand Dunes*. Berlin: Springer.

Pye, K., 1987. *Aeolian Dust and Dust Deposits*. London: Academic Press.

Queensland Government., 2013. Soil erosion. http://www.nrm.qld.gov.au/land/management/erosion/index.html (Accessed 10 April 2013)

Rajot, J.L., Gomes, L., Alfaro, S.C., & Gaudichet, A., 2000. Poster Session I. Atmospheric aerosol modelling. Modelling mineral aerosol production by wind erosion: Part 2 field validation. *Journal of Aerosol Science*, 31, 428-429.

Raupach, M. R., 1991. Saltation layer vegetation canopies and roughness lengths. *Acta Mechanica*, 1, 135-144.

Raupach, M., Gillette, D. & Leys, J., 1993. The effect of roughness elements on wind erosion threshold. *Journal of Geophysical Research*, 98, 3023-3029.

Raupach, M. R. & Lu, H., 2004. Representation of land-surface processes in aeolian transport models. *Environmental Modelling & Software*, 19, 93-112.

Rice, M., Mullins, C. & McEwan, I., 1997. An analysis of soil crust strength in relation to potential abrasion by saltating particles. Earth Surfaces Processes and Landforms, 22, 869-883.

Rice, M., & McEwan, I., 2001. Crust strength: A wind tunnel study of the effect of impact by saltating particles in cohesive soil surfaces. *Earth Surface Processes and Landforms*, 26, 721-733.

Robertson, A. & Skermer, N., 1988. Design considerations for the long-term stability of mine wastes. https://www.rgc.ca (Accessed 11 March 2014).

Sagan, C., and Bagnold, R.A., 1975. Fluid transport on Earth and aeolian transport on Mars. *Icarus*, 26, 209–218.

Satheesh, S. K. & Moorthy, K. K., 2005. Radiative effects of natural aerosols: a review. *Atmospheric Environment*, 39, 2089–110.

SAWS, 2013. South African Weather Service. http://www.weathersa.co.za (Accessed 11 March 2014).

Schmechtig, C., Marticorena, B., Chatenet, B., Bergametti, G., Rajot, J. L., & Coman, A., 2011. Simulation of the mineral dust content over Western Africa from the event to the annual scale with the CHIMERE-DUST model. *Atmospheric Chemistry and Physics*, 11, 7185-7207.

SGS, 2011. Test Report: Toxicity Assessment of Soil Samples at East Plats Crocodile River Mine. Report to East Platinum Mines – Crocodile River Mine, Report No. GS377, 4 July 2011.

Shao, Y. & Lu, H., 2000. A simple expression for wind erosion threshold friction velocity. *Journal of Geophysical Research*, 22, 437-443.

Shao, Y. & Yang, Y., 2007. A theory for drag partition over rough surfaces. *Journal of Geophysical Research – Earth Surface*, 00-00.

Shao, Y., 2004. Simplification of a dust emission scheme and comparison with data. *Journal of Geophysical Research*, 109, 372.

Shao, Y., 2008. *Physics and Modelling of Wind Erosion*. 2nd revised and expanded edition. Berlin: Springer.

Shao, Y., Ishizuka, M., Mikami, M. & Leys, J. F., 2011. Parameterization of size-resolved dust emission and validation with measurements. *Journal of Geophysical Research*, 116, 1-19.

Shao, Y., Wyrwoll, K-H., Chappel, A., Huang, J., Zhaohui, L., McTainsh, G.H., Mikami, M., Tanaka, T.Y., Wang, X., & Yoon, S., 2011b. Dust cycle: An emerging core theme in Earth system science. *Aeolian Research*, 2,181-204.

Shao, Y., Raupach, M. R. & Leys, J. F., 1996. A model for predicting aeolian sand drift and dust entrainment on scales from paddock to region. *Australian Journal for Soil Research*, 34, 309-342.

Snow, N. & Held, G., 1998. Material flux monitoring at Tutuka Power Station Ash Disposal Site. Proceedings 11th World Clean Air and Environment Congress, 14 to 18 September 1998, Durban.

South Africa Info., 2012. Mining and Minerals in South Africa. http://www.southafrica.info/business/economy/sectors/mining.htm (Accessed 14 August 2012).

Stout, J. E., 1998. Effect of averaging time on the apparent threshold for aeolian transport. *Journal of Arid Environments*, 39, 395–401.

Stout, J. E., 2013. The bibliography of aeolian research. http://www.lbk.ars.usda.gov/wewc/biblio/bar.htm (Accessed 17 October 2013).

Tanaka, Y., & Chiba, M., 2006. A numerical study of the contributions of dust source regions to the global dust budget. *Global and Planetary Change*, 52, 88-104.

Tegen, I. & Fung, I., 1995. Contribution to the atmospheric mineral aerosol load from land surface modification. *Journal of Geophysical Research*, 100, 18707-18726.

Toraño, J.A., Rodriquez, R., Diego, I., Rivas, J.M., Pelegry, A., 2007. Influence of the pile shape on wind ersoion CFD emission simulation. *Applied Mathematical Modelling,* 31, 2487-2502.

Torrance, J. D., 1972. Malawi, Rhodesia and Zambia, in T H E Landsberg. *World Survey of Climatology*, 10.

Tyson, P., Garstang, M. & Swap, R., 1996. Large-scale Recirculation of Air over Southern Africa. *Journal of Applied Meteorology,* 35, 2218-2236.

US EPA, 1993. Compilation of Air Pollution Emission Factors: AP 42, Procedures for Sampling Surface/Bulk Dust Loading. http://www.epa.gov/ttn/chief/ap42/appendix/app-c1.pdf (Accessed 29 March 2014).

US EPA, 2006. Compilation of Air Pollution Emission Factors: AP 42, Fifth Edition, Volume I, Chapter 13. http://www.epa.gov/ttn/chief/ap42/ch13/index.html (Accessed 18 April 2012).

USGS-NASA., 2007. Malvern Instruments: Measurements of Particle Size Distribution by Wet & Dry Laser Diffraction. http://isru.msfc.nasa.gov (Accessed 13 July 2013).

Von Gruenewaldt, R., 2012. Continuous disposal of ash at Tutuka Power Station: Air Quality Evaluation. Report APP/12/LCE-03A to Lidwala Consulting Engineers, South Africa.

White, B., 1979. Soil transport by winds on Mars. *Journal of Geophysical Research*, 84, 4643-4651.

WHO, 2005. WHO Air Quality Guidelines global update 2005. Report on a working Group meeting, 18-20 October 2005, Bonn Germany: World Health Organisation.

Wiggs, G., Garvey, B., Castro, I. I. & Bullard, J., 2002. Interactions between airflow and valley topography with implications for Aeolian sediment transport. *Journal of Physical Geography*, 23, 366-380.

Yabuki, S., Kanayama, S., Fu, F.F., Honda, M., Yanagisawa, F., Wei, W.S., Zend, F.J., Liu, M.Z., Shen, Z.B., & Liu, L.C., 2002. Physical and chemical characteristics of aeolian dust collected over Asian dust source regions in China – comparison with atmospheric aerosols in an urban area at Wako, Japan. *Journal of Arid Land Studies*, 11, 273-289.

Zender, C. S., Bian, H. & Newman, D., 2003. The mineral dust entrainment and deposition (DEAD) model: Description and 1990[s] dust climatology. *Journal of Geophysical Research*, 108, 4416.

Zender, C., 2005. The Zender Group Webserver. http://dust.ess.uci.edu/ (Accessed 12 June 2011).

Zingg, A.W., 1953. Wind tunnel studies of the movement of sedimentary material. Proceedings of the 5th Hydraulic Conference, University of Iowa Studies in Engineering, Iowa City, IA.

Zobeck, T.M., 1991. Abrasion of crusted soils: Influence of abrader flux and soil properties. *Soil Science Society of America Journal*, 55, 1091-1097.

Zumdahl, S. S., Zumdahl, S. L., & Decoste, D. J., 2002. *World of Chemistry*. Boston: Houghton Mifflin Company.

Appendices

Appendix A: Particle Size Distributions for Three Tailings or Ash Storage Facilities

Particle size distributions for gold tailings

AngloGold	TSF1	TSF2	TSF3	TSF4	TSF5	TSF6
psd μm	West Extension	West Complex	South East	East Complex	South Complex	Sulphur Paydam
	Fractions as percentages					
0.05	-	-	0	0	0	0
0.06	-	-	0	0	0	0
0.07	-	-	0	0	0	0
0.08	-	-	0	0	0	0
0.09	-	-	0	0	0	0
0.11	0	0	0	0	0	0
0.13	0	0	0	0	0	0
0.15	0	0	0	0	0	0
0.17	0	0	0	0	0	0
0.20	0	0	0	0	0	0
0.23	0	0	0	0	0	0
0.27	0	0.01	0	0.05	0	0.02
0.31	0.05	0.06	0.05	0.06	0.05	0.02
0.36	0.11	0.10	0.12	0.10	0.12	0.04
0.42	0.16	0.15	0.19	0.15	0.19	0.07
0.49	0.23	0.21	0.27	0.21	0.27	0.10
0.58	0.30	0.27	0.36	0.27	0.36	0.13
0.67	0.38	0.35	0.47	0.35	0.47	0.18
0.78	0.48	0.44	0.61	0.43	0.61	0.23
0.91	0.58	0.53	0.76	0.52	0.76	0.29
1.1	0.68	0.64	0.91	0.61	0.91	0.35
1.2	0.78	0.75	1.07	0.71	1.07	0.40
1.4	0.89	0.87	1.24	0.81	1.24	0.46
1.7	1.01	1.02	1.43	0.92	1.43	0.53
2.0	1.14	1.19	1.64	1.05	1.64	0.60
2.3	1.27	1.39	1.86	1.18	1.86	0.69
2.7	1.43	1.63	2.11	1.33	2.11	0.79
3.1	1.58	1.88	2.38	1.49	2.38	0.90
3.6	1.75	2.16	2.64	1.64	2.64	1.01
4.2	1.91	2.45	2.89	1.79	2.89	1.11
4.9	2.06	2.72	3.13	1.93	3.13	1.22

AngloGold	TSF1	TSF2	TSF3	TSF4	TSF5	TSF6
psd µm	West Extension	West Complex	South East	East Complex	South Complex	Sulphur Paydam
Fractions as percentages						
5.7	2.21	2.98	3.34	2.05	3.34	1.32
6.6	2.34	3.18	3.50	2.14	3.50	1.40
7.7	2.44	3.31	3.59	2.20	3.59	1.45
9.0	2.52	3.37	3.62	2.22	3.62	1.47
10.5	2.59	3.34	3.59	2.21	3.59	1.47
12.2	2.65	3.25	3.52	2.19	3.52	1.46
14.2	2.71	3.11	3.44	2.16	3.44	1.43
16.6	2.77	2.96	3.37	2.15	3.37	1.40
19.3	2.85	2.82	3.34	2.18	3.34	1.38
22.5	2.94	2.72	3.36	2.25	3.36	1.37
26.2	3.04	2.67	3.41	2.38	3.41	1.39
30.5	3.14	2.70	3.51	2.58	3.51	1.45
35.6	3.24	2.80	3.61	2.84	3.61	1.58
41.4	3.35	2.96	3.71	3.15	3.71	1.79
48.3	3.46	3.16	3.80	3.49	3.80	2.11
56.2	3.58	3.40	3.73	3.85	3.73	2.57
65.5	3.71	3.66	3.55	4.20	3.55	3.16
76.3	3.87	3.93	3.30	4.52	3.30	3.90
88.9	4.03	4.13	2.98	4.82	2.98	4.75
103.6	4.18	4.19	2.61	5.09	2.61	5.61
120.7	4.22	4.05	2.19	5.07	2.19	6.38
140.6	4.11	3.69	1.78	4.84	1.78	7.00
163.8	3.81	3.15	1.37	4.42	1.37	7.50
190.8	3.33	2.48	0.96	3.83	0.96	7.18
222.3	2.70	1.77	0.55	3.10	0.55	6.44
259.0	1.94	1.06	0.14	2.30	0.14	5.35
301.7	1.14	0.34	-	1.49	-	4.06
351.5	0.34	-	-	0.68	-	2.78
409.5	-	-	-	-	-	1.50
477.0	-	-	-	-	-	0.21
Total	**100**	**100**	**100**	**100**	**100**	**100**

Particle size distributions for platinum tailings

Impala Platinum	TSF7	Impala Platinum	TSF7
	No. 2 TSF		**No. 2 TSF**
psd (μm)	**Fractions as %s**	*psd* (μm)	**Fractions as %**
0.17	0.01	16.6	1.91
0.20	0.02	19.3	2.17
0.23	0.04	22.5	2.49
0.27	0.05	26.2	2.85
0.31	0.08	30.5	3.25
0.36	0.10	35.6	3.67
0.42	0.14	41.4	4.10
0.49	0.17	48.3	4.49
0.58	0.21	56.2	4.83
0.67	0.26	65.5	5.10
0.78	0.31	76.3	5.29
0.91	0.36	88.9	5.42
1.1	0.41	103.6	5.49
1.2	0.45	120.7	5.51
1.4	0.50	140.6	5.30
1.7	0.54	163.8	4.98
2.0	0.58	190.8	4.53
2.3	0.62	222.3	3.92
2.7	0.66	259.0	3.14
3.1	0.71	301.7	2.22
3.6	0.77	351.5	1.23
4.2	0.84	409.5	0.22
4.9	0.92	**Total**	**100**
5.7	1.00		
6.6	1.08		
7.7	1.18		
9.0	1.27		
10.5	1.39		
12.2	1.52		
14.2	1.70		

Particle size distributions for ash storage pile

Tutuka	ASH1	ASH2
	Tutuka Ash Dump	Majuba Ash Dump
psd (µm)		
	Fractions as percentages	
0.05	-	-
0.06	-	-
0.07	-	-
0.08	-	-
0.09	-	-
0.11	-	-
0.13	0.01	-
0.15	0.01	-
0.17	0.03	-
0.20	0.04	-
0.23	0.06	-
0.27	0.07	-
0.31	0.09	-
0.36	0.11	-
0.42	0.14	-
0.49	0.16	-
0.58	0.18	-
0.67	0.20	-
0.78	0.22	-
0.91	0.24	-
1.1	0.27	-
1.2	0.30	-
1.4	0.34	-
1.7	0.39	0.16
2.0	0.47	0.27
2.3	0.56	0.40
2.7	0.68	0.43
3.1	0.84	0.62
3.6	1.02	0.80
4.2	1.23	0.85
4.9	1.46	1.12
5.7	1.63	1.42
6.6	1.70	1.73
7.7	1.95	2.07
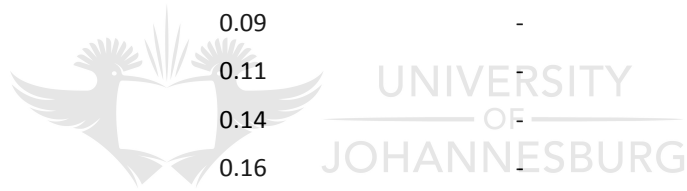
Tutuka	ASH1	ASH2
	Tutuka Ash Dump	**Majuba Ash Dump**
psd (µm)	Fractions as percentages	
9.0	2.19	2.43
10.5	2.42	2.85
12.2	2.83	3.30
14.2	3.01	3.80
16.6	3.16	4.33
19.3	3.28	4.84
22.5	3.36	5.31
26.2	3.40	5.67
30.5	3.42	5.89
35.6	3.43	5.95
41.4	3.46	5.84
48.3	3.53	5.59
56.2	3.68	5.23
65.5	3.91	4.81
76.3	4.23	4.43
88.9	4.59	4.38
103.6	4.94	4.03
120.7	5.25	3.73
140.6	5.33	3.07
163.8	5.03	2.60
190.8	4.31	0.99
222.3	2.66	0.68
259.0	2.23	0.38
301.7	1.95	-
Total	**100**	**100**
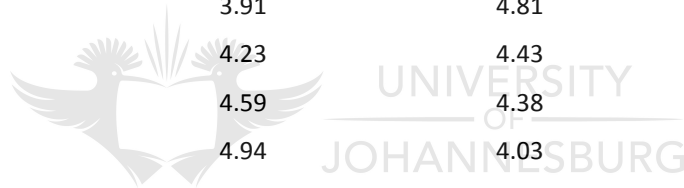
Appendix B: Graphical Representations for the Six TSFs
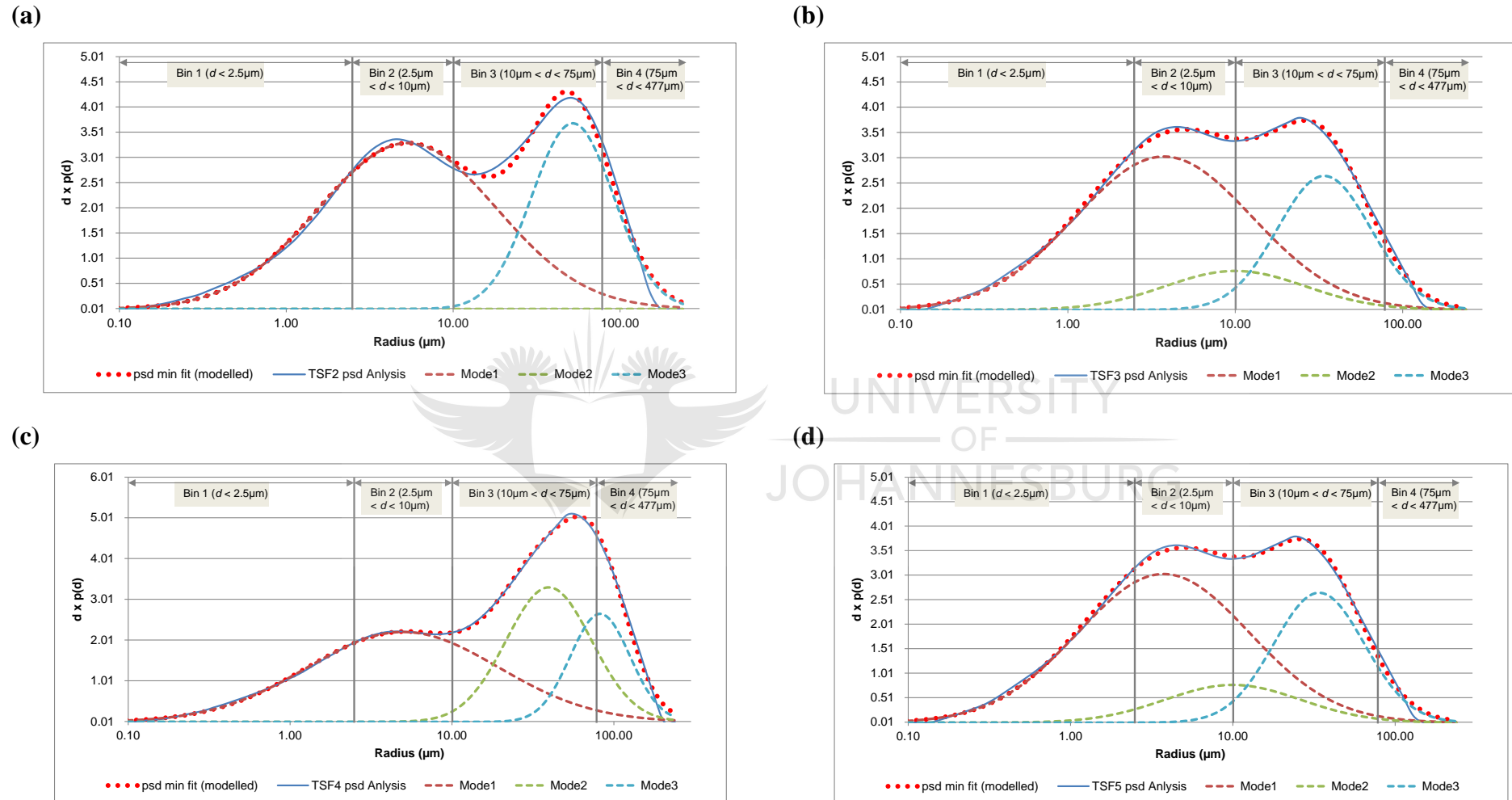
(a)

(b)

(c)

(d)

Figure 61: Least squares fit of a three-mode model applied to the measured particle size distribution of sample of tailings material from the AngloGold Ashanti (a) West Complex (TSF2); (b) South East (TSF3); (c) East Complex (TSF4); (d) South Complex (TSF5) and € Sulphur Paydam (TSF6).
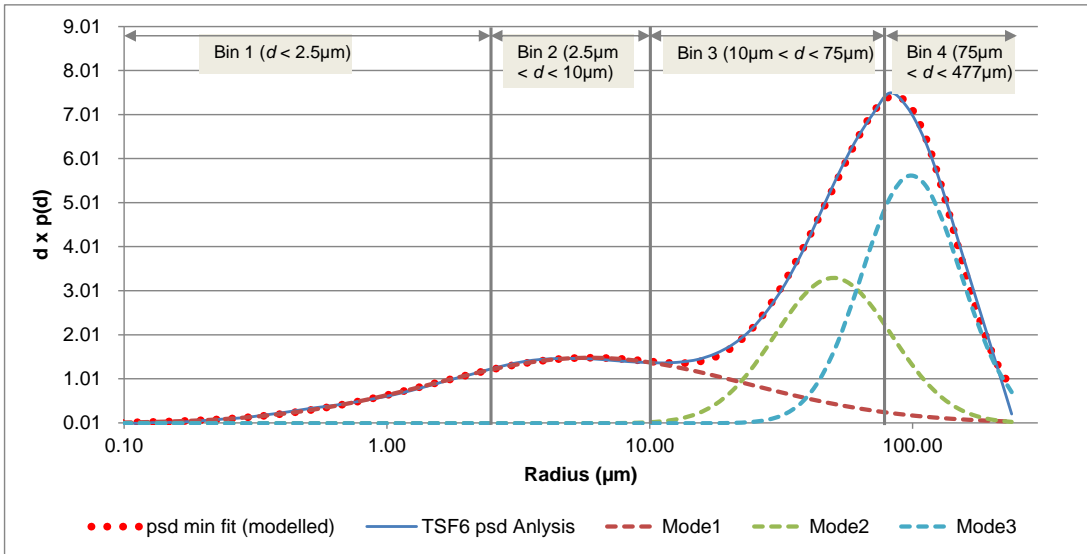
Figure 62:   Least squares fit of a three-mode model applied to the measured particle size distribution of sample of tailings material from the AngloGold Ashanti Sulphur Paydam (TSF6).